



2017

Studies In Mesoscopics And Quantum Microscopies

Zhenghao Ding
zding@iwu.edu

Gabriel C. Spalding
Illinois Wesleyan University, gspaldin@iwu.edu

Recommended Citation

Ding, Zhenghao and Spalding, Gabriel C., "Studies In Mesoscopics And Quantum Microscopies" (2017). *Honors Projects*. 18.
http://digitalcommons.iwu.edu/physics_honproj/18

This Article is brought to you for free and open access by The Ames Library, the Andrew W. Mellon Center for Curricular and Faculty Development, the Office of the Provost and the Office of the President. It has been accepted for inclusion in Digital Commons @ IWU by the faculty at Illinois Wesleyan University. For more information, please contact digitalcommons@iwu.edu.

©Copyright is owned by the author of this document.

ILLINOIS WESLEYAN UNIVERSITY

DEPARTMENT OF PHYSICS

UNDERGRADUATE HONORS RESEARCH

STUDIES IN MESOSCOPICS AND QUANTUM MICROSCOPIES

By

ZHENGHAO (ANDY) DING

A Thesis submitted to the
Department of Physics
in fulfillment of the
requirements for the
Honors Research

2017

The members of the supervisory committee were:

Gabriel C. Spalding, Ph.D.

Ames Professor of Physics, advisor of this project

Narendra Jaggi, Ph.D.

Professor of Physics

Robert Wagner, Ph.D.

Visiting Assistant Professor of Physics

Tian-Xiao He, Ph.D.

Beling Professor of Mathematics

ACKNOWLEDGMENTS

I would like to express my sincere gratitude to Prof. Gabriel C. Spalding for the continuous support of my undergraduate projects, for his patience, motivation and immense knowledge. His guidance helped me throughout the process of doing the research as well as the writing required for this thesis. I could not have imagined having a better advisor and mentor for my undergraduate physics studies.

In addition, I would like to thank the rest of my thesis committee: Prof. Narendra Jaggi, Prof. Tian-xiao He, and Dr. Robert Wagner, for their insightful comments and encouragement, but also for their hard questions and from various perspectives, which motivated me to widen my research.

I would like to thank Dr. Martin Lavery for his supportive collaboration and for his useful criticism of my work. My sincere thanks also goes to Prof. David Weitz and Prof. Paul Kwiat, who each provided me with the opportunity to join their team as intern/visiting student, and who gave access to their laboratory and research facilities. Without their precious support it would not have been possible to complete key portions of this research. Also I would like to thank Dr. Xu Zhang and Dr. John Heyman, for their immense support during my research at Harvard University. A special thanks to Prof. Tim Rettich and Prof. William Jaeckle, who provided me, respectively, with guidance and very significant support for vaterite synthesis and imaging with a scanning electron microscope, and to Dr. James Millen for providing meaningful comments on my work.

TABLE OF CONTENTS

Abstract	vi
0.1 Introduction	vi
1 Studies in quantum optics	1
1.1 Introduction to Quantum Optics	1
1.2 A description of Type I Spontaneous Parametric Down-Conversion	2
1.2.1 Introduction to SPDC	2
1.2.2 Phase Matching	3
1.2.3 The Index of Refraction for Ordinary and Extraordinary Polarizations	5
1.3 Experimental Spontaneous Parametric Down-Conversion	10
1.3.1 Down-conversion Setup	10
1.3.2 Aligning the sub-systems	17
1.4 Establishing that we have a true Single-Photon Source	21
1.4.1 Introduction to Quantum Optics	21
1.4.2 Experimental setup for studying Source Statistics	25
1.4.3 Alignment and Source Statistics data collection	26
1.4.4 Experimental results on SPDC Source Statistics	27
1.5 Quantum State Measurement	29
1.5.1 Introduction to the Inverse Problem	29
1.5.2 Experimental setup for Querying Single-Photon States	31
1.5.3 Alignment and Quantum State data collection	32
1.5.4 Experimental results for Quantum State Measurement	33
1.6 Bell's test of Local Realism	36
1.6.1 Introduction to Quantum Weirdness	36
1.6.2 The CHSH inequality	39
1.6.3 Experimental setup and data collection for testing Local Realism	43
1.6.4 Experimental results for testing the CHSH inequality	45
1.6.5 Error analysis for our Parity Function result	46
2 Experimental analysis of the Orbital Angular Momentum of Light	48
2.1 Topics regarding the Angular Momentum of Light	48
2.2 The Orbital Angular Momentum of light	50
2.2.1 Introduction to OAM	50
2.2.2 Beyond the fundamental Gaussian mode	51
2.2.3 Laguerre-Gaussian modes	53
2.2.4 Experimental generation of Laguerre-Gaussian beams	55
2.3 Programming a Spatial Light Modulator: a primer	59
2.3.1 A very brief introduction to IDL programming	59
2.3.2 Creating a window for display	60
2.3.3 Generating LG beams using LG.pro	61
2.3.4 The original code for LG.pro	65

2.3.5	Enforcing symmetry upon the phase profile	67
2.4	Aberration Correction	72
2.4.1	Iterative phase optimization algorithms	72
2.4.2	Integrating the Adaptive-Additive algorithm into the Ritsch-Marte method for Aberration Correction	73
2.4.3	Application of Ritsch-Marte/AA aberration correction method	79
2.5	Transformation Optics: rapid readout of OAM	81
2.5.1	Introduction to the Lavery method of OAM readout	81
2.5.2	Mathematical expression of the Lavery Transform	81
2.5.3	Experimental setup and alignment for OAM readout	83
2.5.4	First implementation of the transformation optics	88
2.6	Vaterite Synthesis	89
2.6.1	The desire for Birefringent Spheres	89
2.6.2	Synthesis protocols	89
2.6.3	Important tips	90
2.6.4	The polydisperse ensembles produced	91
2.7	Applications of Optical Angular Momentum: Contact-Free Mechanotransduction, and the Quantum Limit of Optomechanics	92
3	Studies in microfluidics, and the creation of micro-containers for nano-components	95
3.1	Introduction to microfluidics and lab-on-a-chip technology	95
3.2	Designing microfluidic devices	98
3.2.1	Introduction	98
3.2.2	Device components	98
3.3	PDMS-based microfluidic device fabrication	105
3.3.1	Materials required	105
3.3.2	Fabrication protocols for microfluidic chips	108
3.4	Application of lab-on-a-chip technology: droplet-based single cell immunol assay . .	118
3.4.1	Introduction	119
3.4.2	Method 1: Dye release	120
3.4.3	Method 2: Apoptosis Detection	121
3.4.4	Method 3: Fluorescence concentration assay to detect secreted IFN- γ	122
3.4.5	Notes and protocols on water droplet generation using co-flow microfluidic devices	123

Bibliography

ABSTRACT

0.1 Introduction

This thesis begins with a foundational section on quantum optics. The single-photon detectors used in the first chapter were obtained through the Advanced Laboratory Physics Association (ALPhA), which brokered reduced cost for educational use, and the aim of the single-photon work presented in Chapter 1 is to develop modules for use in Illinois Wesleyan’s instructional labs beyond the first year of university. Along with the American Association of Physics Teachers, ALPhA encourages capstone-level work, such as Chapter 1 of this honors thesis, which is explicitly designed to play the role of passing on, to a next generation of physics majors, materials that can play a central role in their curriculum. Thus, although such work had previously been done at other institutions, the value added by this work has to do with the impact upon the local curriculum, and the utility of the collation of these materials into one single, easily accessible form.

Beyond its first chapter, this thesis extends into my research projects, each of which, in the long term, carries a motivation that connects back to questions raised in the studies described in Chapter 1. While the first chapter describes ways in which we can experimentally study the “spin” polarization state of a single photon, the second deals extends the discussion of how information may be encoded into the angular momentum of light, and some of its potential long-term consequences, *e.g.*, for experiments involving optical traps that may someday test for the (controversial) hypothesized existence of a boundary between the microscopic (quantum) and macroscopic (classical) domains. Here, too, the work presented builds upon a body of work in the recent research literature. The final chapter deals with the creation of meso-scale systems for use in advanced optical traps studies. Each of these last two chapters points towards opportunities in physics research that are tentative in nature and, as such, constitute research that is very much aspirational. The citations provided, while not exhaustive, point both towards some of the more useful resources discovered during this work, and to some ongoing controversies in the field. At the same time, these chapters also aim to delineate concrete, specific steps that we have taken, which we believe are of immediate interest in their own rights.

CHAPTER 1

STUDIES IN QUANTUM OPTICS

1.1 Introduction to Quantum Optics

The quantum nature of light was posited by Albert Einstein, in his paper on the photoelectric effect in 1905. In recent years quantum optics, which studies the quantum mechanical behavior of light using semi-classical and quantum physics, has become one of the fastest developing field in physics and engineering, with a heartening stream of advances, *e.g.*, regarding methods for generation of entangled pairs of photons, clarification of paradigms such as quantum erasure and the Hong-Ou-Mandel effect, and the development of key elements for potential applications, such as optical quantum information processing. In this thesis, I present elements of my study of the generation of quantum mechanically entangled pairs of photons, through nonlinear processes, and outline multiple experiments that I have performed for studying specific quantum properties of photons, beginning with generation of entangled photons, from which we prove that we can meaningfully extract a true, single-photon source, and including methods for quantum state measurement and a test of the Einstein-Podolsky-Rosen (EPR) paradox and Bell's test of local realism.

1.2 A description of Type I Spontaneous Parametric Down-Conversion

1.2.1 Introduction to SPDC

Spontaneous Parametric Down-Conversion (SPDC) describes an optical phenomenon where a beam of photons (the “pump” beam) passing through a non-linear, birefringent crystal spontaneously splits into two beams of photons with lower frequency, traditionally called the signal and idler beam (since the idler is typically used only to herald, via coincidence counting, the arrival of the signal photon, which is used for tests of quantum mechanics at the single-photon level). The SPDC process can be roughly viewed as the reverse process of second-harmonic generation (SHG), where two photons with equal energy combine, while passing through a nonlinear crystal, into one photon with double the energy. However, SHG has a much higher efficiency, as it is a “seeded” process, which is to say that SHG is a stimulated process where the generation of a single, higher-energy photon is triggered by the coincident absorption of two photons that deposit their energy simultaneously with one another, leading to reemission at the higher energy. In contrast, SPDC is a spontaneous process where there is no clear “seed” to the conversion (*i.e.*, why should the input photon split its energy exactly in half? why not in some unequal proportion?). In fact, each such allowed division is possible, but the lack of any direct simulation for SPDC processes explains the relatively low efficiency compared to SHG. The fact that SPDC occurs at all has led to the suggestion that SPDC is likely triggered by the photons generated by quantum field fluctuations (“vacuum fluctuations”). In fact, in Chapter 16 of the Mark Beck text, he writes, “The correct prediction of the spontaneous emission rate is one of the great triumphs of quantum field theory.” [6]

The importance of SPDC lies in the fact that when one pump photon generates two down-converted photons, those output photons are very strongly correlated. They were generated at the same point in space and time, and the conservation laws mandate that if one of these output photons has transverse momentum, relative to the direction of the input beam, then the other in the pair must have the opposite transverse momentum. So, these two photons are correlated in transverse position and anti-correlated in transverse momentum. These correlations lie at the heart of heralded detection methods, including such demonstrations of “spooky action at a distance” as ghost imaging and ghost diffraction.

1.2.2 Phase Matching

SPDC must obey the basic conservation principles. Thus, the output photons must each have lower energies than the pump photon that generated them. Inside a normal medium this would make it difficult to simultaneously satisfy the constraints of momentum conservation, simply because normal dispersion in a transparent material yields a reduction in the total momentum for the output in comparison to the input, a problem which can only be overcome by moving to birefringent media.

Because the phase of a propagating wave is dependent upon momentum and energy, the basic conservation laws are often phrased in terms of “phase matching” of the input and output beams, viewed as classical electromagnetic waves. Inside birefringent materials, the phase velocity of light (and thus the index of refraction) depends upon polarization and frequency. Again, the down-converted beams have different frequencies (energies) compared to the input (“pump”) beam and, because of the frequency dependence of the index of refraction, conservation of momentum is not trivial to achieve. However, by tilting a birefringent crystal, one can tune the effective index, so as to optimize the matching conditions. As is detailed in Section 1.1.2, any remaining difference in refractive indices for the pump and down-converted beams will mean that the output photons must travel through the crystal at an angle with respect to the original beam. The size of this “spreading angle” is calculated below, given a particular (near optimal) orientation of the birefringent crystal.

In order to find the spreading angle, we explicitly write down the basic conservation laws, in Equation (1.1) and (1.2), invoking an assumption that the SPDC process may be treated as if it were, effectively, a three-body process.

$$E_p = E_s + E_i \tag{1.1}$$

$$\vec{p}_p = \vec{p}_s + \vec{p}_i \tag{1.2}$$

From quantum mechanics, we have Equations (1.3) and (1.4).

$$E = \hbar\omega \tag{1.3}$$

$$\vec{p} = \hbar\vec{k} \tag{1.4}$$

Plugging in (1.1) and (1.2), we can get Equations (1.5) and (1.6).

$$\omega_p = \omega_s + \omega_i \quad (1.5)$$

$$\vec{k}_p = \vec{k}_s + \vec{k}_i \quad (1.6)$$

Notably, Planck's Constant, originally appearing on both sides of each equation, has canceled out. When the momentums of the signal and idler photons have the same direction as the pump beam, the downconversion is said to be collinear. Depending upon the wavelength of the pump and the tilt of the nonlinear crystal used for the downconversion process, it is also possible to for SPDC to be non-collinear, which results in a “doughnut-shaped” output beam.

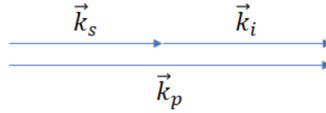


Figure 1.1: Linear down-conversion

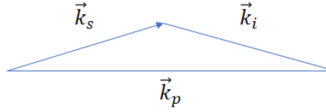


Figure 1.2: Nonlinear down-conversion

Now let's calculate the spreading angle between the beams, which, as we will see, depends upon the orientation of our BBO crystal, which sets the effective indices of refraction. From Fig. 1.1, by vector analysis, we can get Equation (1.7) and (1.8) from (1.6).

$$|\vec{k}_p| = |\vec{k}_s| \cos(\theta_s) + |\vec{k}_i| \cos(\theta_i) \quad (1.7)$$

$$|\vec{k}_s| \sin(\theta_s) = |\vec{k}_i| \sin(\theta_i) \quad (1.8)$$

The relationship between k vector and angular frequency is given in Equation (1.9). [23]

$$|\vec{k}_{p,s,i}| = \frac{\omega_{p,s,i} n_{p,s,i}}{c} \quad (1.9)$$

If our experiment uses filters to select output photons having the same energy as one another, we can set the energy of the signal and idler photons equal to each other, as shown in Equation (1.10).

$$\omega_s = \omega_i \tag{1.10}$$

Now, we can substitute (13) and (14) into (11) and (12) to get relationships between the indices of refraction and the angle between signal/idler beam and the pump beam, which are expressed in Equation (1.11), (1.12), (1.13) and (1.14).

$$\theta_s = \theta_i \tag{1.11}$$

$$n_s = n_i \tag{1.12}$$

$$\cos\theta_{s,i} = \frac{n_p}{n_{s,i}} \tag{1.13}$$

$$\theta_{s,i} = \arccos\left(\frac{n_p}{n_{s,i}}\right) \tag{1.14}$$

As is evident in Equation (1.14), the angle between pump beam and signal beam is determined by the indices of refraction of both the pump beam and the signal/idler beam.

1.2.3 The Index of Refraction for Ordinary and Extraordinary Polarizations

The only way to satisfy all of the constraints for SPDC is for the down-conversion crystal to be birefringent, meaning that the index of refraction depends on the *direction* of propagation, as well as the wavelength and polarization of the beam. This adds an additional degree of freedom (related to the tilt of the crystal), which is used to ensure the above equations are satisfied.[18]

Optical components are typically made using glasses, where there is no long-range order of atomic positions. Since the wavelength of light used in our experiments is much longer than the atomic spacing, a great deal of averaging (*e.g.*, over bond angles) occurs and, in the end, the medium is effectively isotropic. On the other hand, there are many transparent *crystals*, where the propagation is non-isotropic. That is, in a crystal, electrons experience different amounts of restoring force when ?sloshing?? in different directions. As long as absorption is negligible, the relative propensity for

slushing is described by an electric susceptibility tensor that is real and symmetric, and which can be diagonalized by choosing the appropriate set of axes, called the “principal axes” of the medium. Given the constraint that absorption is negligible, these axes will be orthogonal, and so are called x , y , and z . The crystals that we will discuss have diagonalized electric susceptibility tensors where $\chi_{xx} = \chi_{yy} \neq \chi_{zz}$. For these kinds of birefringent materials, there is one direction, described in Figure 1.3, such that any beam traveling along that particular direction will experience the same phase speed, c/n_0 , regardless of its polarization state. This unique direction is called the “optic axis” of the material (and such birefringent materials are said to be “uniaxial”). Such materials are characterized by two refractive indices, the “ordinary” index, n_0 , for light polarized in the x or y directions, and an “extraordinary” index, n_e , for light polarized in the z direction.

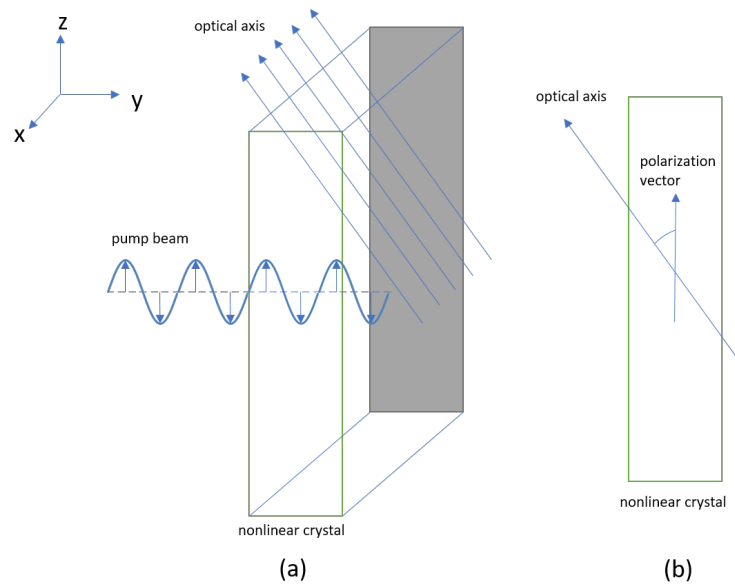


Figure 1.3: An “ordinary” beam traveling through a nonlinear crystal. (a) Here, the coordinate system is not that of the crystal, but is such that the pump beam is traveling along the y direction, while the optical axis of the nonlinear crystal is parallel to the y - z face. That back face of the crystal is shadowed in the figure, and the direction of the optical axis is marked by several vectors that lie parallel to the y - z face. Here, the polarization vector of the pump beam is also parallel to the y - z plane. (b) Front view, *i.e.*, looking at the front y - z face: there is an angle between the optical axis and the polarization vector. The index of refraction of the beam is independent of this angle. As long as the polarization vector lies in the same plane as the optical axis, the index of refraction of the crystal can be calculated using Equation 1.15

The ordinary index of refraction, n_0 , depends upon the wavelength of the light, as follows from a simple model, called the Sellmeier equation, which is applicable at frequencies well below the resonant (UV) frequencies of electron shells: [18]

$$n_0^2(\lambda) = A_0 + \frac{B_0}{\lambda^2 + C_0} + D_0\lambda^2 \quad (1.15)$$

Here, λ is the wavelength of the beam, and A_0 , B_0 , C_0 , and D_0 are all coefficients that are determined by the properties of the crystal.

On the other hand, if the polarization of the beam lies *within* the plane formed by the optical axis and the propagation direction of the beam, as illustrated in Figure 1.4, it will experience an index of refraction n_e that depends both on the wavelength of the beam and, additionally, upon the angle ϕ shown in the graph, which is the angle between the optical axis and the pump beam. The index

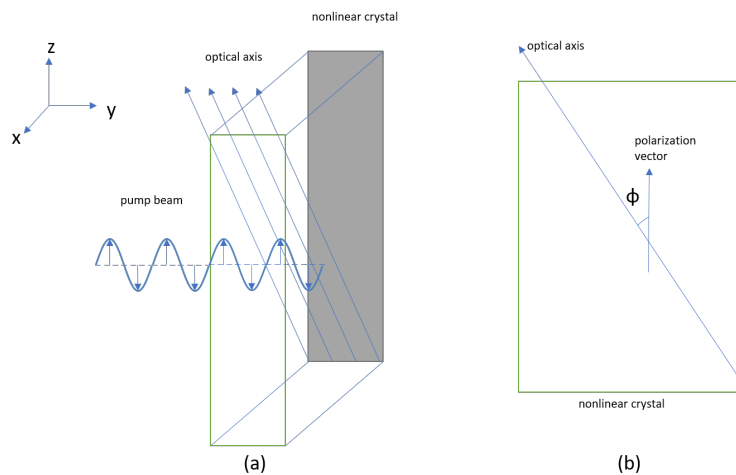


Figure 1.4: An extraordinarily polarized beam traveling through a nonlinear crystal. (a) Here, the pump beam is traveling along the y direction, while the optical axis of the nonlinear crystal lies in the x - z plane. The back face of the crystal is shadowed in the figure, and the direction of the optical axis is marked by several vectors that lie in the x - z plane. The polarization vector of the beam lies in y - z plane, the same as the optical axis. (b) Looking into the right surface of the crystal, *i.e.*, the x - z plane, there is an angle ϕ between the optical axis and the polarization vector. Here, the index of refraction of the beam depends on this angle, as shown in Equation 1.16

of refraction n_e as a function of ϕ and λ is given by Equation (1.16).[18]

$$\frac{1}{n_e(\lambda, \phi)^2} = \frac{\cos^2(\phi)}{n_o(\phi)^2} + \frac{\sin^2(\phi)}{n_e(\phi)^2} \quad (1.16)$$

Here, $n_e(\lambda)$ is calculated using Equation(1.17), while $n_o(\lambda)$ is calculated using Equation(1.15). [18]

$$n_e^2(\lambda) = A_e + \frac{B_e}{\lambda^2 + C_e} + D_e\lambda^2 \quad (1.17)$$

Again, λ is the wavelength of the beam, and A_e , B_e , C_e , and D_e are all coefficients that are determined by the properties of the crystal. [18]

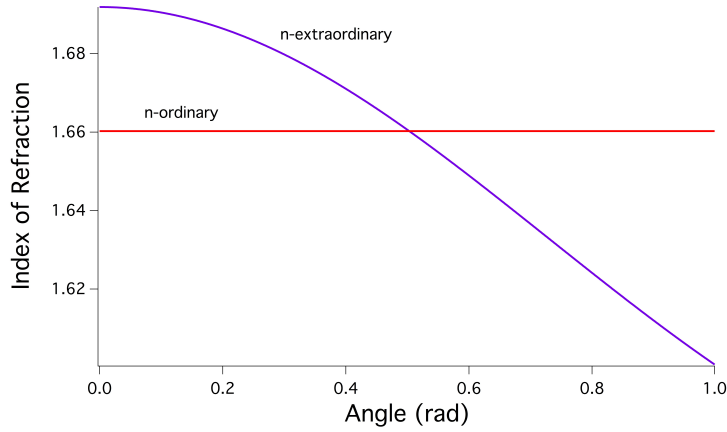


Figure 1.5: Index of refraction, as a function of birefringent crystal orientation. To satisfy conservation of momentum, downconverted photon polarizations are orthogonal to that of the pump, so here the ordinary index of refraction is plotted for a wavelength of 810 nm, while the extraordinary index is plotted for a wavelength of 405 nm, assuming that, if the wavelengths are given in microns, coefficients in the Sellmeier equations for BBO are $A_0 = 2.7359$, $B_0 = 0.01878$, $C_0 = -0.01822$, $D_0 = -0.01354$, while $A_e = 2.3753$, $B_e = 0.01224$, $C_e = -0.01667$, and $D_e = -0.01516$. Our BBO crystal is cut at 0.511 radians (29.3 degrees), which – for our pump wavelength – is *close* to the crossing point of the two curves shown.

For the nonlinear SPDC process to occur, it must satisfy both conservation of energy and momentum. The latter is not satisfied in most transparent media, because normal dispersion ensures that the total momentum of the signal and idler would be less than that of the pump photon. However, in a birefringent material, if the pump beam is polarized such that it is characterized by the extraordinary index of refraction, then total momentum can be conserved when the signal and

idler photons are emitted with polarization orthogonal to that of the pump, so that these output photons are characterized by the ordinary index of refraction.

1.3 Experimental Spontaneous Parametric Down-Conversion

1.3.1 Down-conversion Setup

An initial exploration of SPDC was setup according to instructions provided in the book *Quantum Mechanics: Theory and Experiment* by Mark Beck. The same entangled-photon source described here is utilized in all further single-photon experiments contained in this thesis.

For our work, an inexpensive blue-ray 405-nm laser is setup as the initial light source (*i.e.*, the

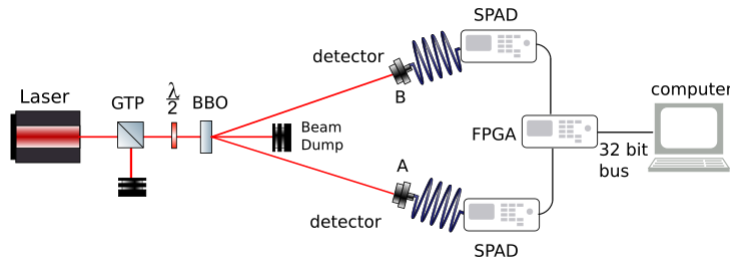


Figure 1.6: The setup for SPDC

“pump beam”). To ensure linear polarization, the pump is steered directly into the center of the Glan-Taylor polarizer, and to adjust the orientation of that polarization, we make use of a half-wave plate on a rotary mount, before arriving, at normal incidence, at our BBO crystal. For simplicity, the required steering mirrors are not shown in the schematic diagram shown in Fig. 1.6.

The BBO crystal and the angle of separation

From Section 1.2.2, it is known that the angle of separation between the down-converted photons and the pump beam is the inverse cosine of the ratio between the indices of refraction of the crystal at 405 nm and at 810 nm, as shown below in Equation 1.18:

$$\theta_{s,i} = \arccos\left(\frac{n_p}{n_{s,i}}\right) \quad (1.18)$$

As indicated in Fig. 1.5, for our BBO crystal at normal incidence, the index of refraction at the pump wavelength is fairly close to that of the downconverted beams, but there is a small difference:

the index is 1.659 at 405 nm and 1.661 at 810 nm. From this, it can be shown that the resulting angle of separation is approximately 2.8 degrees.

The crystal we are using for this lab is a single Type-I BBO crystal, as is the case for nearly all of the single-photon experiments I have done, except for one involving a Bell's test, where there was a need to use a double crystal. In general, though, our double crystal produces less down-converted photons, as that crystal is shorter, and so the longer, single crystal described here has been the workhorse for our investigations.

Even with our longer crystal, the efficiency of the down-conversion process is very low, and so the pump beam coming out of the crystal has, essentially, the same intensity as the original pump beam. It is unsafe, both for the single-photon detectors and for the experimenters themselves, to allow the pump beam to freely propagate around. In addition, there can be problems with fluorescence of the filters that protect the detectors. The colored-glass filters we are using will work well to filter scattered background light, but if you hit them with the pump beam, they will fluoresce. This issue could be controlled by filtering the majority of the pump beam first with some sort of interference filter (*i.e.*, a "cold mirror"), but we've simply ensured that the collection optics are physically further from the down-conversion crystal; the further away from the source that you are imaging onto your fibers, the less fluorescence you will collect. Given that our collection optics are nearly a meter away from the BBO crystal, we have room for a beam "dump" to be placed along the optical axis to absorb the pump beam, once it has passed through the BBO crystal and completed its "job."

Collection optics

It is highly recommended to add a bandpass filter, or a broadband filter in front of the collection optics, to get rid of any stray 405-nm light that has been scattered into the path, as well as other optical noise in the room. In addition, regular optical fiber is deemed unsuitable for protecting the single-photon detectors from stray light that can leak in through the jacketing materials, and so the first bit of fiber most directly connected to the Single-Photon Avalanche Diodes (SPADs) should either be specialty opaque fibers or regular fiber with opaque covers added to them, to shield out background optical noise.

Collection optics using convex lenses couple the down-converted beams into the optical fibers that transmit the signals into SPADs. The distance between the lens and the fiber is critical to this coupling, as is the range of angles for rays entering the optical fiber. Given that optical fiber relies upon Total Internal Reflection (TIR) at the core-cladding boundary, rays coming in at too steep an angle will be lost. Thus, we must also optimize the collection angle of the collection optics, by using collection optics with appropriate Numerical Aperture (NA). Moreover, we must ensure that these collection optics point directly towards the BBO crystal. To achieve that final goal, we perform an initial alignment by “back-propagating” a fiber-coupled visible laser: sending the output of that laser’s output fiber through what would normally be our collection optics back towards the BBO crystal. Fine tuning of the “pointing direction” for our collection optics can only be done by optimizing the count rate of the detected down-converted single photons.

Each fiber should have the same length to avoid differences in propagation time, which will result in errors in coincidence counting.

For the experiments described here, we used multimode optical fiber. Without spatial filtering of the pump beam, the output from our 405-nm laser contains multiple modes. Yet even if we were to use a single-mode laser, the SPDC process itself yields output which may be described as a superposition of modes. Thus the source does not have the high degree of coherence necessary to yield high-contrast single-photon interference, but if we were to replace the multimode fiber with single-mode optical fiber, the effect would be to discard higher mode contributions, as has been demonstrated in the work of Aspden, Padgett, and Spalding, *Am. J. Phys.* **84**, 671 (2016). [4]

Glan-Taylor polarizer

The Glan-Taylor polarizer (GTP in Fig. 1.6) is for purifying the polarization of the pump beam. The diode laser we utilize was, again, selected as an inexpensive source. The untreated output from this laser contains multiple modes with multiple polarizations. The Glan-Taylor polarizer is a polarizing beam splitter. It will reflect away photons with other polarizations and preserve the photons with horizontal polarization. Having a pump beam with a well-defined polarization state is important to single-photon experiments, as we have more knowledge and more control over the system. As suggested by Fig 1.5, polarization also plays a role in optimizing the efficiency of the

downconversion process.

Half-wave plate

Because the polarization of the pump beam is relevant to the phase-matching process, we make use of a half-wave plate, which is a transmissive element that allows rotation of the polarization of the input beam. During the alignment process, we rotate the half-wave plate until the count rate of down-converted photons, measured at our detectors, is maximized. Rotating the half-wave plate also allows us to check whether we are getting any “real” signal. If rotation of the polarization does not change the measured counts at the detectors, that implies that whatever signal is present is not associated with down-converted light coming from the BBO crystal.

Single-Photon Avalanche Diodes

A single 810-nm photon carries very little energy. Translating information from this “microscopic” entity to the macroscopic realm requires an *irreversible, entropy-producing* process: amplification. In our work, this involves (Geiger-mode) avalanche of a solid state diode biased to very near an instability, such that a small perturbation (associated with a single, incoming photon) causes a large, easily measurable result. The Laboratory for Mesoscopics and Quantum Microscopies, which I have been a part of during my work at Illinois Wesleyan, has broad interest in this sort of issue, and its impact upon information, and it will recur as a theme of interest in work to be described later on, in Chapter 3, of this thesis.

When a photon deposits its energy in the active area of a SPAD, it initiates a charge avalanche which yields a pulse that has a fast onset associated with the avalanche dynamics, and a longer decay associated with the RC time constant of the system (which leads to a “dead time” during which the detector is incapable of re-firing). It is the well-defined *leading* edge of this pulse that is used for timing (*e.g.*, to determine whether pulses from two different SPAD detectors fall within a “coincidence” window). Thus, a SPAD is a basic transducer used to convert optical signals into well characterized electric timing cues.

The output of each SPAD is sent, via coaxial cable to a Field-Programmable Gate Array (FPGA), which acts as a fast logic circuit for determining coincidence. The coaxial cabling must have a characteristic (transmission line) impedance which matches the output impedance of the SPAD in order to minimize signal loss and reflection during the transmission process. For the ALPhA SPADs, the output impedance is 50Ω . In addition, the length of the coaxial cables should be roughly the same, as any difference in length translates into the time delay, which could result in errors in the reported coincidence count rates. (For estimation purposes, it is useful to assume that the speed of the electrical pulses is roughly $0.8c$. So, while light travels in free space one foot per nanosecond, a one-foot difference in cable length would correspond to a delay of around 1.27 ns.

The Field-Programmable Gate Array

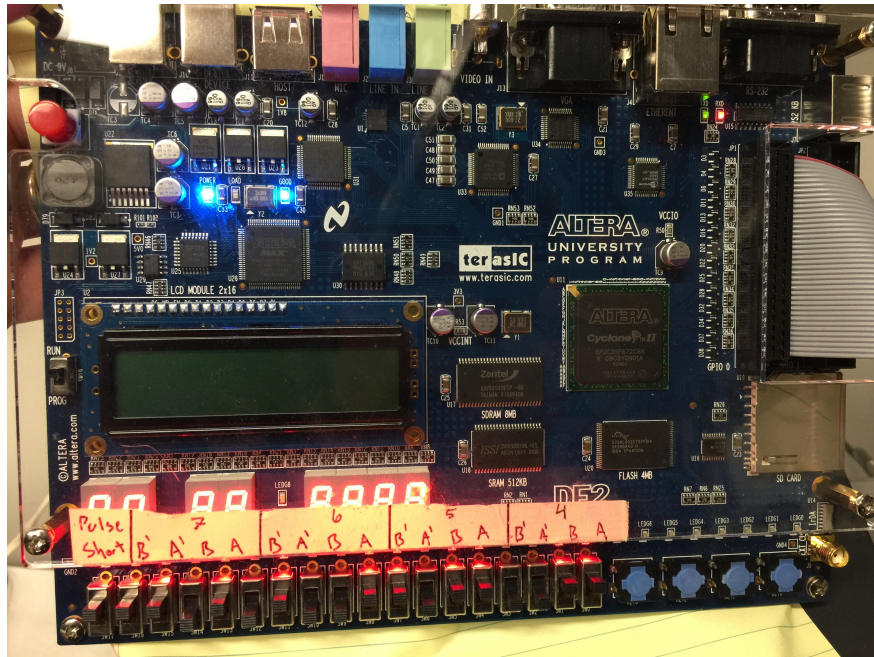


Figure 1.7: The Field-Programmable Gate Array (FPGA), which is used to determine coincidences between detection events.

Fig 1.7 contains a photo of the kind of FPGA we use, which is an Altera Model DE-2. As currently configured, this FPGA limits us to no more than four SPAD detectors in a single experiment. The

FPGA processes the signals from the SPADs with digital logic gates, and outputs (8) 32-bit arrays to a *LabVIEW* program on the computer, using an RS-232 bus (which an industrious student could easily upgrade to a USB-bus). Of the (8) 32-bit arrays output, the first four arrays, indexed 0 to 3, are report the individual counts detected by each SPAD, which are referred to as “singles” and are labeled as A, B, A’ and B’. The last four arrays, indexed 4 to 7 (from right to left at the bottom of Fig. 1.7), are for coincidence counts, which are referred to as the “doubles” (*e.g.*, if AB are switched on while A’ and B’ are off) or “triples” (*e.g.*, if ABB’ are switched on while A’ is off), *etc.*: precisely what information arrays 4-7 will contain depends on how those physical switches on the FPGA board are set.

To reiterate: as is shown along the bottom of Fig 1.7, there are 16 physical switches the edge the FPGA board. We have labeled these in four groups. There are four switches in each group, with each switch labeled with the names of the four SPAD detectors. How we set the switches within each group “hardwires” the programming of logic gates in the FPGA, so that they will report the outcome of a type of coincidence measurement. Setting switches within a group to the “on” position sends the output of the specified detectors to digital gates which correspond to a Boolean “AND” operation, which is how we measure coincidence counts for those detectors.

The outputs of the logic gates in a group correspond of one of the last four 32-bit arrays of data in each block sent to the computer. For example, if switch A and switch B in group 4 are switched on, the output of the fifth 32-bit array will be the coincidence counts observed between detectors A and B. If switch B and B’ in group 7 are switched on, the output of the eighth 32-bit array will be the coincidences observed between detector B and B’.

While the machine-specific programming of the FPGA is written in *Verilog HDL* code, this is embedded into a *LabVIEW* program that is openly available on Mark Beck’s website, along with complete instructions on how to bootload instructions onto the FPGA.

The LabVIEW front end

We make use of Mark Beck’s *LabVIEW* program called “coincidence-rs232.vi,” both for the initial experiment described in this section as well as for some additional experiments described later. A screen shot of the program is in Fig 1.8. Users switch between sub-programs appropriate to

different experiments by toggling the “Experimental Setup” dial on the left of the screen. For an initial SPDC experiment, set the dial to the “Coincidence” position. Critical to successful operation of the program is selection of the correct counter port, at the bottom of the screen. As currently configured in our lab, the correct counter port is COM1. Obviously, communicating to the wrong port should result in no signal, but in practice, if the wrong port is selected, the program will crash. *LabVIEW* will then need to be restarted before reopening this program.

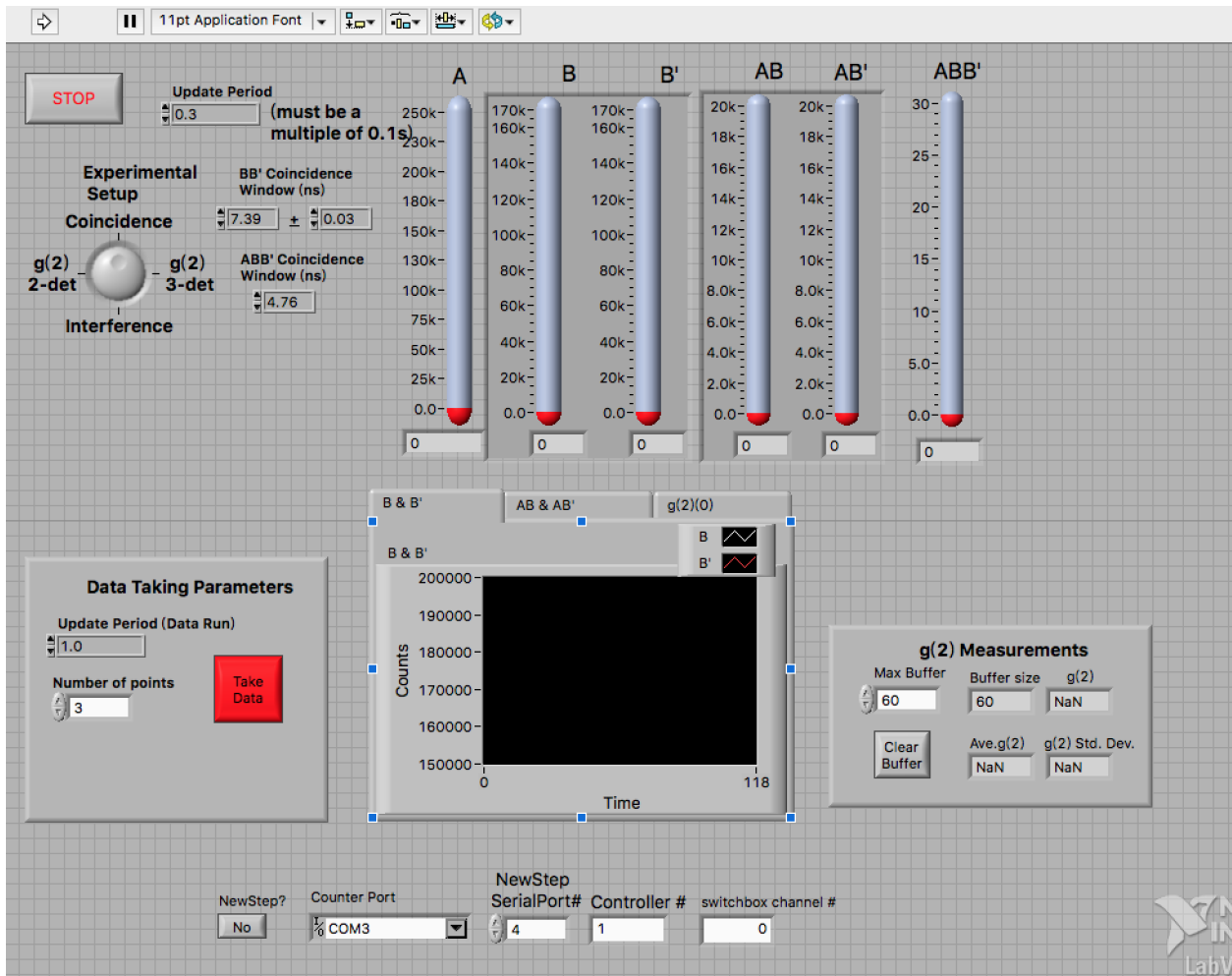


Figure 1.8: Screen shot of the *LabVIEW* program called “coincidence-rs232.vi,” for exploration of SPDC statistics.

In Fig 1.8, vertical “thermometer” scales provide a highly visible measure of the number of counts

we are detecting, which is useful during interactive alignment and optimization, as they can still be easily seen while working on the far side of the optical table. While the program is running, the maximum range of each thermometer can be adjusted by the user to fit the range of the counts actually coming from the detectors. Beneath these thermometer-style indicators are boxes which report the actual number of counts counts.

If all optical and electronic path lengths in the experiment are equal, the down-converted photon pairs should arrive at the detectors at exactly the same time, and the “coincidence window” should then be set to be an infinitesimal time interval. However, due to unavoidable variations in the propagation delays (including any delay associated with the electronics internal to the SPAD modules), there needs to be certain amount of tolerance. Default settings should suffice for our experiments, though students have the ability to explore the effects of varying any of these parameters. The temporal interval considered to amount to “coincidence” can be adjusted on the left of the screen (see “Coincidence Window” controls).

We can take data using the control panel on the lower left part of the interface. When taking data, an additional *LabVIEW* front panel will open, with corresponding adjustable parameters for saving data.

1.3.2 Aligning the sub-systems

Walking the beam

The path along which the pump beam propagates is referred to as the optic axis. Wherever this reaches an element where alignment is critical, it is helpful to set things up such that the optical axis aligns with the holes on the optical breadboard. To do this, as shown in Fig 1.9, a pair of steering mirrors is used to align the beam to a pair of identically mounted iris apertures.

The alignment process, colloquially referred to as “walking the beam,” first uses the mirror farther from the first iris to center the beam on the first iris. After the beam is centered there, use the mirror that is closer to the first mirror to center the beam on the second iris (on the right in Fig. 1.9). Then go back to the first iris and repeat the process. The process will converge more rapidly if each step includes some degree of *overshoot*, which decreases with each iteration. Once the beam

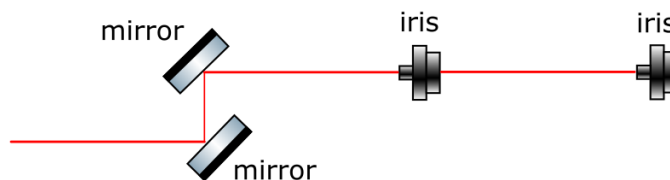


Figure 1.9: Aligning the optical axis to the optical breadboard

is centered on both irises, the irises can be removed.

Aligning the GTP, the half-wave plate and the BBO crystal

The alignment process for each of these components is as follows: place the component into the beam and rotate it, slightly, until the back-reflection coincides with the incidence beam. For BBO crystal, though, this “rough” alignment does not provide sufficient phase matching. After aligning the collection optics we will return to make fine adjustments to the vertical tilt of the crystal, so as to maximize the counts.

Aligning the collection optics

Given our prediction for the angle of separation, the two collection optics modules should be set into positions such that the line drawn between each collection optic and the crystal has a 2.8 degree separation with the optical axis, which, again, is the axis along which the pump beam is propagating. In my setup, the horizontal distance between the collection optics and the crystal is a hair under 38 inches. Thus the collection optics should be separated from the optical axis by approximately 1.85 inches. This quick trigonometry is only intended to provide us with a starting point, likely to give a signal which can be maximized experimentally, as the positions of the collection optics modules must be adjusted so as to maximize the counts.

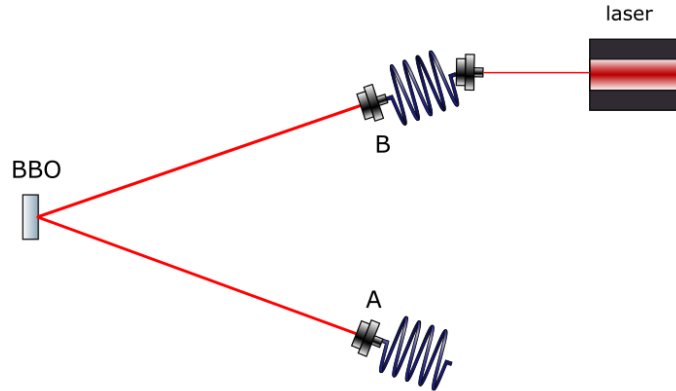


Figure 1.10: Adjust the pointing direction of the collection optics modules via back-propagation of a visible-wavelength fiber-coupled laser

The down-converted beam is too dim for human eyes to see, both because the wavelength is outside the range of peak sensitivity for human eyes, and because the intensity of the beam is quite low. So, our first step, shown in Fig. 1.10, is to use *back-propagation* of a fiber-coupled visible-wavelength laser, to make sure that the module containing the collection optics is aimed towards the BBO crystal.

The BBO crystal acts like a mirror, and it reflects the visible-wavelength alignment laser onto the second collection optics module. Once that part of the system is aligned, turn off the alignment laser, uncouple the fiber from the first collection optics module and connect that module to the fiber optics leading to the SPAD detector. (Again, the optical fiber that is directly connected to the SPAD must be opaque.) Then turn off all the lights in the room, except for the (green) LED safe light. After turning on the warning light in the hallway, it is safe to apply power to the SPAD detectors. There should always be some counts from the detector. Even with no light applied to the input, the SPAD will trigger about 100 times per second (which we call “dark counts”). IF you now turn on the 405 nm laser, you can maximize the detected counts by moving the collection optics modules vertically, first. Then tweak the tip/tilt angles of the collection optics modules to further maximize the counts. Next, further maximize the counts by making fine adjustments to the tilt the BBO crystal and to the rotation of the half-wave plate. Normally, when the system is aligned, the coincidence counts should be of order several thousand per second, for our single BBO crystal.

The SPDC setup described so far is relatively basic, but is also the most fundamental of all the quantum optics experiments I describe in this thesis. Other experiments are largely built upon this setup, with some additional components. Thus, for later experiments, I will not go in details of the basic alignment process except for experiment-specific alignments. Learning to align the system well, at this point, will lay a firm foundation for future experiments in quantum optics, and these alignment skills have value that extends well beyond quantum optics.

1.4 Establishing that we have a true Single-Photon Source

1.4.1 Introduction to Quantum Optics

As seen in the previous section, our detectors count discrete events where energy has been deposited. In quantum mechanics, we say that light is quantized into particles called photons. This granular aspect of light is distinctively different from the classical wave model, which would involve a continuous distribution of energy over spatially extended regions. For example, if a photon in a random polarization state is coming into a polarizing beam splitter (PBS), the statistics gathered in our quantum optics experiments suggest that it will either get reflected by or get transmitted through the PBS. If there are detectors in both directions, we expect no coincidence counts between them, so long as we can show that there was not more than one photon in the system at a time. However, that final qualifier requires special attention: photons are bosons, and therefore have a statistical tendency to “bunch,” meaning that even if you have an *average* of one photon in the path to your detector per millisecond, it is probably more commonly the case that you would have two photons arriving *together*, sometime during a two-millisecond interval. In other words, there is a likelihood, with traditional light sources, that on those (rare) occasions when you do have a photon you also have more than one, and so your experiments cannot then be taken to have uncovered any true single-photon effects. As a result, during a measurement of the sort described at the start of this paragraph, during the coincidence window there will be (distinct) photons reflected and transmitted from the PBS, obscuring what any single photon might do.

A correlation function for two-detector measurement

If we really want to explore single-photon physics, we need to establish a metric to demonstrate whether a dataset corresponds to single photons or bunched combinations. Single photon sources are essential to quantum optics and quantum information processing, as they are performing operations at the single photon level.

A metric that we will explore is shown in equation 1.19, provided in Mark Beck’s book: [6]

$$g_{B,B'}^{(2)}(\tau) \equiv \frac{\langle I_B(t + \tau)I_{B'}(t) \rangle}{\langle I_B(t + \tau) \rangle \langle I_{B'}(t) \rangle} \quad (1.19)$$

Consider a stream of intensity measurements taken at a sequence of times. Here, we can consider non-consecutive measurements in our data stream by considering results separated by a time delay, τ , where the angle brackets indicate we are averaging the results over the entire data set (all times). B and B' are SPADs on the transmission and reflection sides of the PBS, respectively. Such a “correlation function,” is one way of looking for patterns, or “hidden treasures” inside data. If the intensity signals at two detectors are independent (uncorrelated, and random), then our correlation function would yield a result of 1. Deviations from unity are indications time correlations (or anti-correlations) in the intensity detected by the two SPADs. There is a similar correlation function, used for thinking about the visibility of interference fringes, which looks at electric field amplitude rather than the intensity and so, by convention, the version that looks at correlations in the field is called the “first-order” correlation function while the one we are concerned with, which looks for correlations in intensity, is called the “second-order” correlation function.

Because of our concern over “photon bunching,” we want to consider the likelihood of *simultaneous* contributions to the intensity, *i.e.*, the limit where $\tau = 0$: [6]

$$g_{B,B'}^{(2)}(0) = \frac{\langle I_B(t)I_{B'}(t) \rangle}{\langle I_B(t) \rangle \langle I_{B'}(t) \rangle} \quad (1.20)$$

For our experiments, we note that the intensity of a beam is related to the probability of photon arrival. As we will see, while a lack of correlation yields $g_{B,B'}^{(2)}(0) = 1$, if the probabilities for arrival at the two detectors were perfectly correlated then the correlation function would be 2, and if they are instead perfectly anti-correlated, then the correlation function will yield 0. [6]

The probability of measuring a single photon from a single detector is proportional to the average intensity of the beam multiplied by the time window of detection. In equation 1.21, below, Δt is the time window for measurement, and e_B and $e_{B'}$ are the quantum efficiencies of the detectors.

[6]

$$\begin{aligned}
P_B &= e_B \langle I_B(t) \rangle \Delta t \\
P_{B'} &= e_{B'} \langle I_{B'}(t) \rangle \Delta t \\
P_{BB'} &= P_B P_{B'} = e_B e_{B'} \langle I_B(t) I_{B'}(t) \rangle \Delta t^2
\end{aligned}
\tag{1.21}$$

Note that the average of the product of the intensities at two detectors, *i.e.*, the coincidence count rate, is related to the joint probability of measurement. By substituting Equation 1.21 into Equation 1.20, we see: [6]

$$g_{B,B'}^{(2)}(0) = \frac{P_{BB'}}{P_B P_{B'}} \tag{1.22}$$

However, we still have not yet written our correlation function in terms of quantities that can be directly measured during an experiment. If the total time of measurement is T , and the total number of photons detected during that interval is N , then the probability of measuring a photon coming into the detector is equal to the rate of photon detection, N/T , times the measurement window, Δt : [6]

$$\begin{aligned}
P_B &= N_B \frac{\Delta t}{T} \\
P_{B'} &= N_{B'} \frac{\Delta t}{T} \\
P_{BB'} &= N_{BB'} \frac{\Delta t}{T}
\end{aligned}
\tag{1.23}$$

Substitute into equation 1.22, and we can get equation 1.24. [6]

$$g_{B,B'}^{(2)}(0) = \frac{N_{BB'}}{N_B N_{B'}} \left(\frac{T}{\Delta t} \right) \tag{1.24}$$

Now, everything in this version of our correlation function is measurable in our experiments. There should be no, or very little coincidence count, if we have a true single-photon source. In that situation, we say that we have a source that exhibits “anti-bunching”, in that $g_{B,B'}^{(2)}(0)$ is very close to zero. However, if our source is merely equivalent to a highly attenuated, conventional laser light source, the joint probability of measurement should be very close to the product of individual probability of measurement. As a result, $g_{B,B'}^{(2)}(0)$ will be very close to one. On the other hand, if we have a thermal light source, statistical physics assures us that photon-bunching will be commonplace and $g_{B,B'}^{(2)}(0)$ will be close to two. [6]

“Heralded” measurements

In the experiment discussed above, we considered a PBS and two detectors, one for photons transmitted by the PBS and one receiving photons reflected toward it by the PBS. As we will demonstrate, if the input to the PBS is the “signal” beam resulting from Spontaneous Parametric Down-Conversion (SPDC), then $g_{B,B'}^{(2)}(0)$ will be very close to one, implying that the “signal” beam is no better than a conventional light source. On the other hand, if retain, from our data set, only photon detection events that arrive, within a coincidence window, at the same time that a photon arrives from the “idler” beam, then $g_{B,B'}^{(2)}(0)$ will be very close to zero, implying that the “heralded” signal photons constitute a true single-photon source. This difference between the un-heralded and heralded measurements of the signal beam persist even if we do everything possible to filter out the background noise, to eliminate any stray light scattered by the pump beam, and to address other extraneous factors under our control. Students should be encouraged to discuss this point in class, where possible.

The un-heralded version of our experiment with the PBS involved two detectors. The heralded version of this experiment adds a third detector, and all of the probabilities that enter our correlation function become conditional upon the coincident detection of an idler photon at the heralding detector, which we call A :

$$g^{(2)}(0) = \frac{P_{ABB'}}{P_{AB}P_{AB'}} \quad (1.25)$$

Because of the conditional nature of heralded measurement, we can treat the counts from detector A as the total number of photons, which simplifies the calculation of probabilities, as shown in equation 1.26:

$$\begin{aligned} P_B &= \frac{N_{AB}}{N_A} \\ P_{B'} &= \frac{N_{AB'}}{N_A} \\ P_{BB'} &= \frac{N_{ABB'}}{N_A} \end{aligned} \quad (1.26)$$

Substituting into equation 1.25, we can get equation 1.27 shown below, where all quantities are directly measurable in our experiments.

$$g^{(2)}(0) = \frac{N_A N_{ABB'}}{N_{AB} N_{AB'}} \quad (1.27)$$

1.4.2 Experimental setup for studying Source Statistics

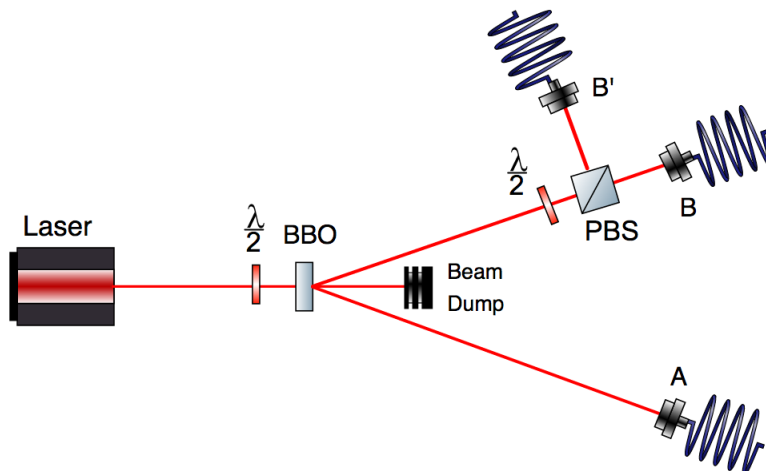


Figure 1.11: Setup for studying the statistics of an SPDC source (and, when heralded, demonstrating the existence of a true source of single, anti-bunched photons).

The experimental setup is shown in Figure 1.11. Some details discussed earlier, such as the GTP, the SPADs and the FPGA are omitted from the schematic for simplicity. Here, detector A is the heralding detector, and detector B and B' are the signal detectors. I put a half-wave plate right in front of the PBS to make the signal beam diagonally polarized. Because we use a single Type-I BBO crystal, when the pump beam is horizontally polarized, the down-converted photons are all vertically polarized, which means that without the addition of this half-wave plate all signal photons would be transmitted at the PBS. Rotating the half-wave plate allows us to tune (and equalize) the relative likelihood of detection at B and B' .

1.4.3 Alignment and Source Statistics data collection

This experiment requires you to have already completed the basic alignment of the SPDC described in Section 1.3. Following that, block the pump beam, turn off the detectors and couple the visible-wavelength fiber-coupled laser into detector B , as we did for back-propagation. During the alignment process which follows, the position of detector B should never be changed, as it is already aligned in the previous process. Next, add the PBS to the measurement arm, right in front of detector B , and adjust the orientation of the PBS such that the beam reflected from the PBS is concentric with the incidence beam. Turning the room light off is a good idea when doing this part of the alignment, simply to make it easier to see the reflected beam. Do the same thing with the half-wave plate. Then add detector B' on the other side of the PBS. The distance between detector B' and the PBS should be the same as the distance between detector B and the PBS, otherwise the differences in propagation times will lead to a reduction in the measured coincidence counts. The reflection of the visible-wavelength fiber-coupled laser should go into the center of detector B' . Once this rough alignment is completed, decouple the fiber-coupled laser and couple the SPADs into all the detectors, unblock the pump beam, start the computer program, and (only) with the room lights off, power up the SPADs. For fine-tuning the alignment, we use the same program that we used for SPDC measurement, “coincidence-rs232.vi.” Fine tuning of the alignment consists of adjusting the horizontal position of detector B' , as well as its tip and tilt, so as to maximize the measured counts.

Once the alignment is done, it's time to start our new experiment. For that purpose, the dial switch labeled “Experimental Setup” (shown on the left of Fig. 1.8) should be set first to “2-det,” to demonstrate that the un-heralded signal beam does not exhibit anti-bunching, and then later set to “3-det,” to show – at long last – that conditional (heralded) measurement really does provide us with a true (anti-bunched) single-photon source.

Table 1.1: (Un-heralded) two-detector measurement results

B	B'	BB'	$g_{BB'}^2(0)$
367424	289731	82	1.042
367374	289076	90	1.147
371363	293407	88	1.093
370220	292758	91	1.136
371277	293624	90	1.117
365820	287242	84	1.082
362172	280908	82	1.091
361905	280527	83	1.106
366356	283938	89	1.158
371093	294140	84	1.041
373758	295967	99	1.211
367948	288886	78	0.993
364676	282531	89	1.169
370556	292187	80	1.000
370335	293351	81	1.009

1.4.4 Experimental results on SPDC Source Statistics

Our results for the two-detector (un-heralded) measurements are shown in Table 1.1. Our average value for $g_{BB'}^2(0)$ is 1.09, with a standard deviation is 0.07. Again, this is consistent with a conventional, coherent laser light source. If that were the best we could do, there would be no point to going to the trouble of working with SPDC.

A much more important result emerges when we examine the results of our heralded (three-detector) measurement, shown in Table 1.2. Here, the average we observed for $g^2(0)$ is 0.023, and the standard deviation is 0.008. As noted earlier, the most extreme limit for anti-bunching would yield a $g^2(0)$ very close to 0. Within the quantum optics research community, a beam can be considered suitable for drawing conclusions about single-photon physics whenever the source statistics yield $g^2(0) < 0.5$. From our data, it is pretty clear that we have now established a single-photon source. (Some would go further, and declare that such experiments prove the existence of single photons.)

Table 1.2: Heralded detection results

A	B	B'	AB	AB'	ABB'	$g^2(0)$
1260093	366940	290100	18092	20027	7	0.024
1260867	366650	289091	17911	20101	6	0.021
1258648	367593	288875	17968	20150	6	0.021
1260537	367670	288265	17908	20052	6	0.021
1259656	365289	285618	17824	20122	11	0.039
1261006	363520	280707	18057	19991	7	0.024
1259442	362171	281408	18172	19839	5	0.017
1258713	364407	281734	18076	19986	5	0.017
1259301	363394	282878	18072	20047	4	0.014
1258607	364141	282112	17829	19982	8	0.028
1259844	363193	281983	18038	19877	3	0.011
1258621	362975	279806	17895	19886	8	0.028
1259322	362416	281659	17861	20179	5	0.017
1257997	364128	282412	18208	20015	11	0.038
1258766	360184	276274	18030	19975	8	0.028

1.5 Quantum State Measurement

1.5.1 Introduction to the Inverse Problem

Measuring the quantum state of a single photon can be arduous: it is an example of what physicists refer to as “an inverse problem.” A simpler example of an inverse problem is the game of “20 Questions.” In that game, your task is to invert the data and work out, say, “who I’m thinking of,” which is to say that you don’t “detect” the identity of the person *directly*. The answer to any one yes-or-no question doesn’t, normally, provide enough information to tell you who I’m thinking of. Strategically, you gain maximum information per question if each question that you pose eliminates half the population. If you take that approach, there is a decent chance that you will win, because 2^{20} is over a million.

As we move on to quantum, we have to recognize that the answers to some “yes-or-no” questions are *maybe*. Experimentally, our strategy will be to examine a stream of identically prepared single photons and, for each of them, ask questions pertaining to more than one type of basis state. Are you a horizontally polarized photon? Are you a vertically polarized photon? Are you a diagonal polarized photon? Are you an anti-diagonal polarized photon? Using the formalism presented in Mark Beck’s text, *Quantum Mechanics: theory and experiment*, these questions can be expressed as a matrix multiplying the state vector, and yielding the answers as a column vector.

You only need two basis states, *e.g.*, $|H\rangle$ and $|V\rangle$, in order to completely describe a general “spin” polarization state for a photon, $|\psi\rangle = a|H\rangle + be^{i\phi}|V\rangle$, but this means that in order to fully specify the state we have to experimentally determine the values of three quantities, a , b , and ϕ . Thus, in this section we will make three distinct kinds of measurements (with sufficient data to ensure decent statistics) in order to fully determine the polarization state of a stream of identically prepared single photons.

As an aside, it is worth noting that in Chapter 2 of this thesis we will describe experiments that we have done which demonstrate that a photon can also possess “orbital” angular momentum (OAM). Unlike the 2D Hilbert space associated with “spin” angular momentum, OAM requires us to consider a “higher-dimensional” space (limited to a finite number, D , only by the finite aperture of our experimental implementation). The use of higher-dimensional spaces is of interest for encoding large amounts of information but, when it comes to reading out that encoded information, solving

inverse problems in higher-dimensional spaces can be quite challenging. Again, experimentally, you measure probabilities for D independent basis states (plus noise, and so you can get “unphysical” answers if you haven’t taken enough data to ensure decent statistics), but the need to establish the relative phases means that, in general, you need $2D - 1$ distinct kinds of measurements. Thus, there is current interest in the development of special tricks for simplifying the characterization of higher-dimensional quantum states. (One such approach is addressed in Section 2.5 of this thesis).

That said, in this section, we confine ourselves to measuring the polarization state of single photons prepared by the heralding method described in the previous section, where, in order to ask questions pertaining to more than one type of basis state, we will perform three distinct kinds of measurements, involving a quarter-wave plate, a half-wave plate, and a polarizing beam splitter. The wave plates allow us to changing the basis of the photon state and the polarizing beam splitter is for projecting the photon state onto the $|H\rangle$ axis.

Again, a general polarization state of a photon can be written, in bra-ket notation, as follows:

$$|\psi\rangle = a|H\rangle + be^{i\phi}|V\rangle \quad (1.28)$$

In order to measure the state of the photon, the coefficients a , b , and ϕ must to be experimentally determined. Here, a and b are the probability *amplitudes* for detecting the states $|H\rangle$ and $|V\rangle$, if we pass such a photon through an HV polarization analyzer (*i.e.*, a PBS with appropriate orientation). We have already described measurements using a PBS, and so we are clearly prepared to measure the probability of getting $|H\rangle$ out of the PBS. Because the input stream contains identically prepared photons that are in the state $|\psi\rangle$, the measured probability is a conditional probability, $P(H||\psi)$: this is the probability that we will measure a horizontally polarized photon, given that the beam is prepared in the state $|\psi\rangle$. From this measured probability we can calculate the probability amplitude, a , using Equation (1.5.3).

$$a = \sqrt{P(H||\psi)} \quad (1.29)$$

As soon as the value of a is measured, the value of b can be determined. Normalized mandates the relationship between a and b be as shown in Equation (1.5.2):

$$a^2 + b^2 = 1 \quad (1.30)$$

Thus,

$$b = \sqrt{1 - a^2} \quad (1.31)$$

To determine the phase factor, ϕ , we need to measure the polarization of the beam using different basis. First we will measure the polarization state of the beam using the $\pm 45^\circ$ basis and then we will perform an analogous measurement using the LR circular polarization basis. The relation between these measurements and the desired coefficients is shown in Equation 1.23 and 1.24.

$$P(+45|\psi) = |(\langle +45|\psi \rangle)|^2 = \frac{1}{2}(1 + 2ab\cos\phi) \quad (1.32)$$

$$P(L|\psi) = |(\langle L|\psi \rangle)|^2 = \frac{1}{2}(1 + 2ab\sin\phi) \quad (1.33)$$

As a result, we can calculate the angle ϕ using Equation 1.25.

$$\begin{aligned} \phi &= \arctan\left(\frac{\sin\phi}{\cos\phi}\right) \\ &= \arctan\left(\frac{P(L|\psi) - \frac{1}{2}}{P(+45|\psi) - \frac{1}{2}}\right) \end{aligned} \quad (1.34)$$

After we have experimentally determined the values of a , b and ϕ , we can substitute them in Equation 1.19, yielding the full expression of the quantum state of the input photons.

1.5.2 Experimental setup for Querying Single-Photon States

This experiment has largely the same setup as in Sect. 1.4, except that there is a quarter-wave plate added. Again, in Fig. 1.12 common features, such as the GTP, the SPAD and the FPGA have been omitted for simplicity. A half-wave plate and a quarter-wave plate are added to the measurement arm. Rotating the wave plates to certain angles can change the basis states for our polarization measurements, as detailed in Table 1.3.

Table 1.3: Wave plate settings to establish each measurement basis

Basis	Fast axis of quarter-wave plate	Fast axis of half-wave plate
HV	0°	0°
LR	45°	0°
± 45	45°	22.5°

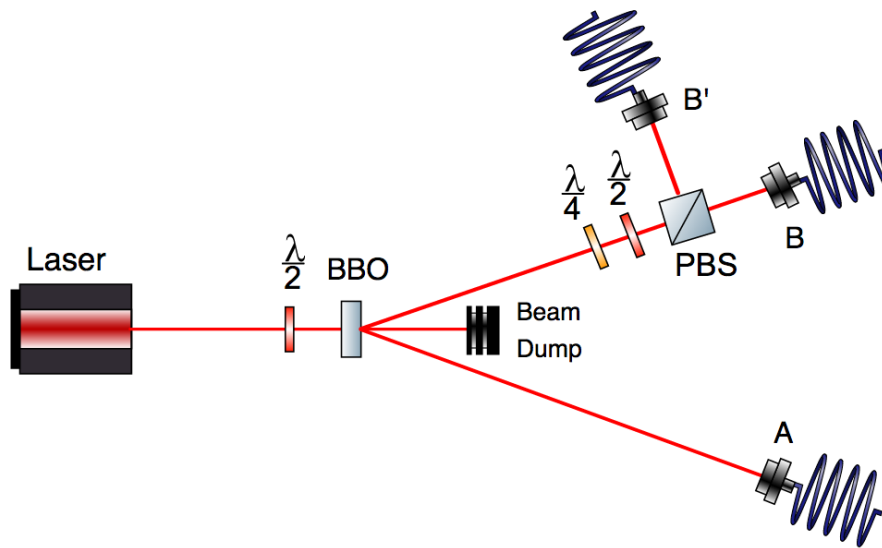


Figure 1.12: Quantum state measurement schematic

1.5.3 Alignment and Quantum State data collection

The only new twist here is that, in order to switch from measurement basis to measurement basis, we first need to find the fast axis orientation for each of the wave plates. When a wave plate is rotated so that its fast axis is aligned with the polarization of the input beam, it will not change the state of the beam. All of the angles listed in Table 1.3 are understood to be *relative* to this orientation of the wave plates.

As a first step, place a polarizer into the 405-nm pump beam, and add an imaging screen beyond the polarizer. Rotate the polarizer until the output is dimmest. The reason we start out with the dimmest light is that human eyes are logarithmic detectors, and are most sensitive to the change of brightness when the light is dim. Next, put one of the wave plates to be used in this experiment in front of the polarizer. Rotate the wave plate to return the output on screen to its dimmest limit. Now the wave plate is at its “zero angle,” and the reading on its rotary mount should be

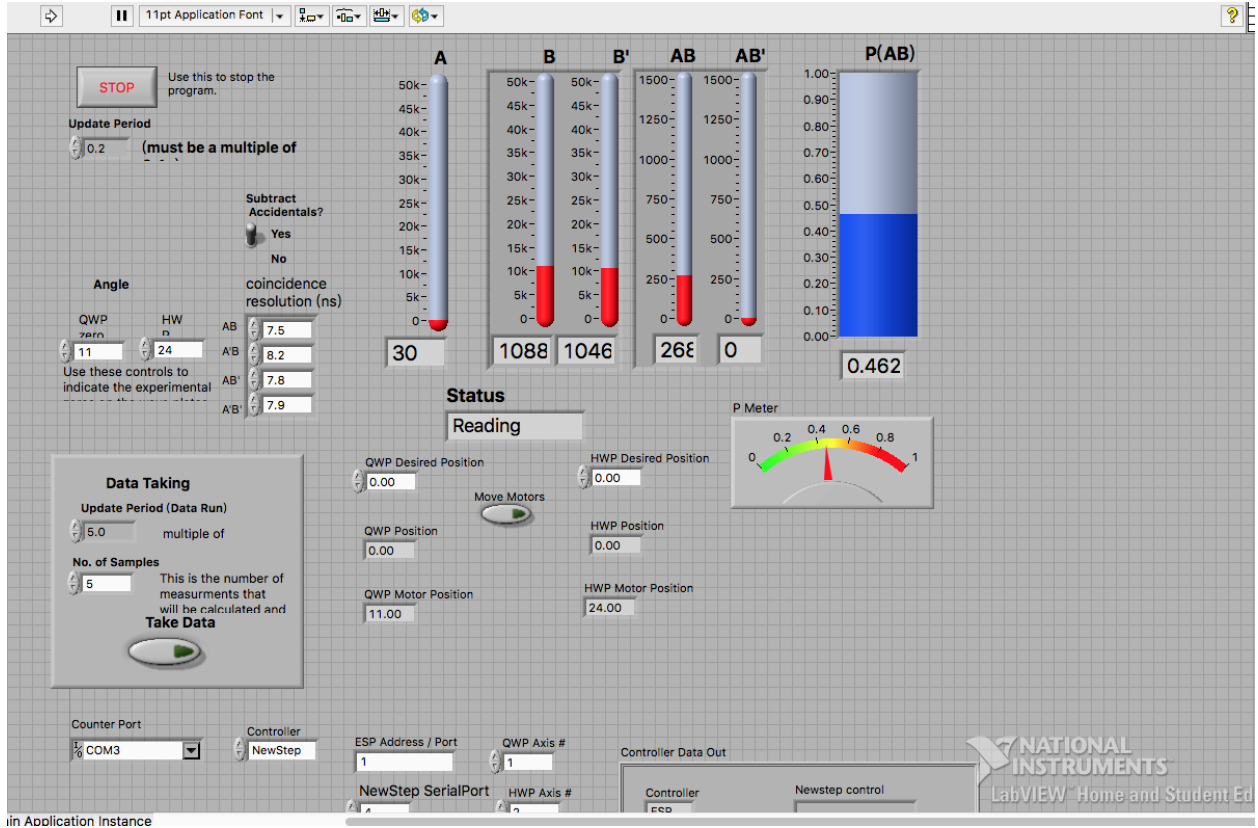


Figure 1.13: QSM-rs232.vi front panel

noted. Once the wave plates are thus characterized, they can be put in place, following which, the alignment process for each waveplate is the same as was described in Section 1.4.3.

To collect data, we use Mark Beck's *LabVIEW* program "QSM-rs232.vi." The interface is shown in Figure 1.13. It should be noted that the conditional probabilities $P(H|\psi)$, $P(L|\psi)$, and $P(+45|\psi)$ can each be calculated using the method of Section 1.4:

$$P(AB) = \frac{N_{AB}}{N_{AB} + N_{AB'}} \quad (1.35)$$

1.5.4 Experimental results for Quantum State Measurement

Our experimental results for each individual measurement basis are shown in Table 1.4, 1.5 and 1.6.

Table 1.4: Measurement results in the HV basis

A	B	B'	AB	AB'	ABB'	$g^{(2)}$
122232	43836	35510	1702	3815	0	0.000
122480	43736	35416	1732	3896	1	0.018
122011	43940	35552	1765	3920	0	0.000
122217	43584	36028	1716	3957	2	0.036
122523	44284	35344	1770	3882	0	0.000
122638	43552	35332	1765	3994	1	0.017
122460	43871	35263	1764	3891	4	0.071
122280	43810	35304	1756	3971	3	0.053
122591	43799	35309	1721	3946	4	0.072
122900	43606	35218	1745	3936	2	0.036

Table 1.4 provides our results in the HV basis, for which the average for N_{AB} is 1743.6, and the average for $N_{AB} + N_{AB'}$ is 5664.4. By referring back to Equation 1.29 we can get $a = 0.555$, and using Equation 1.31 we can get $b = 0.832$.

Table 1.5: Measurement results in the LR basis

A	B	B'	AB	AB'	ABB'	$g^{(2)}$
122913	6280	61526	31	4846	1	0.818
123320	6336	61999	33	4857	0	0.000
123236	6419	62398	36	4986	0	0.000
123583	6296	61986	25	4819	1	1.026
124151	6243	62089	40	5034	0	0.000
123600	6299	62254	28	4896	0	0.000
123160	6220	61605	36	4906	0	0.000
123021	6399	61889	38	4799	0	0.000
122245	6305	62163	31	4944	0	0.000
123735	6294	61928	40	4924	0	0.000

From Table 1.5, the results in the LR basis give an average for N_{AB} is 33.8, and an average for $N_{AB} + N_{AB'}$ is 4934.9, so $P(L|\psi) = 0.0068$. From Table 1.6, our measurements in the ± 45 basis yield the average for N_{AB} is 2805.6, and the average for $N_{AB} + N_{AB'}$ is 5237.1, so $P(\pm 45|\psi) = 0.536$. Then using Equation 1.34 we can get $\phi = -0.48\pi$. At this point, we have

Table 1.6: Measurement results in the ± 45 basis

A	B	B'	AB	AB'	ABB'	$g^{(2)}$
122052	49966	30432	2718	2437	1	0.018
122040	49986	30374	2877	2449	0	0.000
123244	49983	30517	2797	2400	1	0.018
122613	50171	30761	2790	2403	2	0.037
122439	50218	30561	2791	2532	0	0.000
122553	50431	30561	2857	2359	0	0.000
122781	50184	30246	2903	2358	1	0.018
122163	50186	30831	2743	2547	0	0.000
121885	50242	30509	2733	2371	1	0.019
121612	50136	30586	2847	2459	3	0.052

solved the inverse problem, and have experimentally determined the quantum state of the down-converted beam to be:

$$\psi = 0.555|H\rangle + 0.832e^{-0.48\pi i}|V\rangle \quad (1.36)$$

Equivalently, this single-photon state may be written in a form that explicitly reflects the angular momentum content:

$$\psi = 0.198|L\rangle + 0.980e^{-0.15i}|R\rangle \quad (1.37)$$

1.6 Bell’s test of Local Realism

1.6.1 Introduction to Quantum Weirdness

In 1935, Einstein, Podolsky, and Rosen (hereafter, EPR), wrote a paper proposing a paradox intended to undermine the notion of quantum superposition. In the paper, by exploring a *gedanken* experiment, they came up with an idea, later termed (by Schrödinger) “quantum entanglement.” Einstein referred to the consequences as “spooky, action-at-a-distance,” pointing out the implications for faster-than-light effects which seemed as though they held the potential to violate the inviolable principles established by the theory of Special Relativity. Thus, it *seemed* quantum mechanics must be flawed. The EPR paper suggested that what had previously been taken to be a quantum superposition was, instead, a “mixed state,” where each individual quantum entity must have been in a definite state before measurement. This struck at the core of quantum mechanics, including the uncertainty principle and the probabilistic Copenhagen interpretation of the wavefunction. The EPR “paradox” regarded the reality of quantum superposition *prior* to measurement, and so seemed unresolvable. The debate remained a rather philosophical one, until John Bell, an Irish physicist and mathematician, carefully examined the implications of the EPR paradox 30 years later, in a context which suggested that people could actually perform experiments to prove the existence of quantum superposition. In this section, I am first going to describe, rather intuitively, the EPR *gedanken* experiment and Bell’s contribution, and then recount the particular test of Bell’s inequality that I performed, in an undergraduate laboratory in University of Urbana-Champaign, using down-converted photon pairs, with supervision from quantum optics pioneer Prof. Paul Kwiat and Chris Zeitler, a Ph.D student in Prof. Kwiat’s research group. Loophole-free tests of Bell’s inequality have only been presented in the research literature within the past year or so, and the field of quantum optics continues to provide key new insights.

Suppose we have an SPDC setup that produces down-converted photon pairs that fly off to detectors on each of the measurement arms associate with the experiments we have described in previous sections. At the end of Section 1.2, we established that, when using a single Type-I crystal, the down-converted photons must have the same polarization as one another (and that polarization must be perpendicular to that of the pump beam). While the down-converted photons produced

in that way are, in an important sense, entangled, they are not *polarization* entangled, in that the polarization part of their two-body wavefunction may be written in factorable form. So, in order to create polarization-entangled states, for this section we will instead use a *double* Type-I BBO crystal, a geometry invented by Prof. Kwiat and his collaborators. This involves placing two (thin) Type-I BBO crystals into optical contact, oriented such that their optical axes are rotated by 90° with respect to each other, and by 45° with respect to the polarization of the pump beam. In this case, the pump beam may be considered a superposition of $|H\rangle$ and $|V\rangle$ states, and one crystal holds the possibility of converting horizontally polarized pump photons into vertically polarized signal and idler photons, while the other crystal can convert vertically polarized pump photons into horizontally polarized output photons. So long as the thickness of the crystal is small compared to the coherence length, the downconverted photons are produced in a superposition: $|\phi\rangle = \frac{1}{\sqrt{2}}(|H, H\rangle + |V, V\rangle)$, which cannot be factored into separate states corresponding to the signal and idler photons. In other words, it no longer makes sense to speak of these two photons as being in separable polarization states: their polarization degrees of freedom are said to be entangled, and the polarizations of the down-converted photon pairs are superpositions of $|H\rangle$ and $|V\rangle$ states before measurement, or at least, this is what the Copenhagen interpretation implies. Moreover, the SPDC process described at the end of Section 1.2 ensures that the polarizations of these photon pairs are *correlated* (always the same), and that must remain true regardless of which measurement basis we use in our experiments, *e.g.*, the HV basis or the ± 45 basis (a point which becomes central in Section 1.6.2). This is a distinctly non-classical prediction, and so we have created an interesting system for examining the questions raised by the EPR paper.

Suppose we place a polarizer in front of each detector. If both polarizers are set in the vertical direction, then it is still possible to have coincidence counts at the two detectors. The same would hold true if both polarizers were horizontal. However, if I change one of them to horizontal direction, there should no longer be coincidence counts. Again, as described at the end of Sect. 1.2, the SPDC process was constrained, by conservation of momentum, in a way that requires both of the down-converted photons to have the same polarization. Here's a key point: measurement of polarization of one of the photons will reveal, instantly, the polarization state of the other, regardless of how far our detectors are from the source (and therefore how far they are from each other).

In the Copenhagen interpretation, measurement effectively “collapses” the wavefunction into the measured result, but according to any interpretation of quantum mechanics we cannot describe either photon as being in a particular polarization state *before* measurement. Thus, the information of the collapsing of polarization state of one, measured photon somehow travels instantly to the other photon and makes it collapse. For Einstein, this seemed a clear violation of the theory of Special Relativity, which insists that all information must travel at speeds less than or equal to the speed of light in vacuum. Therefore, he concluded that quantum superposition was an illusion, and that prior to measurement each of the photons must have a definite polarization state. According to this alternative to the quantum theory and the intrinsic indeterminacy it contains, the EPR paper suggested that it is only our lack of detailed experimental information about the system that leads us to the (errant, to their view) notion of quantum superposition, when the ensemble of photons sampled over extended data collection would be more appropriately described as containing a mixture of well-defined states. It’s similar to the situation of traveling with one glove from a pair, sealed inside a suitcase. If I open the suitcase and find that it is right-handed, I immediately figure out that the other one, which I left at home, is left-handed. From Einstein’s point of view, the glove in my suitcase has always been right-handed. It is never truly in a superposition state of “handedness.”

All of these arguments from Einstein and his colleagues are very intriguing, but for many years it appeared that there could hardly be any way to test it. So, it came as a huge surprise to the scientific community when, in 1964, John Bell proposed a *gedanken* experiment of his own, which established that such a test should be, in principle, possible. Actual experimental implementations of these tests took much longer to achieve, with the most compelling, “loophole-free” versions only reported quite recently. So, rather than describing Bell’s original version, I will translate the problem into language appropriate to our quantum optics experiments.

Instead of rotating the polarizers in front of our detectors into either a horizontal or vertical position, we can rotate one of them to some random direction and see what can happen to our measured results. Suppose that, as a preliminary, we begin with both polarizers aligned, so as to maximize coincidence counts, to some level we’ll call a . We may consider this to be, say, the horizontal di-

rection, marked as 0° rotation. Next, let's rotate one of the polarizers, A , to 30° , leaving the other one, B , at 0° . By the Law of Malus, which amounts to projection of the field onto the analyzer axis, the coincidence count should fall to $a * \cos^2 30^\circ = 3a/4$, implying that there are $a/4$ photon pairs being blocked by the polarizer. We denote this as follows:

$$N(30, 0) = \frac{1}{4}a \tag{1.38}$$

If I rotate A back to 0° and rotate B to -30° , the coincidence count is again $a * \cos^2(-30^\circ) = 3a/4$, and so there are, again, $a/4$ photon pairs being blocked by the polarizer. We denote this result as:

$$N(0, -30) = \frac{1}{4}a \tag{1.39}$$

Suppose now I rotate polarizer A to $+30^\circ$ and polarizer B to -30° . If Einstein's view is correct, then number of photon pairs blocked by the polarizers should now either be equal to the sum of $N(30, 0)$ and $N(0, -30)$, or it could be something less than that. In other words, there could be some overlap between the two sets of photon pairs that are blocked by the two polarizers. We can denote this by the inequality 1.39, which is, in essence, the Bell's inequality:

$$N(-30, 30) \leq N(30, 0) + N(0, -30) \tag{1.40}$$

Quantum mechanics violates this prediction, arguing instead that before a measurement is performed, individual photons are in a true superposition of polarization states, for which there is no predetermined measurement basis. The point of that final clause is that, according to quantum mechanics we expect the $(-30, 30)$ case to be equivalent to one where the first polarizer is at 0 degrees and the other one at 60 degrees, so $N(-30, 30) = 1 - \cos^2(60^\circ) = 3/4$, which is larger than $1/2$ calculated as the limiting value allowed if Einstein's view were correct. In other words, we have a testable situation which can, potentially, whether true superposition exists or not before measurement. (As will be shown by our experimental results, it does.)

1.6.2 The CHSH inequality

Are there pre-existing "results" associated with superposition states before measure-

ment?

In 1969, Clauser, Horne, Shimony and Holt published a paper and proposed a variation of the Bell's inequality, the CHSH inequality, designed to be more experiment-friendly. Below, the CHSH inequality is re-derived, to facilitate later discussions of our experiment. By showing that the superposition state has the same mathematical form when we switch the measurement basis, we can prove the idea that a pre-existing measurement basis does not exist.

At the start of Section 1.6.1, we argued that would could produce a pair of polarization-correlated photons in "Bell's state," which is shown below:

$$|\psi_{EPR}\rangle = \frac{1}{\sqrt{2}}(|H\rangle_s|H\rangle_i + |V\rangle_s|V\rangle_i) \quad (1.41)$$

Here, subscripts have been explicitly added to identify the signal and idler photons.

Next, let us switch to a different measurement basis by rotating the H and V basis by an angle a . The transformation is shown below.

$$\begin{aligned} |H_a\rangle &= \sin(a)|H\rangle + \cos(a)|V\rangle \\ |V_a\rangle &= \cos(a)|H\rangle - \sin(a)|V\rangle \end{aligned} \quad (1.42)$$

If we substitute equation 1.41 into equation 1.40, after a bit of manipulation we can get:

$$|\psi_{EPR}\rangle = \frac{1}{\sqrt{2}}(|H_a\rangle_s|H_a\rangle_i + |V_a\rangle_s|V_a\rangle_i) \quad (1.43)$$

which has the same mathematical form as equation 1.40. Thus, the probability for measuring the system in state $|H_a\rangle_s|H_a\rangle_i$ is the same as $|H\rangle_s|H\rangle_i$, showing that there is no difference regarding which specific measurement basis we choose. As a result, there is no pre-existing measurement basis for quantum mechanical superposition states. That would not be the case for a classical mixed state of the sort the EPR paper promoted.

Quantitative metrics entering the CHSH inequality

Einstein insisted that each individual particle is in a definite state before the measurement, and that it is only our lack of knowledge of some hidden variable of the system that gives us the illusion that the system is in a superposition state. According to Einstein's view, the measurement results for one of the detectors can only be determined by the settings of the detector and the local hidden

variable, λ . In our experiment, we assign the polarizers the role of detectors (absorbers), and the settings of these detectors are simply the orientations of the polarizers. The hidden variable is more or less a metaphysical quantity: it affects the outcome of measurements of the entangled pairs of photons, and it varies according to unknown physics laws.[14] Essentially, λ must act as a randomizing variable, leading to the apparent indeterminacy observed in experiment, and in order to lead to a more quantitative discussion, we assign values ± 1 to each of our observable outcomes, at each detector, and imagine that λ also takes on values of ± 1 , distributing the measured values according to a probability $\rho(\lambda)$, where normalization dictates:

$$\int \rho(\lambda) d\lambda = 1 \quad (1.44)$$

The result of one single measurement of the polarizer A is denoted by $A(\lambda, a)$, and $B(\lambda, b)$ for detector B . A type of **correlation function** can then be constructed, using the products of the outcomes – a bit along the lines of $g_{B,B'}^{(2)}(0)$, but instead of averaging a product of intensities, which can take on any value, and then normalizing the function, we simply examine the statistical average of the product of $A(\lambda, a)$ and $B(\lambda, b)$:

$$E(a, b) = \int A(\lambda, a) B(\lambda, b) \rho(\lambda) d\lambda \quad (1.45)$$

As we will see, the range of the correlations will differ, depending upon whether we have a quantum superposition or an EPR mixture.

First, though, we need a few more definitions in order to derive the CHSH inequality. Let ϕ_A and ϕ_B represent the settings of the polarizers. If, for example, we require that the two polarizers are either in state $|H_a\rangle$ or in state $|V_a\rangle$, we might assign $|H_a\rangle$ the value -1 and $|V_a\rangle$ the value +1. The probability of a coincidence detection between detectors A and B is normally denoted in terms of projections onto the basis states corresponding to the polarizer settings:

$$P_{\phi_A \phi_B}(a, b) = |\langle \phi_{A,a} | \langle \phi_{B,b} | \psi_{EPR} \rangle|^2 \quad (1.46)$$

However, using our newly defined numerical quantities associated with the polarizer settings, ϕ_A and ϕ_B , along with the measurement quantities $A(\lambda, a)$ and $B(\lambda, b)$, we can re-write the probability of the coincidence detection between detector A and B as follows:

$$P_{\phi_A \phi_B}(a, b) = \int \frac{1 + \phi_A A(\lambda, a)}{2} \frac{1 + \phi_B B(\lambda, b)}{2} \rho(\lambda) d\lambda \quad (1.47)$$

For two polarizers, there are four possible combinations of settings, if we require that the two polarizers are either in state $|H_a\rangle$ or in state $|V_a\rangle$. For each of those combinations, we can explicitly write down the probability of a coincidence detection between detector A and B :

$$\begin{aligned}
P_{VV}(a, b) &= \int \frac{1 + A(\lambda, a)}{2} \frac{1 + B(\lambda, b)}{2} \rho(\lambda) d\lambda \\
P_{VH}(a, b) &= \int \frac{1 + A(\lambda, a)}{2} \frac{1 - B(\lambda, b)}{2} \rho(\lambda) d\lambda \\
P_{HV}(a, b) &= \int \frac{1 - A(\lambda, a)}{2} \frac{1 + B(\lambda, b)}{2} \rho(\lambda) d\lambda \\
P_{HH}(a, b) &= \int \frac{1 - A(\lambda, a)}{2} \frac{1 - B(\lambda, b)}{2} \rho(\lambda) d\lambda
\end{aligned} \tag{1.48}$$

As a result, we gain the following relationship between the correlation function and the probability of a coincidence detection between detector A and B .

$$E(a, b) = P_{VV}(a, b) + P_{HH}(a, b) - P_{VH}(a, b) - P_{HV}(a, b) \tag{1.49}$$

At this point, we see that the correlation function varies from +1 when the polarizations are always the same to -1 when the polarizations always differ.

Finally, if we expand our detector settings options, and let a , a' , b and b' be four different detector settings, we characterize the polarization correlation in a single pair of particles via a **parity** function[10]:

$$\begin{aligned}
s &\equiv A(\lambda, a)B(\lambda, b) - A(\lambda, a)B(\lambda, b') + A(\lambda, a')B(\lambda, b) + A(\lambda, a')B(\lambda, b') \\
&= A(\lambda, a)[B(\lambda, b) - B(\lambda, b')] + A(\lambda, a')[B(\lambda, b) + B(\lambda, b')]
\end{aligned} \tag{1.50}$$

Note that the parity function, s , can only be ± 2 .

Let S denote the expectation value of s . Because s can only be ± 2 , it is clear that

$$|S| \leq 2 \tag{1.51}$$

This is the famous CHSH inequality we were looking for!

Critically, note that we can also write:

$$\begin{aligned}
S(a, a', b, b') &= \int s(\lambda, a, a', b, b') \rho(\lambda) d\lambda \\
&= E(a, b) - E(a, b') + E(a', b) + E(a', b')
\end{aligned} \tag{1.52}$$

Quantum violation of the CHSH inequality

Recall that, in terms of projections onto the basis states corresponding to the polarizer settings, the probability of coincidence detection of detector A and B was written in Equation 1.45 as the following:

$$P_{\phi_A\phi_B}(a, b) = |\langle\phi_{A,a}|\langle\phi_{B,b}|\psi_{EPR}\rangle|^2 \quad (1.53)$$

For starters, let $|\phi_A\rangle = |V_a\rangle$ and $|\phi_B\rangle = |V_b\rangle$, and then use equation 1.40 and 1.41, to get:

$$P_{VV}(a, b) = \frac{\cos^2(a)\cos^2(b)}{2} + \frac{\cos^2(a)\cos^2(b)}{2} + \frac{1}{4}\sin(2a)\sin(2b) = \frac{1}{2}\cos^2(b - a) \quad (1.54)$$

Similar calculation can be performed with other pairs of polarizer states. If we choose the polarizer angles to be $a = -45^\circ, a' = 0, b = -22.5^\circ$ and $b' = 22.5^\circ$, then by using equation 1.53, equation 1.48 and equation 1.50, we can get [10]

$$S^{(QM)} = 2\sqrt{2} \quad (1.55)$$

...a result which is specific to the Bell state shown in equation 1.40.

1.6.3 Experimental setup and data collection for testing Local Realism

The experimental setup for the Bell's test is shown in Figure 1.14. The alignment of the system is similar to that described in previous sections. Once again, all wave plates need to be characterized before the experiments. For procedures on initializing their rotations, please refer to Section 1.5 for detailed instructions.

Producing Bell's state

The output of the GTP is in $|H\rangle$ state. Turn the half-wave plate to 45 degrees to rotate the polarization to the state $\frac{1}{\sqrt{2}}(|H\rangle + e^{i\phi}|V\rangle)$. As a result, the output from the crystal is in the state $\frac{1}{\sqrt{2}}(|HH\rangle + e^{i\phi}|VV\rangle)$. Try to balance the counts for $|HH\rangle$ and $|VV\rangle$ and eliminate $|HV\rangle$ and $|VH\rangle$ counts by slightly rotating the half-wave plate, as preliminary initializations of the orientation may not be sufficient. Then, in order to eliminate $e^{i\phi}$, we switch the measurement basis from H and V to

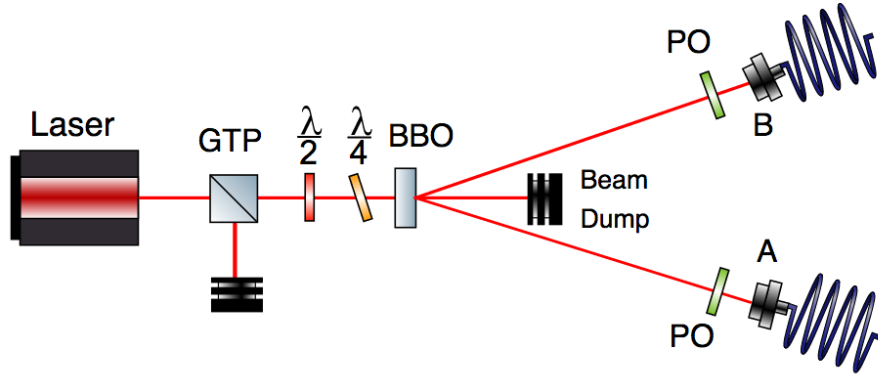


Figure 1.14: Bell's test experimental setup

+45 and -45. Try to minimize $|+45, -45\rangle$ and $|-45, +45\rangle$ counts by tilting the quarter-wave plate. Tilting the quarter-wave plate can introduce a phase factor to the state to eliminate the $e^{i\phi}$ factor. Also, try to balance $|+45, +45\rangle$ and $|-45, -45\rangle$ counts by slightly rotating the half-wave plate. After these are done, switch back to H and V basis and check to see if the previous results still holds. Perform these alignments over and over until the requirements for both the H,V basis and +45,-45 basis are met simultaneously. We now have a Bell's state, which is shown in the equation underneath.

$$|\psi_{Bell}\rangle = \frac{1}{\sqrt{2}}(|HH\rangle + |VV\rangle) \quad (1.56)$$

Measurement of the correlation function E and parity expectation S

The definitions of the correlation function E and parity expectation S provided in the previous subsection are convenient for theoretical understanding and deductions. However, to move forward, we need to re-write them in terms of quantities that are directly measurable in the lab. First, we

write the probability of a coincidence detection for detectors A and B when they are in V_a and V_b states as follows:[10]

$$P_{VV}(a, b) = \frac{N(a, b)}{N(a, b) + N(a_{\perp}, b_{\perp}) + N(a, b_{\perp}) + N(a_{\perp}, b)} \quad (1.57)$$

As a result, the the correlation function may be re-written as

$$E(a, b) = \frac{N(a, b) + N(a_{\perp}, b_{\perp}) - N(a, b_{\perp}) - N(a_{\perp}, b)}{N(a, b) + N(a_{\perp}, b_{\perp}) + N(a, b_{\perp}) + N(a_{\perp}, b)} \quad (1.58)$$

To determine the value of $E(a, b)$, four kinds of measurements must be performed. As a result, a total of 16 measurements will be carried out in the experiment, because we need four different $E(a, b)$ values to determine the parity expectation, S , which is still written as:

$$S \equiv E(a, b) - E(a, b') + E(a', b) + E(a', b') \quad (1.59)$$

1.6.4 Experimental results for testing the CHSH inequality

The results of the 16 measurements are listed in Table 1.7. The calculations required for $E(a, b)$ are shown below in 1.59.

$$\begin{aligned}
& E(a, b) : \\
& E(-45, -22.5) = \frac{N(-45, -22.5) + N(45, 67.5) - N(-45, 67.5) - N(45, -22.5)}{N_T} = 0.6856 \\
& E(a', b) : \\
& E(0, -22.5) = \frac{N(0, -22.5) + N(90, 67.5) - N(0, 67.5) - N(90, -22.5)}{N_T} = 0.6704 \\
& E(a', b') : \\
& E(0, 22.5) = \frac{N(0, 22.5) + N(90, 112.5) - N(0, 112.5) - N(90, 22.5)}{N_T} = 0.7357 \\
& E(a, b') : \\
& E(-45, 22.5) = \frac{N(-45, 22.5) + N(45, 112.5) - N(-45, 112.5) - N(45, 22.5)}{N_T} = 0.6420
\end{aligned} \quad (1.60)$$

Table 1.7: measurement results in ± 45 basis

pairs	a	b	AB
(a,b)	-45	-22.5	2980
(a,b')	-45	22.5	600
(a, b_{\perp})	-45	67.5	630
(a, b_{\perp}')	-45	112.5	3150
(a',b)	0	-22.5	2870
(a',b')	0	22.5	3025
(a', b_{\perp})	0	67.5	615
(a', b_{\perp}')	0	112.5	461
(a_{\perp} ,b)	45	-22.5	523
(a_{\perp} ,b')	45	22.5	2905
(a_{\perp} , b_{\perp})	45	67.5	3201
(a_{\perp} , b_{\perp}')	45	112.5	720
(a_{\perp}' ,b)	90	-22.5	575
(a_{\perp}' ,b')	90	22.5	496
(a_{\perp}' , b_{\perp})	90	67.5	3160
(a_{\perp}' , b_{\perp}')	90	112.5	3260

As a final result, our experimental data yields $S = E(a, b) - E(a, b') + E(a', b) + E(a', b') = 2.7319$, close to the value predicted by quantum mechanics, $2\sqrt{2}$, and much different from the EPR limit (the violation of the CHSH inequality, $|S| \leq 2$, is clear).

1.6.5 Error analysis for our Parity Function result

The uncertainty of the quantity S is found by adding, in quadrature, the contributions due to limited counting statistics associated with each independent measurement:

$$\sigma_s = \sqrt{\sum_{i=1}^{16} (\sigma_{N_i} \frac{\partial S}{\partial N_i})^2} = \sqrt{\sum_{i=1}^{16} N_i (\frac{\partial S}{\partial N_i})^2}. \quad (1.61)$$

As

$$\frac{\partial S}{\partial N_i} = \frac{\partial E(a, b)}{\partial N_i} - \frac{\partial E(a, b')}{\partial N_i} + \frac{\partial E(a', b)}{\partial N_i} + \frac{\partial E(a', b')}{\partial N_i} \quad (1.62)$$

The data listed in the result table yields:

$$\sigma_S = 0.023 \quad (1.63)$$

So, our final, experimental result for our measured S value is 2.732 ± 0.023 . Thus, EPR's local hidden variable theory, which requires $|S| \leq 2$, is *incompatible* with the observed quantum phenomena, as my data demonstrates a $31\sigma_S$ violation of the CHSH inequality. These experimental results lead us to conclude, as others have before us, that the photons do not have a definite measurement basis before measurements; instead, they are in true superposition states.

CHAPTER 2

EXPERIMENTAL ANALYSIS OF THE ORBITAL ANGULAR MOMENTUM OF LIGHT

2.1 Topics regarding the Angular Momentum of Light

Light’s orbital angular momentum (OAM), and spin angular momentum (SAM), either used separately or together, offer revolutionary opportunities. I hope that pun made you chuckle, but it is also true! As noted in Section 1.5.1, the higher-dimensional Hilbert Space associated with OAM allows more information to be encoded, in comparison to SAM. Indeed, record-setting data transmission rates have been achieved by encoding information into light’s OAM, limited, in the case of free-space transmission, only by the system *étendue*, which caps the accessible dimensionality of the Hilbert Space to a finite number, D . On the other hand, in Section 1.5.1, our experiment on quantum state measurement allowed us to extract a measurement of the SAM of the photons produced in our SPDC setup. In that section, we also made note of the challenges associated with reading out information encoded in higher-dimensional quantum states, explicitly pointing out that $2D - 1$ distinct kinds of measurements would be required, *if* we restrict ourselves, as was done in that section, to the “20 Questions” strategies required for the complete set of information required to uniquely specify the quantum state.

In the early portions of this chapter, a (slightly less complete version of) state measurement is massively *parallelized* through the use of transformation optics provided to Illinois Wesleyan University by Martin Lavery and Miles Padgett of Glasgow University, which allow for ultra-fast readout of OAM information. We are interested in investigating the *robustness* of this method, and the degree to which aberration correction methods can be of use. Section 2.2 provides a theoretical background on OAM, and ends by comparing the results of simulations to the results we have actually obtained in the lab. – In order to understand the experimental steps required to achieve these results, Section 2.3 takes a step back, to present our basic methods for generation of OAM modes, while in Section 2.4 we discuss both the need for further optimization and the methods we have used for aberration correction. The OAM portion of the thesis is completed by

Section 2.5, which introduces the use of Martin Lavery’s transformation optics for rapid readout of a Laguerre-Gaussian beam, a beam mode that carries orbital angular momentum.

This study of beams containing OAM *complements* our applications of SAM in (holographic) optical traps, where readout of optically induced torques is essential to a host of applications. For such research we have fabricated smaller-than-normal birefringent vaterite (CaCO_3) microspheres. So, in Section 1.6 we describe our synthesis of vaterite crystals. In the final section of this chapter, Section 1.7, we describe an immediate application of the mechanical transfer of angular momentum to our vaterite samples (for *contact-free* mechanotransduction of biological cells), and also point towards our most aspirational dreams for their use.

For this work, the transformation optics and the corresponding alignment procedures were provided by Dr. Martin Lavery. The alignment of the setup for generating LG beams is something that I have done independently at IWU, with feedback from Dr. Lavery. I also relied heavily upon Dr. Lavery’s written works for the theoretical background, and so this thesis owes a heavy debt to those works. The IDL program for generating Laguerre-Gaussian beam was provided by Dr. Gabe Spalding and his students in IWU, and are provided in this chapter as a resource to future students. I have improved the core program by adding a circular aperture to the phase profile, using code which is also provided in this chapter. In addition, I added in the use of the adaptive-additive method for aberration correction, which I have not found applied to this kind of system in any of the literature I have encountered. In section 2.6, we are trying to study transference of mechanical angular momentum, from light, to vaterite crystals that I have synthesized in IWU. The recipe for vaterite synthesis that I used was provided by Yoshi Arita of St Andrews University, though by systematic variation of parameters I tried to find my own optimization.

2.2 The Orbital Angular Momentum of light

2.2.1 Introduction to OAM

The angular momentum of light consists of two parts: (a) spin angular momentum, associated with the (intrinsic) polarization state of the photons, and (b) the orbital angular momentum, associated with helicity of a wavefront, as highlighted by the groundbreaking work of Les Allen *et al.* This year marks the 25th anniversary of that landmark paper in *Physical Review A*, which led to widespread recognition of the orbital angular momentum content of Laguerre-Gaussian (LG) modes.[1]

The pace of innovation based upon the use of LG beams only seems to have increased since then. One of the more widely publicized applications is a method to circumvent (without violating) the (apparent) limitations of the uncertainty principle for super-resolution imaging, via “Stimulated Emission Depletion” (STED) microscopy, which earned a 2014 Nobel Prize.[16] However, most applications have nothing to do with engineering the selection rules for atomic transitions. At the moment, a dominant area of interest has to do with increasing the information density for communications. Just eight months ago, IEEE (“The world’s largest technical professional organization dedicated to advancing technology for the benefit of humanity”) posted the following *Tech Alert*:

Twisted Light Could Dramatically Boost Data Rates

We’re running out of available spectrum for transmitting signals. But we may soon have a way to cut the same pie into a seemingly endless number of slices. A property of light called orbital angular momentum (OAM) allows overlapping beams with different values to behave as if they can’t “see” each other. Each beam is distinct, and none are intrinsically capable of interacting with the others. So multiple data streams can be sent using a single frequency – all without cross talk.[27]

2.2.2 Beyond the fundamental Gaussian mode

In this section I will give a theoretical introduction to the Laguerre-Gaussian laser beam modes and their associated “topological charge,” and will then briefly introduce a setup for generating LG beams in our lab. The LG modes form a basis set of independent solutions to the paraxial approximation of the Maxwell wave equation in cylindrical coordinates. While the study of laser modes has been an important subject since the invention of laser, introductory texts invariably concentrate instead upon the Hermite-Gaussian modes, which constitute an alternative basis set appropriate to Cartesian coordinates [24]. The following mathematical description largely follows what is provided in the paper “Gaussian, Hermite-Gaussian, and Laguerre-Gaussian beams: A primer” by Francesco Pampaloni and Joerg Enderlein, and the book, “Photonics” by Vittorio Degiorgio and Ilaria Cristiani.

For monochromatic waves, Maxwell’s wave equation for the electric field may be written in “static” form (eliminating explicit mention of any time dependence), as shown in equation (2.1).

[24]

$$\left[\frac{\partial^2}{\partial x^2} + \frac{\partial^2}{\partial y^2} + \frac{\partial^2}{\partial z^2} + k^2 \right] E(x, y, z) = 0 \quad (2.1)$$

As our interest is in propagating beams, we can, without loss of generality, define the z -axis to be the direction of propagation (*i.e.*, the optic axis). A general solution to this equation may then be written, via Fourier synthesis over spatial frequencies, as a superposition of plane waves with different amplitudes traveling at different angles with respect to the optic axis, as shown below:

[24]

$$E = \int \int \frac{dk_x dk_y}{(2\pi)^2} A(k_x, k_y) e^{ik_x x + ik_y y + i(\sqrt{k^2 - k_x^2 - k_y^2})z} \quad (2.2)$$

In the paraxial approximation, we assume that the k vector components along the x and y directions contribute only a small part to the total k vector (*i.e.* $k_{x,y} < k$). Within this approximation, the binomial approximation allows us to re-write equation 2.2 as: [24]

$$E = \int \int_{k_{x,y} < k} \frac{dk_x dk_y}{(2\pi)^2} A(k_x, k_y) e^{ik_x x + ik_y y + ikz - i\left(\frac{k_x^2 + k_y^2}{2k}\right)z} \quad (2.3)$$

Furthermore, the paraxial approximation implies a windowing of the transverse spatial frequencies. The standard way to enforce this is to assume that $\frac{\partial A(k_x, k_y)}{\partial k_x}$ and $k_x A(k_x, k_y)$ only differ by a

constant factor, which we can call w_0 , and that the same condition applies to the y direction. As a result, the amplitude term in the Fourier synthesis may be written as a Gaussian:

$$A(k_x, k_y) \propto e^{-\frac{w_0^2}{4}(k_x^2 + k_y^2)} \quad (2.4)$$

This form is particularly useful because the Fourier Transform of a Gaussian is itself a Gaussian. So, *e.g.*, given that the action of an optical lens is to output, at its front focal plane, the Fourier Transform of the input provided at its back focal plane, this implies that if the input beam is Gaussian, then the output will be Gaussian as well. This fundamental laser mode can be expressed in terms of the intensity of the electric field, in equation 2.5.

$$E = \int \int_{k_x, y < k} \frac{dk_x dk_y}{(2\pi)^2} e^{ik_x x + ik_y y + ikz - i\left(\frac{k_x^2 + k_y^2}{2k}\right)z - \frac{w_0^2}{4}(k_x^2 + k_y^2)} \quad (2.5)$$

Solving this integral requires the following mathematical rule:[24]

$$\int_{-\infty}^{+\infty} \frac{dx}{2\pi} e^{iax - \frac{b^2}{2}x^2} = \frac{1}{\sqrt{2\pi b^2}} e^{-\frac{a^2}{2b^2}} \quad (2.6)$$

Applying this rule to the integral in equation 2.5, we can get equation 2.6. [9]

$$E_0 = \frac{1}{w_0^2 + 2iz/k} e^{ikz - \frac{x^2 + y^2}{w_0^2 + 2iz/k}} \quad (2.7)$$

Now we introduce several physical quantities to further simplify the expression. First, the Rayleigh length (or ‘‘Rayleigh range’’), which is the distance from the focus of a beam to the place where the beam area doubles. The expression for Rayleigh length z_R is shown below.[24] [9]

$$z_R = \frac{kw_0^2}{2} = \frac{\pi w_0^2}{\lambda} \quad (2.8)$$

(Note that this implies that the smaller the beam waist, w_0 , the more rapidly the beam spreads or, conversely, that the rules of Fourier synthesis mandate that construction of a small spot size requires rays converging from high angles). Further compaction of our expressions are possible if we highlight the cylindrical symmetry of the Gaussian via use of a transverse radial coordinate, $\rho^2 = x^2 + y^2$, and introduce a dimensionless propagation coordinate, ζ , where [9]

$$\zeta = \frac{z}{z_R} \quad (2.9)$$

After some algebra, the expression in 2.7 is transformed into:

$$E_0 = \frac{1}{w_0 \sqrt{1 + \zeta^2}} e^{ikz - \frac{1 - i\zeta}{w_0^2(1 + \zeta^2)} \rho^2 - i \arctan(\zeta)} \quad (2.10)$$

The field, E_0 , described in 2.10 is called the fundamental Gaussian mode, which denotes both the fact that the beam it describes does have a Gaussian intensity profile along the z axis and the fact that there higher-order spatial modes are also possible, as described in the next subsection.[24]

Again, the above derivation follows the presentation in the paper “Gaussian, Hermite-Gaussian, and Laguerre-Gaussian beams: A primer” by Francesco Pampaloni and Joerg Enderlein, and the book, “Photonics” by Vittorio Degiorgio and Ilaria Cristiani. Interested readers may find these resources helpful for further understanding and discussions.

2.2.3 Laguerre-Gaussian modes

The Laguerre-Gaussian modes are an orthonormal family of solutions to the paraxial wave equation. They all have rotational symmetry around the optical axis. A key step in deriving the expression for LG beams comes from noting the periodicity of the azimuthal angle, ϕ , which results in the following constraint: [5] [24]

$$k_x \pm ik_y = \sqrt{k_x^2 + k_y^2} e^{i\phi} \quad (2.11)$$

Armed with this knowledge, we test, by substitution into equation 2.3, a trial solution where the amplitude $A(x, y)$ is proportional to $(k_x + ik_y)^m (k_x - ik_y)^{m+n}$, wher m and n are integer indices: [24]

$$E_{m,n}^L \propto \int \int_{k_x, y < k} \frac{dk_x dk_y}{(2\pi)^2} (k_x + ik_y)^m (k_x - ik_y)^{m+n} e^{ik_x x + ik_y y + ikz - \frac{w_0^2}{4}(1+i\zeta)(k_x^2 + k_y^2)} \quad (2.12)$$

To simplify this expression, we introduce [24]

$$S(k_x, k_y, x, y, z) \equiv ik_x x + ik_y y + ikz - \frac{w_0^2}{4}(1+i\zeta)(k_x^2 + k_y^2) \quad (2.13)$$

and note that [24]

$$ik_x e^S = \frac{\partial e^S}{\partial x} \quad (2.14)$$

As a result, equation 2.12 can be written in a compact form that relates this field to the fundamental Gaussian mode:[24]

$$E_{m,n}^L \propto (\partial_x + i\partial_y)^m (\partial_x - i\partial_y)^{m+n} E_0 \quad (2.15)$$

Further simplifications are possible via the following expressions. [24]

$$\begin{aligned}
\omega &\equiv x + iy \\
\bar{\omega} &\equiv x - iy \\
\partial_{\bar{\omega}} &= \frac{1}{2}(\partial_x + i\partial_y) \\
\partial_{\omega} &= \frac{1}{2}(\partial_x - i\partial_y) \\
\rho^2 &= \omega\bar{\omega}
\end{aligned} \tag{2.16}$$

Equation 2.15 then simplifies into the following form:

$$E_{m,n}^L \propto \partial_{\bar{\omega}}^m \partial_{\omega}^{m+n} E_0 \tag{2.17}$$

At this point, we need to recall a standard function which arises in multiple contexts, namely, the Laguerre function: [24]

$$L_m^n(r) \equiv \frac{e^r r^{-n}}{m!} \frac{d^m}{dr^m} (e^{-r} r^{m+n}) \tag{2.18}$$

Thus armed, it is quick work to demonstrate that the differentiation in equation 2.17 has solutions that contain the Laguerre function as well as the fundamental Gaussian mode: [24]

$$\partial_{\bar{\omega}}^m \partial_{\omega}^{m+n} E_0 = (-\omega)^{-m-n} m! \left[\frac{\omega\bar{\omega}}{w_0^2(1+i\zeta)} \right]^n \left[\frac{\omega}{w_0^2(1+i\zeta)} \right]^m L_m^n \left[\frac{\omega\bar{\omega}}{w_0^2(1+i\zeta)} \right] E_0 \tag{2.19}$$

Thus, our trial solutions are valid, and may now be written in a general form. [24]

$$\psi_{\ell,p}(r, \phi) = C_{\ell,p} \left(\frac{\sqrt{2}r}{\omega} \right)^{\frac{|\ell|}{2}} L_p^{|\ell|} \left(\frac{2r^2}{\omega^2} \right) \times e^{-\frac{r^2}{\omega^2}} e^{i\ell\phi} \tag{2.20}$$

This set of solutions are termed Laguerre-Gaussian modes, as the Laguerre polynomial appears in the equation, now denoted by $L_p^{|\ell|} \left(\frac{2r^2}{\omega^2} \right)$, where our integer indices are now ℓ and p , alongside a Gaussian profile which ensures that these paraxial solutions decays we move off of the optic axis. The final term, involving the azimuthal angle, was mandated by the periodic nature of that angle. The physical origin of the OAM content of LG beams lies within this phase term, which gives rise to a helicity of the wavefront for any solution where ℓ is non-zero, as shown in Figure 2.1.

The integer index ℓ is commonly referred to as the ‘‘topological charge’’ of the beam, as it determines the number of intertwined helices in the beam. In working with analogous acoustic beams, Prof.

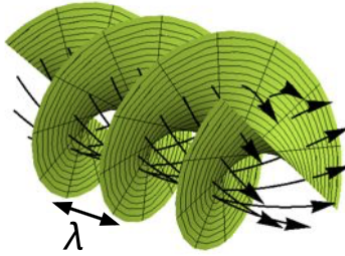


Figure 2.1: Laguerre-Gaussian beam with helical wavefront. This picture is taken from page 26 of Martin Lavery’s thesis, “Measurement of Light’s Angular Momentum.” [21]

Spalding and his co-authors provided the first direct, mechanical evidence of the OAM-to-energy ratio of LG beams: [11]

$$\frac{\langle L_z \rangle}{\langle U \rangle} = \frac{1}{\omega_B} \ell \quad (2.21)$$

In other words, the OAM content of the beam is simply proportional to the topological charge.

It is important to reiterate that the allowed values of ℓ are theoretically unbounded. Thus, whereas there are only two kinds of spin angular momentum associated with photons, associated with left or right circularly polarization, no such constraint applies to the orbital angular momentum of light: there is no theoretical limit to the number of spirals in a wavelength of the beam, providing promise for greatly increasing the information capacity for optical communication (which is the backbone of the internet). Note that the above derivation for the mathematical form of the LG beam largely follows the paper “Gaussian, Hermite-Gaussian, and Laguerre-Gaussian beams: A primer” by Francesco Pampaloni and Joerg Enderlein,

2.2.4 Experimental generation of Laguerre-Gaussian beams

Here in Dr. Spalding’s optics lab in Illinois Wesleyan University, we are using a laser source whose output is a very good approximation to the fundamental Gaussian mode. Figure 2.2 is a rather simplified schematic representing how this beam is processed, most significantly by a Spatial Light Modulator (SLM), so as to generate Laguerre-Gaussian beams.

In the setup, we use a Coherent Model Verdi-5 laser operating at 532 nm as our laser source. While the maximum power available from this source is 5.5 watts, we typically operate near the lasing threshold, which requires a minimum power of 10 mW. Further reduction of the output is achieved via use of the half-wave plate and the polarizing beam splitter, which in combination allow us to continuously vary the power in the transmitted beam. In order to increase the efficiency of the Spatial Light Modulator, we must expand the area of the laser beam so the active area of the SLM is illuminated completely and (more or less) uniformly. The beam expander consists of a pair of plano-convex lenses separated by the sum of their focal lengths. This Keplerian telescope expands the laser beam by a factor equal to the ratio of the focal lengths of the two lenses. The absolute values of those focal lengths is not critical, although as the focal lengths become very long the system becomes more susceptible to convection currents in the room as well as any limitations associated with the (quite good) intrinsic pointing stability of the Verdi-5 laser. At the other extreme, if the focal lengths become quite short, errors in the relative placement of the two lenses may require the use of a shear-plate collimator to ensure that the output is neither converging nor diverging. In order to reduce aberrations, whenever the beam is passing through lenses we take care to align the beam parallel to the optical table and along a line of holes, as was described in Section 1.3.2 (“Walking the beam”). Those steering mirrors have been omitted from the schematic shown here, for simplicity.

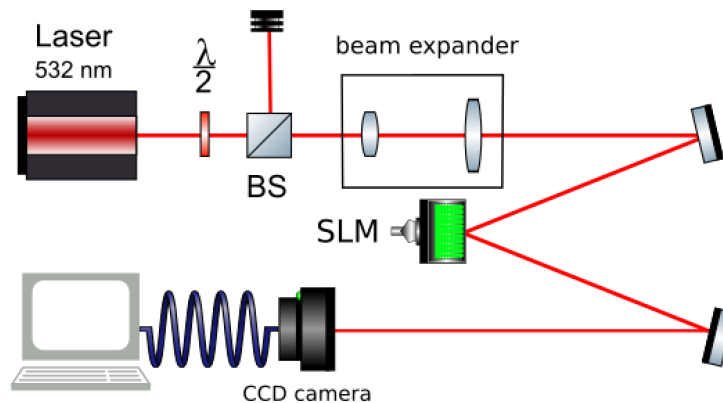


Figure 2.2: Experimental setup for generating Laguerre-Gaussian beams

We use an optically addressed Hamamatsu SLM with 768 x 768 pixels and 256 linear phase levels, to perform phase-only modulation to the incoming beam. The phase profile imparted by the SLM is programmably controllable, as described below. The modified beam reflected off of the SLM and is then detected at a CMOS camera.

We have made use of a *LabVIEW* program provided by Dr. Martin Lavery to simulate the LG beams with different topological charges. [19] Figure 2.3 compares our simulated target intensity profiles to those of the beams we were actually able to generate via our programs described in Section 2.3, subsequent to the aberration corrections described in Section 2.4. For reference, the degree of agreement, while not perfect, was cause for considerable celebration in our lab.

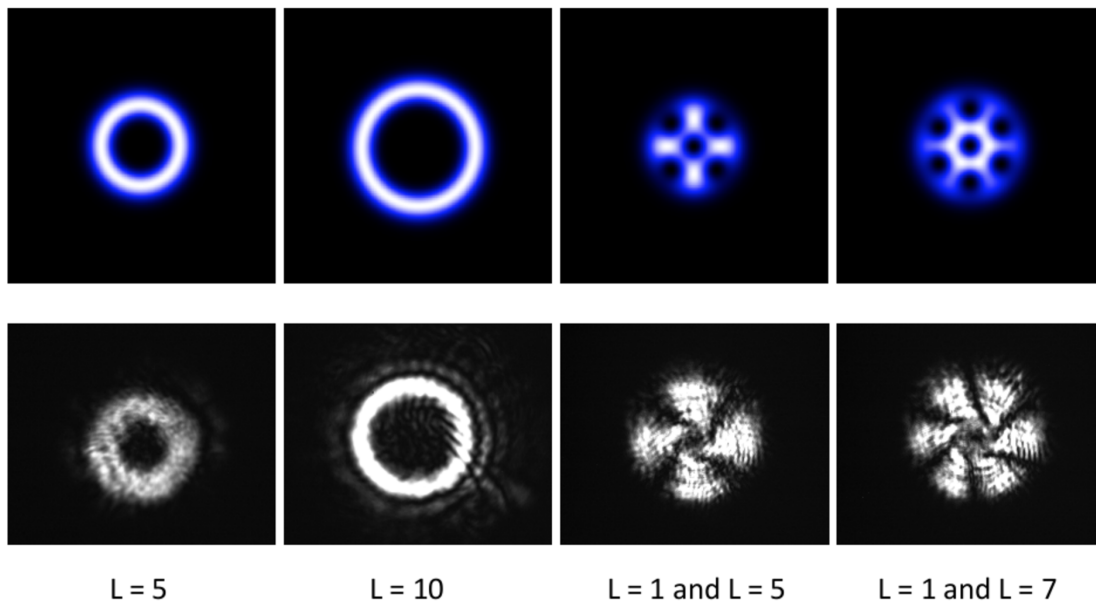


Figure 2.3: Intensity profiles for LG beams generated using Lavery’s simulation (top), and results actually produced in our experiment (bottom)

In the first two columns of Figure 2.3, each of which corresponds to a single mode, note that the result is a “donut beam.” That fact that there is a null along the optic axis is a consequence of the azimuthal phase profile, $e^{il\phi}$, where ϕ is, again, the angle of rotation about the optic axis. This then implies that a multiple of 2π phase is accumulated in any closed path integral containing the optic axis. Thus, the optic axis itself corresponds to a phase singularity. The language of Fourier

Synthesis provides a physical understanding of the result: the fact that rays with all possible phases meet in the middle results in perfect destructive interference. Because of the high degree of symmetry involved, an LG beam with nonzero ℓ should provide a particularly “good dark” on axis (which for some applications, such as cold atom trapping, is a truly essential feature). As we move to higher ℓ -values, the phase gradient becomes steeper and so, as a consequence, the distance one must move off axis before reaching a point where constructive interference results is increased. Hence, in comparing the first two columns of Figure 2.3, the larger ℓ is, the larger the radius of the donut beam generated.

In the final two columns of Figure 2.3, note that the intensity profile reflects interference between two distinct modes, each characterized by their own value of ℓ . The resulting number of azimuthal maxima in the intensity is given by the difference in the ℓ -values of these modes. More importantly, the fact that there is interference does not, in any way, negate the claim that these are independent modes, which hold the potential to transmit information without crosstalk: the beam reaching the camera remains decomposable into its constituent modes (*e.g.*, via the transformation optics described in Section 2.5).

Before we move onto our discussion of transformation optics, however, there are a great many details to discuss regarding the experimental work required to achieve the quality of outputs illustrated in Figure 2.3 above. The following section begins that discussion by considering, in greater detail, the phase profiles to be programmed into the SLM.

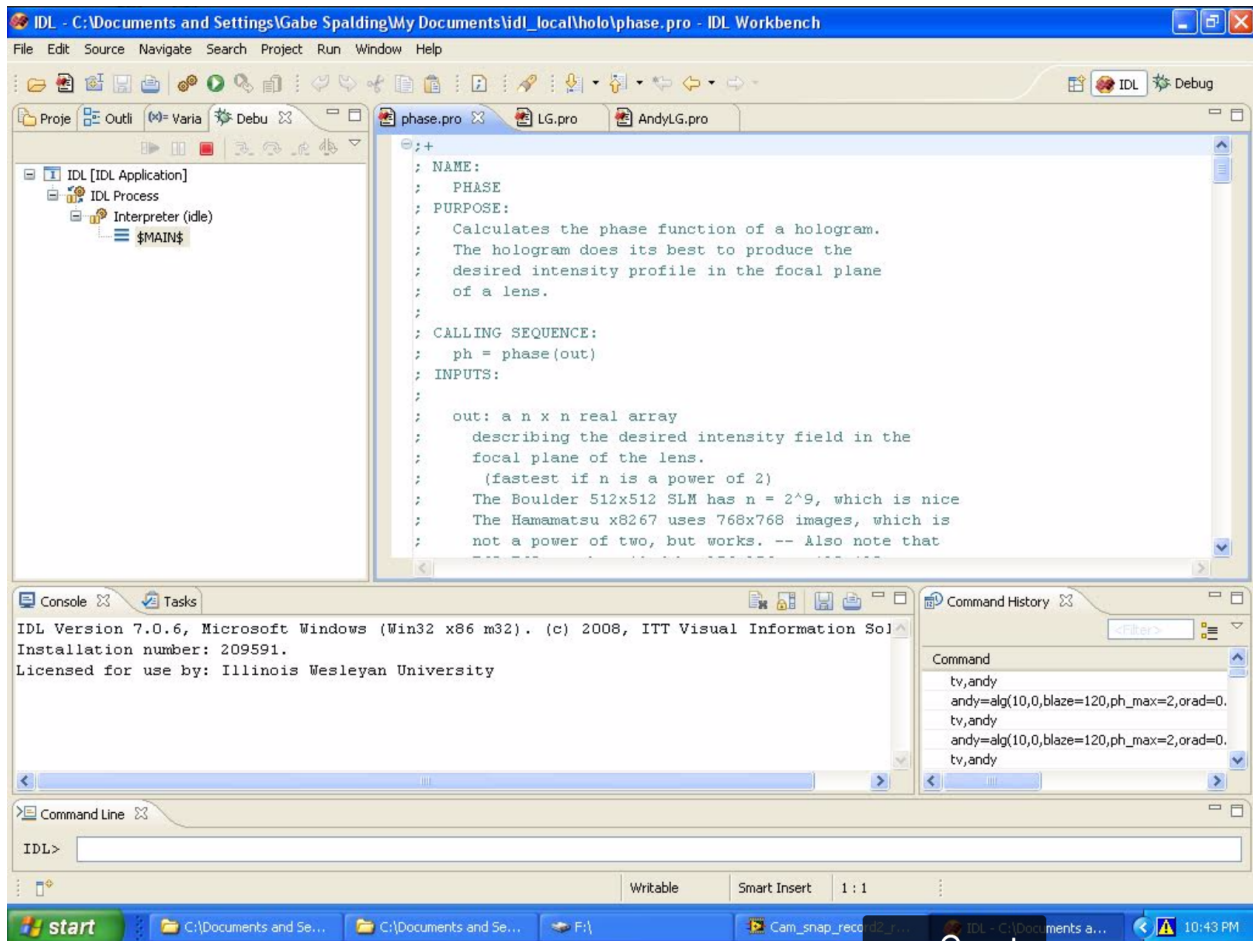


Figure 2.4: IDL interface, default view

2.3 Programming a Spatial Light Modulator: a primer

2.3.1 A very brief introduction to IDL programming

Figure 2.4 introduces our programming language of choice, *IDL*, which is short for *Interactive Data Language*. It is an array-oriented data analysis and visualization environment, available for Windows, MacOS and UNIX, and there is also an open-source version, *GDL*, which is capable of running all of the code described below.[15] Our libraries can be used for particle tracking image

analysis (useful for our work involving optical traps) and, most critically for this chapter, programming tailor-made phase profiles onto our Spatial Light Modulator. In principle, any programming language could be used for these purposes. However, libraries included in this thesis, all written in IDL, make it convenient to generate LG beams and to perform aberration correction.

In Figure 2.4, at upper left are tabs for the file explorer, the variable table, and the debugging interface. The upper right has the compiled programs shown in an editor, from which programs can be directly edited and re-compiled. The lower right shows the command history. If there is a very long and complicated command you have used before, you can search for it in the command history and double-click it. On the lower left part we have the console panel, which shows the status of recent commands input into IDL, or the progress of the program compiling or running. At last, at the very bottom of the page we have the command line, which enable us to use IDL *interactively*. That is, unlike C++ and Java, IDL operates as an *interpreter* (as opposed to a *compiler*), which means that each statement we enter into the command line (*e.g.*, to generate an LG mode) is immediately translated into action. At the same time, we do have the ability to create (and compile) scripts which define the tailored functions and procedures specific to our work. Those form the libraries included in this thesis.

2.3.2 Creating a window for display

The computer cannot recognize the difference between the SLM and a standard monitor of resolution 1024x768 pixels (even though only the central 768x768 pixels of that “virtual monitor” are active elements on the SLM itself). In practice, we program the SLM as if we were attempting to display 8-bit gray scale images on a second monitor. The gray scale levels of 0 – 255 translate, approximately linearly, into the 0 – 2π phase shifts applied by the SLM. Therefore, as a prequel to encoding any phase profile on the SLM, we need to tell the computer to open up an appropriately located window on (what it believes is) the second display monitor. The code for generating the window is shown below.

$$window, 0, xsize = 768, ysize = 768, xpos = 1151, ypos = -30 \quad (2.22)$$

Type this into the command line, and then a window will show up on the second screen in the right location. Because keywords in IDL may always be truncated to the shortest unique entry, the same action results from entering:

$$\text{window}, 0, xs = 768, ys = 768, xp = 1151, yp = -30 \quad (2.23)$$

As to the particular position coordinates used, the computer believes that we are using dual displays, arranged side by side. In the computer settings we adjust the resolution of both displays to 1024x768 pixels. To confirm that these window coordinates were appropriate, we unplug the SLM and instead connected, temporarily, a real second monitor. In this way, we found that the coordinates (1151, -30), will center the window while also moving with window header bar off screen.

2.3.3 Generating LG beams using LG.pro

A spiral phase profile may be added to the SLM by calling the function contained within the script LG.pro, written by Dr. Gabe Spalding. To inspect the contents of the script, type at the command line “.compile LG.pro” and hit enter, and this program will show up in the editor. In order to actually apply the spiral phase profile to the window created above, we first load the phase profile into an array, by entering, at the command line, $LGmode = lg(\ell, p)$, where $LGmode$ can be substituted with whatever name you wish to assign to the array returned by the function lg . There are several optional keywords that can be applied, as noted in the documentation included with in the LG.pro code, but the only required arguments of the function lg are ℓ , which is the topological charge of the beam, and p , which is the radial mode index, which determines the number of radial nodes in the resulting intensity distribution. For all of the beams described in this thesis, we kept p equal to zero (though non-zero p modes have been used in our lab to synthesize “bottle beams”).

In addition to the spiral phase required by the $e^{i\ell\phi}$ term associated with OAM, this function adds (*modulo* 2π) a linear phase profile. This added “blazing” shifts the desired Laguerre-Gaussian mode away from the zeroth-order un-diffracted beam, and as a side benefit separates any components associated with different ℓ values into the different diffraction orders, allowing us to select the one we desire via spatial filtering (typically done in the Fourier plane of the SLM). The blazing parameters

may be adjusted via the optional keyword “*blaze*,” which sets the number of 2π blazings across the field, as follows:

$$mode = lg(10, 0, blaze = 100) \quad (2.24)$$

where higher values of *blaze* increase the linear phase gradient. For example, Figures 2.5 and 2.6 demonstrate the difference in the separation of the diffracted orders when the blazing changes from 120 to 150.

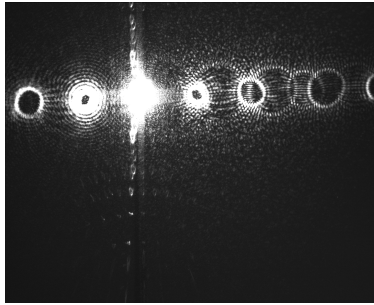


Figure 2.5: Multi-order LG beams returned by the *lg* function with $\ell = 10$ and *blaze* = 120 (the default value)

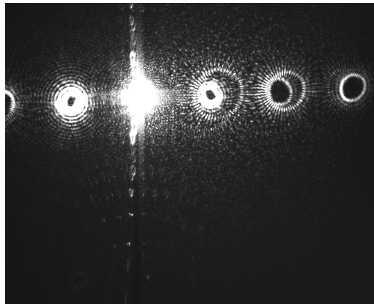


Figure 2.6: Multi-order LG beams returned by the *lg* function with $\ell = 10$ and *blaze* = 150. Note that the separations between components associated with different ℓ values is increased with this value of *blaze*, compared to the smaller value associated with the previous figure.

While our experiments do make use of the *blaze* keyword, it is instructional to remove the blazing, as follows:

$$mode = lg(l, g, /noblaze), \quad (2.25)$$

This yields, for $\ell = 1$, and for $\ell = 5$, the phase profiles shown below in Figures 2.7 and 2.8, respectively.

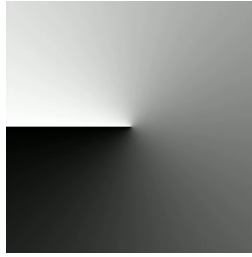


Figure 2.7: Phase profile with no blazing and $\ell = 1$. Assuming appropriate calibration, a grey scale value of 0 nominally corresponds to zero phase shift, while a grey scale value of 255 roughly yields a phase shift of 2π . Thus, because of the equivalency of 0 and 2π phase for a cyclic process, the horizontal line in the phase profile is not a discontinuity. On the other hand, the point in the center, where all phases meet, is a singularity in phase.

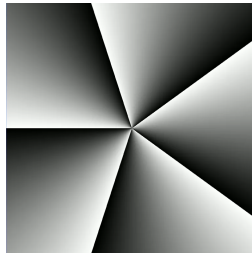


Figure 2.8: Phase profile for no blazing and $\ell = 5$. The presence of five lines indicates the multiple of 2π phase change accumulated in any closed path integral containing the phase singularity at the center.

It is also instructional to examine the phase profile returned when we leave in a blazing, but apply no topological charge to the phase profile. The resulting phase profile, which is the diffractive optic equivalent of a prism, would, ideally, simply translate the beam away from the un-diffracted, zero-th order spot. For $blaze = 10$, the phase profile returned is shown in Figure 2.9. Contrast this with the result when a linear phase gradient, of the sort shown in Figure 2.9, is added, *modulo* 2π , with a spiral phase profile, which yields a characteristic forked pattern, where the number of “topological edge dislocations” introduced into the blazing is equivalent to the topological charge. For example, Figures 2.10 and 2.11 show the results of adding $blaze = 10$ to the phase profiles for $\ell = 1$ and $\ell = 5$, respectively.

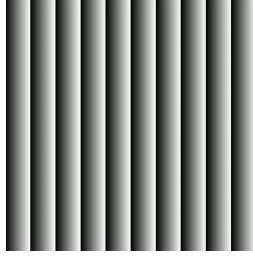


Figure 2.9: A phase profile with $\ell = 0$ and $blaze = 10$ lacks any phase singularity.

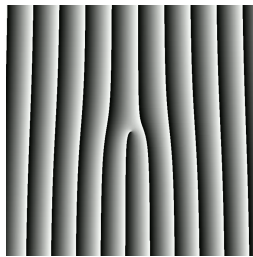


Figure 2.10: Phase profile combining $\ell = 1$ and $blaze = 10$. The topological charge is apparent from the single topological edge dislocation emanating from the phase singularity in the center.

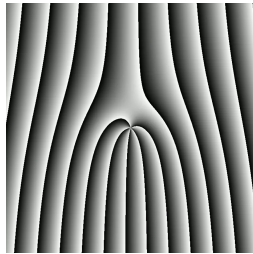


Figure 2.11: Phase profile for $\ell = 5$ and $blaze = 10$. Careful inspection will reveal five topological edge dislocations emanating from the phase singularity.

2.3.4 The original code for LG.pro

```
1 ;+
2 ; NAME:
3 ;   LG
4 ;
5 ; PURPOSE:
6 ;   For creating an approximated, generalized (p not necessarily zero!)
7 ;   Laguerre-Gaussian mode out of a fundamental Gaussian input beam --
8 ;   and, if desired, to shift it away from the undiffracted central
9 ;   spot of the diffractive optic
10 ;
11 ; CATEGORY:
12 ;   Hologram/DOE Generator
13 ;
14 ; CALLING SEQUENCE:
15 ;   LGmode = lg(l, p)
16 ;
17 ; INPUTS:
18 ;   l: the multiple of 2pi associated with traversal about the center
19 ;   ('azimuthal number')
20 ;
21 ;   p: the radial index for the LG mode ('radial number')
22 ;
23 ; OPTIONAL INPUTS (KEYWORD PARAMETERS):
24 ;   blaze: the number of 2pi blazings across the field
25 ;   (we've been using 120)
26 ;   -- this is effectively adding a prism to refract the beam
27 ;   away from the central spot
28 ;   -- increasing 'blaze' is like increasing the angle of the exit
29 ;   face of the prism
30 ;
31 ;   noblaze: if no blazing is desired, this keyword must be set
32 ;   (see RESTRICTIONS below)
33 ;
34 ;   rad: the radius of a circular discontinuity
35 ;   (must fit on the DOE for the beam to sample)
36 ;
37 ;   nbit: provides 2^nbit levels of phase,
38 ;   default setting is 8 (for Hamamatsu x8267 SLM)
39 ;
40 ;   npix: number of pixels on a side,
41 ;   default setting is 768 (for Hamamatsu x8267 SLM)
42 ;
43 ; OUTPUTS:
44 ;   LGmode: a npix x npix real array giving a spiral phase plate,
45 ;   with radial phase shifts added
46 ;
47 ; SIDE EFFECTS:
48 ;   For l = 0, p = 0, this creates a blazed diffraction grating
49 ;   (the DOE equivalent of a prism)
50 ;
```

```

51 ; REQUIRES:
52 ;   Calibration of the phase levels of the SLM used, for the desired
53 ;   operating conditions, in terms of the 'greyscale' levels used here.
54 ;   An appropriate look-up table (LUT) would allow the images generated
55 ;   by this program to be used directly by the SLM.
56 ;
57 ; RESTRICTIONS:
58 ;   The program does not directly recognize BLAZE = 0.
59 ;   This is a consequence of the way the keyword_set function works.
60 ;   The workaround is to add the argument /NOBLAZE whenever no
61 ;   blazing is desired. (Note that '/no' will work as an abbreviation
62 ;   for '/NOBLAZE,' since in general a slash preceding a keyword sets
63 ;   its value to one, and keywords can be abbreviated to their shortest
64 ;   unique length. For example, a keyword called XSTYLE could be
65 ;   abbreviated to XST)
66 ;
67 ;   Extremely large phase gradients will be 'aliased' due to the
68 ;   discretization of the SLM (the number of phase levels and the size
69 ;   of the pixels).
70 ;
71 ; MODIFICATION HISTORY:
72 ;   Created by Gabe Spalding
73 ;   October, 2002
74 ;-
75
76 FUNCTION lg,l, p, blaze=blaze, noblaze=noblaze, rad=rad, nbit=nbit, $
77     npix=npix
78
79 IF NOT keyword_set(blaze) THEN blaze = 120
80 IF keyword_set(noblaze) THEN blaze = 0
81 IF NOT keyword_set(rad) THEN rad = 100
82 IF NOT keyword_set(nbit) THEN nbit = 8
83 IF NOT keyword_set(npix) THEN npix = 768
84
85 LGmode=fltarr(npix,npix)
86 offset = long(0.5 * npix)
87 FOR i=0,npix-1 DO BEGIN
88     FOR j=0,npix-1 DO BEGIN
89
90         ; First, create a phase blazing to shift everything away
91         ; from the undiffracted spot:
92         ; (Whenever no blazing is desired, add the argument /noblaze.)
93         LGmode(i,j) = i * (2*!pi) * blaze/(npix-1)
94
95         ; Next, convert this refracted spot to a p=0 LG mod
96         ; by creating a spirial phase plate:
97         ; the azimuthal angle is given by
98         theta = ATAN(j-offset, i-offset)+!pi
99         ; A term containing the azimuthal angle multiplied by
100        ; the azimuthal number creates the spiral phase plate:
101        LGmode(i,j) = LGmode(i,j) + l * theta
102
103        ; Now, find how far the present pixel is from the center
104        ; of the diffractive optical element (DOE)
105        rho = SQRT((i-offset)^2.0 + (j-offset)^2.0)

```

```

106
107     ; Use this radius as a criteria for adding further phase shifts that
108     ; depend upon the radial number:
109 IF p GT 0 THEN BEGIN
110     FOR pindex = 1, p DO BEGIN
111         ; For non-zero radial number, the DOE will contain p circles ,
112         ; with sizes given by:
113         cirsize = pindex*rad
114         ; Beyond each of those circles , we add a pi phase shift ,
115         IF rho GE cirsize THEN LGmode(i,j) = (LGmode(i,j) + !pi)
116     ENDFOR
117 ENDIF
118
119 ENDFOR
120 ENDFOR
121
122 modulo = 2*!pi
123 LGmode = LGmode - (modulo * long(LGMode/modulo))
124
125     ; Finally , scale everything from units of phase to units of
126     ; 'image level'
127 LGmode = LGmode*((2^nbit-1)/(2*!pi))
128     ; The extra parentheses above improve efficiency :
129     ; otherwise the precedence of multiplication over division would mean
130     ; that the array would be operated on twice .
131
132 return ,LGmode
133 END

```

2.3.5 Enforcing symmetry upon the phase profile

So far, the phase profiles shown have made use of the full active area of the SLM. That would be appropriate if the goal were to transmit as much power as possible into a mechanical effect (*i.e.*, transference of OAM to an optically trapped microparticle). However, our immediate goal is to produce, as test beams, close approximations to the LG modes described above. The cylindrical symmetry associated with those modes suggests that we impose a circular aperture on our phase profiles. Without that, the output beams will contain additional energy along the diagonal directions associated with the corners of the SLM. To avoid this effect, I modified the code, to add in this circular aperture, which confines the phase profile to region that is symmetric about the phase singularity. A comparison of generated phase profiles with and without the addition of enforced symmetry are shown in Figure 2.12, for the simple case of $\ell = 1$, and Figure 2.13 compares example output beams, for the case of a superposition of $\ell = 1$ and $\ell = 5$.

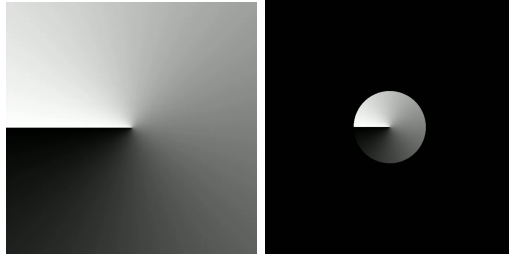


Figure 2.12: A comparison of phase profiles with and without enforced symmetry. At left is a spiral phase profile generated by the original LG.pro program. On the right is a profile of equivalent topological charge, generated by the modified code where a circular aperture is added. The diameter of the aperture is adjustable within the code.

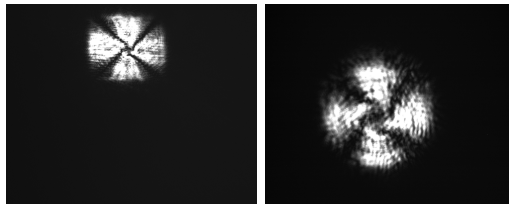


Figure 2.13: A comparison of intensity profiles for output superpositions, with and without enforced symmetry. The beam on the left was generated by the original LG.pro code. The one on the right was generated by the modified version where a circular aperture was applied to the phase profile. Differences in the positions and size of the beams are merely artifacts associated with a change in position of the camera and a change in magnification of the telescope, during re-alignment. The key issue has to do with the heightened degree of circular symmetry in the case on the right.

```

1 ;+
2 ; NAME:
3 ;   ALG
4 ;
5 ; PURPOSE:
6 ;   For creating an approximated, generalized (p not necessarily zero!)
7 ;   Laguerre-Gaussian mode out of a fundamental Gaussian input beam —
8 ;   and, if desired, to shift it away from the undiffracted central
9 ;   spot of the diffractive optic
10 ;
11 ; CATEGORY:
12 ;   Hologram/DOE Generator
13 ;
14 ; CALLING SEQUENCE:
15 ;   ALGmode = alg(l, p)
16 ;
17 ; INPUTS:
18 ;   l: the multiple of 2pi associated with traversal about the center
19 ;   ('azimuthal number')

```

```

20 ;
21 ;   p: the radial index for the LG mode ('radial number')
22 ;
23 ; OPTIONAL INPUTS (KEYWORD PARAMETERS):
24 ;   blaze: the number of 2pi blazings across the field
25 ;         (we've been using 120)
26 ;         — this is effectively adding a prism to refract the beam
27 ;         away from the central spot
28 ;         — increasing 'blaze' is like increasing the angle of the exit
29 ;         face of the prism
30 ;
31 ;   noblaze: if no blazing is desired, this keyword must be set
32 ;           (see RESTRICTIONS below)
33 ;
34 ;   rad: the radius of a circular discontinuity
35 ;       (must fit on the DOE for the beam to sample)
36 ;
37 ;   nbit: provides 2^nbit levels of phase,
38 ;       default setting is 8 (for Hamamatsu x8267 SLM)
39 ;
40 ;   npix: number of pixels on a side,
41 ;       default setting is 768 (for Hamamatsu x8267 SLM)
42 ;
43 ;   orad: outer radius of the profile
44 ;       default setting is 2*npix
45 ;
46 ;   irad: inner radius of the profile
47 ;       default setting is 0 (appropriate to circular aperture)
48 ;
49 ;   ph_max: setting the size of the cone (for the circular aperture,
50 ;         ph_max=2 is recommended)
51 ;         default setting is 1
52 ;
53 ;
54 ; OUTPUTS:
55 ;   LGmode: a npix x npix real array giving a spiral phase plate,
56 ;         with radial phase shifts added
57 ;
58 ; SIDE EFFECTS:
59 ;   For l = 0, p = 0, this creates a blazed diffraction grating
60 ;   (the DOE equivalent of a prism)
61 ;
62 ; REQUIRES:
63 ;   Calibration of the phase levels of the SLM used, for the desired
64 ;   operating conditions, in terms of the 'greyscale' levels used here.
65 ;   An appropriate look-up table (LUT) would allow the images generated
66 ;   by this program to be used directly by the SLM.
67 ;
68 ; RESTRICTIONS:
69 ;   The program does not directly recognize BLAZE = 0.
70 ;   This is a consequence of the way the keyword_set function works.
71 ;   The workaround is to add the argument /NOBLAZE whenever no
72 ;   blazing is desired. (Note that '/no' will work as an abbreviation
73 ;   for '/NOBLAZE', since in general a slash preceding a keyword sets
74 ;   its value to one, and keywords can be abbreviated to their shortest

```



```

75 ;    unique length. For example, a keyword called XSTYLE could be
76 ;    abbreviated to XST)
77 ;
78 ;    Extremely large phase gradients will be 'aliased' due to the
79 ;    discretization of the SLM (the number of phase levels and the size
80 ;    of the pixels).
81 ;
82 ; MODIFICATION HISTORY:
83 ;    Created by Gabe Spalding ,
84 ;    October, 2002
85 ;    Modified by Andy Zhenghao Ding, to enforce cylindrical symmetry,
86 ;    by adding a circular aperture to the phase profile ,
87 ;    Spring, 2017
88 ;-
89
90 FUNCTION alg,l,p,blaze=blaze,noblaze=noblaze,rad=rad,nbit=nbit,$
91     npix=npix,irad=irad,orad=orad,ph_max=ph_max
92
93 IF NOT keyword_set(blaze) THEN blaze = 120
94 IF keyword_set(noblaze) THEN blaze = 0
95 IF NOT keyword_set(rad) THEN rad = 100
96 IF NOT keyword_set(nbit) THEN nbit = 8
97 IF NOT keyword_set(npix) THEN npix = 768
98 IF NOT keyword_set(irad) THEN irad = 0
99 IF NOT keyword_set(orad) THEN orad = 2*npix
100 IF NOT keyword_set(ph_max) THEN ph_max=1
101
102 LGmode=fltarr(npix,npix)
103 offset = long(0.5 * npix)
104 rho_max = SQRT(2*(offset)^2)
105
106 FOR i=0,npix-1 DO BEGIN
107     FOR j=0,npix-1 DO BEGIN
108
109         ; First, create a phase blazing to shift everything away
110         ; from the undiffracted spot:
111         ; (Whenever no blazing is desired, add the argument /noblaze.)
112         LGmode(i,j) = i * (2*!pi) * blaze/(npix-1)
113
114         ; Next, convert this refracted spot to a p=0 LG mod
115         ; by creating a spirial phase plate:
116         ; The azimuthal angle is given by
117         theta = ATAN(j-offset, i-offset)+!pi
118         ; A term containing the azimuthal angle multiplied by
119         ; the azimuthal number creates the spiral phase plate:
120         LGmode(i,j) = LGmode(i,j) + l * theta
121
122         ; Now, find how far the present pixel is from the center
123         ; of the diffractive optical element (DOE)
124         rho = SQRT((i-offset)^2.0 + (j-offset)^2.0)
125
126         ; Use this radius as a criteria for adding further phase shifts that
127         ; depend upon the radial number:
128         IF p GT 0 THEN BEGIN
129             FOR pindex = 1, p DO BEGIN

```

```

130         ; For non-zero radial number, the DOE will contain p circles ,
131         ; with sizes given by:
132         circline = pindex*rad
133         ; Beyond each of those circles , we add a pi phase shift ,
134         IF rho GE circline THEN LGmode(i,j) = (LGmode(i,j) + !pi)
135     ENDFOR
136 ENDIF
137
138     ; These are the lines I added to the original program to produce a
139     ; circular aperture to the phase profile
140     IF rho LT irad*(rho_max/ph_max) THEN LGmode(i,j) = 0
141     IF rho GT orad*(rho_max/ph_max) THEN LGmode(i,j) = 0
142
143
144     ENDFOR
145 ENDFOR
146
147 modulo = 2*!pi
148 LGmode = LGmode - (modulo * long(LGmode/modulo))
149
150     ; Finally , scale everything from units of phase to units of
151     ; 'image level'
152 LGmode = LGmode*((2^nbit-1)/(2*!pi))
153     ; The extra parentheses above improve efficiency:
154     ; otherwise the precedence of multiplication over division would mean
155     ; that the array would be operated on twice.
156
157 return ,LGmode
158 END

```

2.4 Aberration Correction

2.4.1 Iterative phase optimization algorithms

We have made use of several optimization algorithms which are based, to varying degrees upon

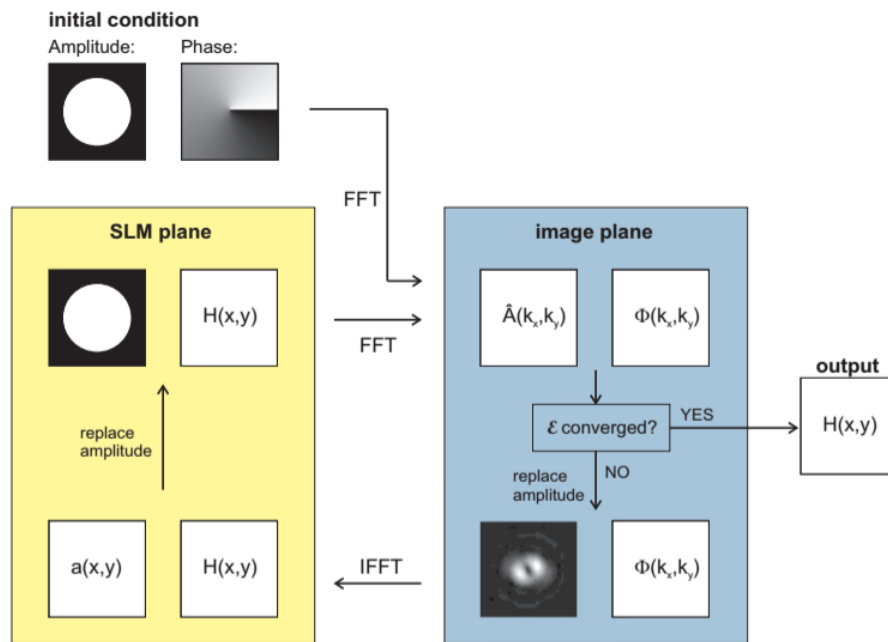


Figure 2.14: A schematic of the Gerchberg-Saxton algorithm, from “Wavefront correction of spatial light modulators using an optical vortex image” by A. Jesacher, A. Schwaighofer, S. Fuehapter, C. Maurer, S. Bernet, and M. Ritsch-Marte

an approach popularized by Ralph Gerchberg and Owen Saxton.[25] The basic Gerchberg-Saxton (GS) algorithm, illustrated in Figure 2.14, is an iterative process that converges to an approximate phase profile appropriate to some target intensity distribution in the Fourier plane of the SLM. As a starting point, the algorithm typically begins by initializing the phase at each pixel, $H(x, y)$, on the diffractive optical element (in our case, the SLM) to a random value. While it is possible to specify the measured input intensity profile (in our case, the fundamental Gaussian mode), this

simply results in the convolution of each point in the output with a Gaussian, and so for simplicity we perform all calculations assuming a uniform intensity profile, and therefore a uniform field amplitude, $A(x, y)$, at each pixel of the SLM. This starting distribution of amplitude and phase, $A(x, y)e^{iH(x, y)}$, is fast-Fourier-transformed (FFT) to yield the distribution in the Fourier plane, $\hat{A}(k_x, k_y)e^{i\Phi(k_x, k_y)}$. The intensity part of this output distribution is compared with the target intensity profile, generating an error function ϵ (which may be constructed in a variety of ways) with a threshold value determining acceptability (set according to the needs of the experiment, and the willingness to spend computational time upon further optimization). If the error is larger than the threshold value, the desired intensity profile $\hat{A}(k_x, k_y)$ is substituted for the calculated intensity profile, while the calculated phase profile $\Phi(k_x, k_y)$ will be preserved, and the composite amplitude and phase transformed back to the SLM plane using the inverse FFT. At this point, the intensity profile that results from the inverse FFT is changed back to the initial (uniform intensity) profile, while the phase profile created by the inverse FFT is preserved, and the composite amplitude and phase profile will then be transformed, via FFT, to the Fourier plane again and compared with the target intensity profile. Again, if the error function is smaller than the desired value, the phase profile is accepted as a final approximation. If not, iteration repeats until the error ϵ is small enough. For distributions with a high degree of symmetry, the error function typically converges after several iterations. A variation of the GS algorithm introduced and popularized by Eric Dufresne and Dr. Spalding and their co-authors is the Adaptive-Additive (AA) algorithm, which, in comparison to the GS algorithm takes smaller steps towards the desired intensity distribution.[12] The AA version tends to yield outputs with less unintended variation in the final intensity profile produced.

2.4.2 Integrating the Adaptive-Additive algorithm into the Ritsch-Marte method for Aberration Correction

In 2007, Monika Ritsch-Marte proposed a method for aberration correction, based upon a combination of the Gerchberg-Saxton algorithm for phase optimization with the use of LG modes as test beams (valued for this purpose because of the distributed nature of the intensity patterns produced, as well as their “good dark” and high degree of symmetry).[17] Her method begins by sending an LG beam through the system to be optimized, and capturing the (aberrated) intensity profile with

a camera. This (undesirable) intensity profile is then used, somewhat counter-intuitively, as the *target* intensity distribution in the GS algorithm, as a means of approximately determining the phase profile of associated with aberrated measurement at the camera. By examining the *difference* between the phase profile output by the GS algorithm and the expected spiral phase profile, Ritsch-Marte was able to determine a phase profile required for correcting the observed aberration in the system. This Ritsch-Marte method converges only in the limit of weak aberration, but is nevertheless appropriate to our experiments for this thesis.

In my version, the AA algorithm is implemented instead of the GS algorithm. I implemented that part of the Ritsch-Marte method by using an IDL program written by Eric Dufresne, Prof. Gabe Spalding and Toan Le (and reproduced below). To correct for aberration arising anywhere in our LG beam-generation system, we first take an image of the intensity profile of the LG beam at the front focal plane, and use the AA algorithm to calculate an approximation to the phase profile that produced that measured intensity distribution. Then we subtract this phase profile from the LG beam phase profile, and add this result to the phase profile we program into the SLM.

```

1 ;+
2 ; NAME:
3 ;     PHASE
4 ; PURPOSE:
5 ;     Calculates the phase function of a hologram.
6 ;     The hologram does its best to produce the
7 ;     desired intensity profile in the focal plane
8 ;     of a lens.
9 ;
10 ; CALLING SEQUENCE:
11 ;     ph = phase(out)
12 ; INPUTS:
13 ;
14 ;     out: a n x n real array
15 ;         describing the desired intensity field in the
16 ;         focal plane of the lens.
17 ;         (fastest if n is a power of 2)
18 ;         The Boulder 512x512 SLM has n = 2^9, which is nice
19 ;         The Hamamatsu x8267 uses 768x768 images, which is
20 ;         not a power of two, but works. — Also note that
21 ;         768x768 can be tiled by 256x256 or 128x128.
22 ;         Also, once upon a time, I calculated 512x512 images
23 ;         and just used CONGRID to blow that up to 768x768
24 ;         (I'm not sure how well that worked.)
25 ;
26 ; KEYWORDS:
```

```

27 ;      ipix: the pixel size of the image describing the input. (in mm)
28 ;          Note that this is determined by the diameter of the back aperture
29 ;          of the objective lens used for tweezing/making the hologram
30 ;          For example, although Kishan's Boulder SLM has a 15-micron pitch, these
31 ;          are imaged by a telescope onto the back aperture of an OL, where their
32 ;          size is effectively much smaller, so it would be a mistake to set ipix
33 ;          =0.015 mm. Similarly, Gabe's Hamamatsu PPM contains physical pixels
34 ;          around 0.024 mm in size, but it would be a mistake to set ipix=0.024
35 ;          for this Hamamatsu x8267 — the projected pixel size on the back
36 ;          aperture of the OL is much smaller.
37 ;
38 ;          For an Olympus microscope using infinity optics, the tube length is
39 ;          180 mm,
40 ;          so the diameter of the back aperture is 2*180*NA/mag
41 ;          Thus, Gabe's 100x NA=1.40 lens has a back aperture of 5.04 mm
42 ;
43 ;          For now suppose there is no significant overfilling of the
44 ;          back aperture,
45 ;          so that the SLM is focused down to a 5.04-mm square, yielding
46 ;          ipix=5.04mm/512 for the Boulder
47 ;          and ipix=5.04/768 for the Hamamatsu x8267.
48 ;
49 ; The program should be rephrased in terms of the true pixel size of the SLM
50 ; and the demagnification factor used in projecting the SLM onto the
51 ; back aperture.
52 ;
53 ;      f: the focal length of the lens used to form the
54 ;          image in mm (The 100x lens I used in Chicago had f = 1.62)
55 ;          For an Olympus microscope using infinity ('UIS') optics,
56 ;          the tube lens has a focal length of 180 mm, so for the objective lens
57 ;          the focal length (in mm) is 180/mag.
58 ;          Though Gabe also has a 100x Olympus lens that is NOT designed for UIS
59 ;          optics, the lenses on Gabe's IX-71 microscope are.
60 ;          For that (UIS) 100x lens, f = 1.8
61 ;
62 ;      in: a n x n real array (of the same size as out), describing
63 ;          the intensity field of the illuminating beam
64 ;          incident upon the hologram.
65 ;
66 ;      lambda: the wavelength of light in mm
67 ;          (1064 nm = 10.64e-4 mm is for Kishan's Boulder SLM)
68 ;          Gabe's Hamamatsu SLM uses 5.32e-4 mm
69 ;
70 ;      nmax: the maximum number of iterations
71 ;
72 ;      iph: initial guess for the phase
73 ;
74 ;      min_er: the percentage change in the error between the
75 ;          ideal and calculated output plane images between
76 ;          successive iterations at which the program
77 ;          considers the calculation to have converged
78 ;
79 ;      lowg: low graphics mode. Only shows end result.
80 ;
81 ;      nog: no graphics mode

```

```

82 ;
83 ;           pr: draw graphics for printing
84 ;
85 ; OUTPUTS:
86 ;           ph: a n x n real array giving the phase at the
87 ;               hologram
88 ;
89 ; NOTES:
90 ;           Though millimeters are the standard choice
91 ;           — lambda, f, and ipix can be specified in arbitrary but consistent units.
92 ;           Together, these simply determine the scale of the image formed
93 ;           by the hologram
94 ;           (see dxo)
95 ;
96 ; MODIFICATION HISTORY:
97 ;           Created by Eric R. Dufresne, 4/98
98 ;           Modified by ERD, 7/13/98, 7/14/98
99 ;           Modified by ERD, 3/03/99:
100 ;                to use memory more efficiently, at the loss of
101 ;                a little speed. This will allow calculation
102 ;                of bigger arrays
103 ;           Modified by Gabe Spalding, September, 2002, for use with
104 ;                Spatial Light Modulators
105 ;           Further modified 7/17/03 — Gabe Spalding
106 ;           Modified by Toan Le as noted below, 1/13/2017
107 ;—
108
109 function phase, out, lambda=lambda, f=f, ipix=ipix, nmax=nmax, min_er, iph=iph, lowg=lowg, $
110     nog=nog, pr=pr, af_er=af_er, in=in
111
112 ; For the Hamamatsu x8267's 768 pixels projected onto the
113 ; 5.04-mm aperture of Gabe's 100x infinity-corrected objective:
114 ; if not keyword_set(ipix) then ipix=5.04/768.
115 ; if not keyword_set(lambda) then lambda=5.32e-4
116 ; if not keyword_set(f) then f=1.8
117
118 ; For the Hamamatsu x8267's 768 pixels and 60x infinity-corrected objective:
119 ; (modified by Toan Le- 1/13/2017)
120 if not keyword_set(ipix) then ipix = 0.012
121 if not keyword_set(lambda) then lambda = 5.32e-4
122 if not keyword_set(f) then f = 3
123
124 ; For the Hamamatsu x7550's 480 pixels projected directly from the SLM:
125 ; if not keyword_set(ipix) then ipix=20./480.
126 ; if not keyword_set(lambda) then lambda=6.33e-4
127 ; if not keyword_set(f) then f=160
128
129 ; For the Boulder's 512 pixels projected onto the
130 ; 5.04-mm aperture of Gabe's 100x infinity-corrected objective:
131 ; if not keyword_set(ipix) then ipix=5.04/512.
132 ; if not keyword_set(lambda) then lambda=10.64e-4
133 ; if not keyword_set(f) then f=1.8
134
135 ; For Gabe's etched-in-glass 512x512 holograms projected onto the
136 ; 3.2-mm aperture of the OL Gabe used at UChicago

```

```

137 ; we (historically) took ipix to be:
138 ; ipix = 0.00633
139 ; if not keyword_set(lambda) then lambda=5.32e-4
140 ; if not keyword_set(f) then f=1.62
141
142 ; As a favor for Molly Rose Darragh, 128 pixels projected onto the
143 ; 5.04-mm aperture of her objective:
144 ; if not keyword_set(ipix) then ipix=5.04/128.
145 ; if not keyword_set(lambda) then lambda=5.32e-4
146 ; if not keyword_set(f) then f=2.74
147
148
149 if not keyword_set(nmax) then nmax=100
150 if not keyword_set(min_er) then min_er=1.e-5
151 if not keyword_set(lowg) then lowg=0
152 if not keyword_set(nog) then nog=0
153 if not keyword_set(pr) then pr = 0
154
155 ;FIND THE LINEAR SIZE OF THE IMAGES IN PIXELS
156 nx = n_elements( out[0,*] )
157
158 ;CALCULATE THE NORMALIZATION FACTORS FOR THE ERRORS
159 nerf = total ( out )
160 if keyword_set(in) then nerw = total(in) else nerw=float(nx^2)
161
162 ;DEFINE THE AMPLITUDE OF THE COMPLEX FIELDS OF THE INPUT BEAM
163 ;GENERATE AN INPUT IF IT IS NOT SUPPLIED
164 if not keyword_set(in) then a0 = replicate(1.,nx,nx) else a0=sqrt(in)
165 ;THE DESIRED OUTPUT - Conserve energy.
166 b0 = sqrt( out * (nerw / nerf) )
167
168 ;DEFINE THE PIXEL SIZE IN THE INPUT PLANE
169 dxi = ipix
170 ;DEFINE THE PIXEL SIZE IN THE OBSERVATION PLANE
171 dxo = lambda * f / ( nx * dxi )
172
173 ;CREATE THE SCALES FOR THE IMAGES
174 xin = findgen(nx) * dxi
175 xout = findgen(nx) * dxo
176
177 ;MAKE AN INITIAL GUESS FOR THE PHASE FUNCTION
178 if not keyword_set(iph) then $
179   ph = exp(complex(0.D0 ,2.D0 * !dpi * randomu( seed , nx , nx ))) $
180   else ph=cexp(0,iph)
181
182 ;ASSIGN A VALUE TO THE ADAPTIVE-ADDITIVE WHAMMY FACTOR
183 s=0.5D0
184
185 i=0
186 der=1
187 math_err=0
188 while (i lt nmax) and (abs(der) gt min_er) and (math_err eq 0) do begin
189   i = i+1
190
191

```



```

192
193 ;print ,1 ;Debugging index
194
195 ;CALCULATE THE FIELD IN THE OBSERVATION PLANE
196 f = shift(fft( a0 * ph, /double ),nx/2,nx/2)
197 ;absf = abs(f) ;Comment out if memory is the limitation
198 ;Make the substitution throughout otherwise
199 ;CALCULATE THE ERROR
200 new_af_er = total ( (abs(f) - b0 )^2 ) / nerf
201
202 if lowg eq 0 and nog eq 0 then $
203 ; dgcont_image , bytscl(abs(f)^2),1000*xout,1000*xout,/nocont,/aspect , $
204 ; xtitle='Microns in focal plane.',title='Intensity in focal plane.'
205
206 ;print ,2 ;Debugging index
207
208 ;USE ADAPTIVE ADDITIVE ALGORITHM TO MAKE CORRECTION
209 f = s * b0 * f / abs(f) + ( 1 - s ) * f
210 ;Could we improve the efficiency of array operations above?
211
212 ;print ,3 ;Debugging index
213
214 ;TRANSFORM BACK TO INPUT PLANE
215 w = fft ( shift(f,-nx/2,-nx/2) , /inverse , /double )
216 ;abs(w)=abs(w) ;Comment out if memory is the limitation
217 ;Make the substitution throughout otherwise
218
219 ;if lowg eq 0 and nog eq 0 then $
220 ; dgcont_image , bytscl(abs(w)^2),xin,xin,/nocont,/aspect,$
221 ; xtitle='Millimeters in DOE plane.',title='Backwards Intensity at DOE'
222
223 ;print ,4 ;Debugging index
224
225 ;CALCULATE OUR NEW GUESS FOR THE PHASE
226 ;MAKE SURE THE ANSWER IS SENSICAL
227 if n_elements( where(finite(w/abs(w)) eq 0) ) eq 1 then ph=w/abs(w) else begin
228 print , 'Oops! There was a math error.'
229 math_err=1
230 endelse
231
232 if lowg eq 0 and nog eq 0 then $
233 ; dgcont_image , bytscl(cphase(ph)),xin,xin,/aspect,/nocont,$
234 ; xtitle='Millimeters in DOE plane.',title='DOE phase shift.'
235
236 ;print ,5 ;Debugging index
237
238 ;CALCULATE THE CHANGE IN THE ERRORS
239 if i ne 1 then der = (new_af_er-af_er)/af_er else der=1.
240 af_er = new_af_er
241 ;w_er = total ( (abs(w) - a0 )^2 ) / nerw
242 ;print , 'The input error:',w_er
243
244 ;DISPLAY THE ERRORS
245 ;print , 'The ouput error:',new_af_er
246 print , 'Iteration #' + strtrim(string(i),2) , ' ' The % change in error:',der

```

```

247     print
248
249 endwhile
250
251 if nog ne 1 then begin
252     if pr eq 1 then begin
253         ;!p.multi=[2,2,0]
254         ;dgcont_image , bytscl (in) ,xin ,xin ,/nocont ,/ aspect , $
255         ; /invert , xtitle='Millimeters in DOE plane.' , title='Input Beam'
256 erase
257         ; dgcont_image , bytscl (cphase(ph)) ,xin ,xin ,/ aspect ,/ nocont , $
258         ; xtitle='Millimeters in DOE plane.' , title='DOE phase shift.'
259
260         ; dgcont_image , bytscl (abs(f)^2) ,1000*xout ,1000*xout , $
261         ; /nocont ,/ aspect , $
262         ; /invert , xtitle='Microns in focal plane.' , $
263         ; title='Intensity in focal plane.'
264         ; !p.multi=0
265     endif else begin
266
267         !p.multi=[2,2,0]
268         ; dgcont_image , bytscl (in) ,xin ,xin ,/nocont ,/ aspect , $
269         ; xtitle='Millimeters in DOE plane.' , title='Input Beam'
270 erase
271         ; dgcont_image , bytscl (cphase(ph)) ,xin ,xin ,/ aspect ,/ nocont , $
272         ; xtitle='Millimeters in DOE plane.' , title='DOE phase shift.'
273
274         ; dgcont_image , bytscl (abs(f)^2) ,1000*xout ,1000*xout , $
275         ; /nocont ,/ aspect , $
276         ; xtitle='Microns in focal plane.' , $
277         ; title='Intensity in focal plane.'
278         !p.multi=0
279
280     endelse
281
282 endif
283 ; help
284 return , cphase(ph) + !pi
285 end

```

2.4.3 Application of Ritsch-Marte/AA aberration correction method

In our lab at IWU, the Ritsch-Marte/AA aberration correction method was applied by using a test beam with $\ell = 5$. The initial, *uncorrected* intensity distribution is shown in Figure 2.15, along with the initial phase profile programmed onto the SLM. At far right is the ring-shaped intensity profile which results at the end of our correction process. We used the phase.pro program shown in the

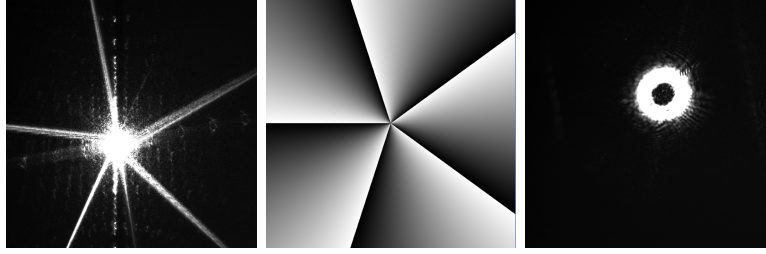


Figure 2.15: At left is an uncorrected $\ell = 5$ intensity profile the front focal plane. The middle shows its associated phase profile on the SLM. At right is the corrected, ring-shaped beam.

previous subsection to associate a phase profile with the uncorrected image, then subtracted the difference in phase from the original spiral phase profile, and defined this as an (initial) correction factor to be applied to all subsequent phase profiles written to the SLM. However, we found that repeating the process twice more provided additional gains, and so the final correction fact is a result of those additional iterations.

2.5 Transformation Optics: rapid readout of OAM

2.5.1 Introduction to the Lavery method of OAM readout

Dr. Martin Lavery of the University of Glasgow developed a set of transformation optics that can rapidly read out the orbital angular momentum content associated with a superposition of LG modes. The following discussions on the transformation optics are all following Dr. Martin Lavery's thesis and his other works on related topics. [21] [13] [20] The Lavery conformal mapping, as a first step, effectively amounts to performing a Cartesian-to-polar coordinate transformation.[21] This mapping will “unwrap” a single-mode ring-shaped Laguerre-Gaussian beam into a straight line that is displaced from the optical axis by the radius of the LG ring, which is calculated below. For a single-mode LG beam, the radius of the ring can be determined from,[21] the topological charge of the beam, ℓ , and the size of the circular aperture of the phase profile, d , described earlier in our section on IDL programming.

$$r_\ell = \frac{\lambda f}{d} \ell \quad (2.26)$$

An additional step compensates for a remaining phase gradient associated with the output line of light. After the Lavery transformation optics, we pass this displaced line of light through a cylindrical lens, which means that the beam is focused to a specific location on the camera. The distance between this location and the optical axis directly maps onto the ℓ -value of the single LG mode used as input. Clearly, then, if a superposition of LG modes is input, the output should yield a discrete array of spots on the camera, which can be directly read as the encoded OAM information.

2.5.2 Mathematical expression of the Lavery Transform

Optical geometric transformation has previously been studied in the context of optical image processing. [21][8] Transformation can be implemented using a set of lenses only if the mapping is

conformal. To elaborate, assume the amplitude profile in the z plane is denoted as $A(x, y)$, then the amplitude profile in the w plane is related via a Fourier transform that includes the conformal mapping phase profile $\phi(x, y)$: [8]

$$\tilde{A}(u, v) = \int \int_{-\infty}^{+\infty} dx dy A(x, y) e^{i[\phi(x, y) - k(xu + yv)/f_L]} \quad (2.27)$$

That is, we are mapping intensity from input plane coordinates (x, y) onto output plane coordinates (u, v) : $(x, y) \rightarrow (u, v)$. This mapping is described by a construct $w = f(z) = u(x, y) + iv(x, y)$, which must satisfy equation 2.10, one of the Cauchy-Riemann equations.[8]

$$\frac{\partial u(x, y)}{\partial y} = \frac{\partial v(x, y)}{\partial x} \quad (2.28)$$

Note that Equation 2.26 involves an integral of the following general form:

$$\int \int g(x, y) e^{ikh(x, y)} dx dy \quad (2.29)$$

Using a saddle-point method, we can find an approximation for large k values. The saddle point can be found using the following equation. [8]

$$\frac{\partial h}{\partial x} = \frac{\partial h}{\partial y} = 0 \quad (2.30)$$

For the integral at hand, $h(x, y) \equiv [\phi(x, y) - k(xu + yv)/f_L]$, so we have

$$\begin{aligned} \frac{\partial \phi(x, y)}{\partial x} &= \frac{k}{f_L} u(x, y) \\ \frac{\partial \phi(x, y)}{\partial y} &= \frac{k}{f_L} v(x, y) \end{aligned} \quad (2.31)$$

As we are performing a Cartesian-to-polar transformation, we assume that

$$\begin{aligned} u(x, y) &= \sqrt{x^2 + y^2} \\ v(x, y) &= \arctan(y/x) \end{aligned} \quad (2.32)$$

However, applying the conformal mapping condition in equation 2.22, we have [8]

$$\begin{aligned} \frac{\partial u(x, y)}{\partial y} &= \frac{x}{\sqrt{x^2 + y^2}} \\ \frac{\partial v(x, y)}{\partial x} &= \frac{-y}{x^2 + y^2} \end{aligned} \quad (2.33)$$

It is clear that $\frac{\partial u(x,y)}{\partial y} \neq \frac{\partial v(x,y)}{\partial x}$. As a result, we change the transformation into a log-polar transformation, which is shown below. [21] [13] [20]

$$\begin{aligned} u(x, y) &= -a \cdot \ln(\sqrt{x^2 + y^2}/b) \\ v(x, y) &= a \cdot \arctan(y/x) \end{aligned} \quad (2.34)$$

Substituting the above transformation into equation 2.26, we can get the following expression for the phase modulation.[21] [13] [20]

$$\phi_1(x, y) = \frac{2\pi a}{\lambda f} \left[y \cdot \arctan\left(\frac{y}{x}\right) - x \cdot \ln\left(\frac{\sqrt{x^2 + y^2}}{b}\right) + x \right] \quad (2.35)$$

However, this mapping introduces a phase distortion to the wavefront that needs to be corrected by introducing a *second* phase modulation optic. We can calculate the far-field amplitude of a plane wave that has passed through the first element by using the stationary phase approximation. The amplitude is shown below.[21][13]

$$A_2(x, y) = e^{i\phi_1(x,y) - i\frac{k}{f}(xu+yv)} \frac{2\pi}{\sqrt{\left|\frac{\partial u}{\partial x} \frac{\partial v}{\partial y} - \left(\frac{\partial u}{\partial y}\right)^2\right|}} \quad (2.36)$$

The desired second element is just the inverse of this phase profile. That is, $\phi_2(u, v) = -arg(a_2)$, so we have [21][13]

$$\phi_2(u, v) = -ab\frac{k}{f} e^{-\frac{u}{a}} \cos\left(\frac{v}{a}\right) \quad (2.37)$$

Now we have mathematical expressions for two optical elements, which together complete the desired transformation. Again, the discussion provided here largely follows Dr. Lavery's Ph.D thesis, "Measurement of Light's Angular Momentum." Interested readers can find this thesis and relevant work in the reference.

2.5.3 Experimental setup and alignment for OAM readout

Measuring encoded OAM information via these transformation optics obviously requires that we generate, as inputs, well-controlled LG beams. We wish to examine the response to various LG inputs (*i.e.* beams characterized by a various values of the topological charge, ℓ , including superpositions. For this, our setup, shown in Figure 2.16, closely resembles the one shown earlier in Figure

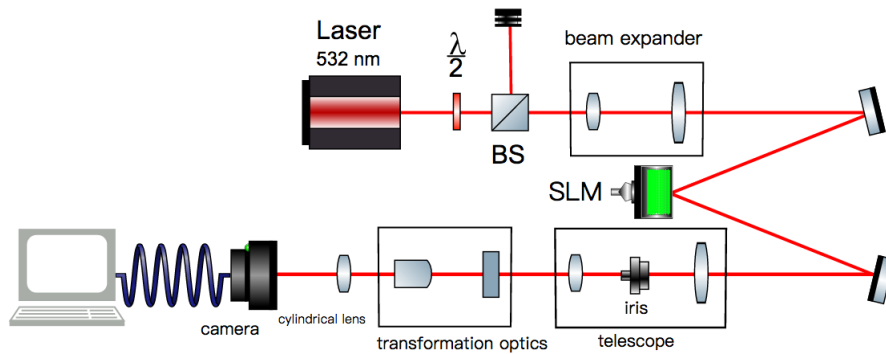


Figure 2.16: Test setup for measuring OAM

2.2, but has the addition of the transformation optics as well as the addition of a spatial filter, which serves as a mode sorter, between the SLM and the input to the transformation optics provided by Dr. Martin Lavery. This mode sorter consists of a telescope, which also serves to adjust the size of the beam for the transformation optics, and an iris for filtering out all the other beams with different orders other than one, as we have imposed a blazing to separate, spatially, components of the beam which are associated with different orders. The iris should be placed at the focal point of the telescope. Aligning the transformation optics requires a specific set of procedures, provided by Dr. Martin Lavery over private communication and the steps are reproduced below. [19]

1. The first step is to measure out an appropriate distance between the two transformation optic elements, adjusted according to the dispersion in the PMMA, using the calibration shown in Figure 2.17. Once corrected for wavelength, leave as is.

2. The analysis of an OAM spectrum is highly sensitive to alignment along the optic axis (both direction and displacement). Therefore it is essential that the optical path be stable and aligned to the beam axis of the input mode. Remove the first element of the transformation optics and then, using two apertures, approximately at the position of each element, walk the input beam (using mirrors omitted from the test setup schematic) to assure the beam travels through each element straight over the (roughly) 30 cm between elements. Stable mirror mounts are required. (Beam

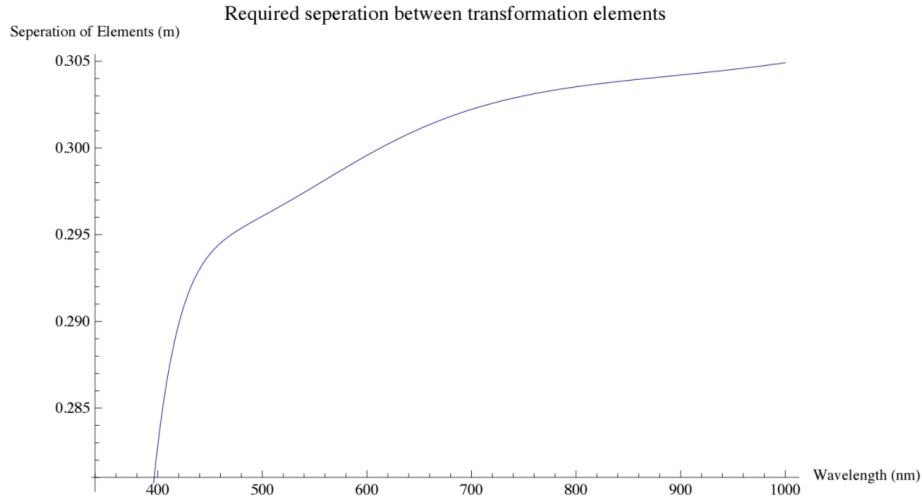


Figure 2.17: Required distance between transformation optics elements, as a function of wavelength. The graph is provided by Dr. Martin Lavery in his tutorial for alignment [19]

walking is also required to set up the mode sorter, so there are multiple mirrors omitted from the schematic).

3. Use the SLM to generate a superposition of LG modes. *e.g.*, $\ell = 5 + \ell = 1$, shown below in Figure 2.18, along with the beam generated in the lab. The resulting interference pattern for that particular superposition should yield an intensity distribution at the input to the sorter comprising a round beam containing four lobes. Adjust the mode “size and weight” settings on the SLM to

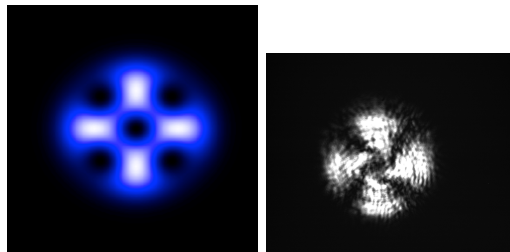


Figure 2.18: On the left is a computer simulation for the intensity distribution, at the input of our analysis optics, for a superposition of $\ell = 5$ and $\ell = 1$. At right we present the actual intensity distribution measured in our lab. The simulation software is provided by Dr. Martin Lavery over private communication. [19]

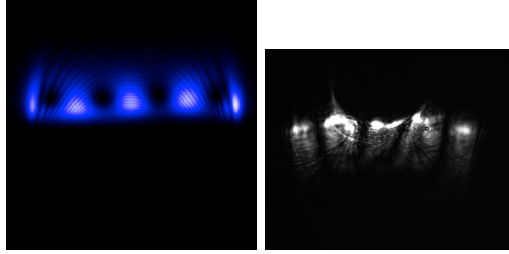


Figure 2.19: The image on the left shows the expected transform of the $\ell = 5$ and $\ell = 1$ superposition. The image at right shows the actual measured result from our lab at IWU. The simulation software is provided by Dr. Martin Lavery over private conversation. [19]

produce the expected interference pattern.

4. Align this input mode with respect to the first element of the sorter. Inspect the intensity distribution in plane of the second element, where an “unwrapped” version should appear as a straight line containing four equally spaced black spots. (Figure 2.19 shows the simulated expected result, along with an image of the measured result taken in our lab at IWU.) Tweak the position of the first element with respect to the beam: preferably, you will only need to use two mirrors to control the input direction.

5. Now look at the beam after it has been allowed to propagate freely for 10-20 cm following the second element. Adjust the second element (the phase corrector) so that the beam is still a straight line at this point. A misaligned beam will normally appear as two half circles adjacent to each other. Align left-to-right so that the join point is in the center, then align up-to-down to make the result straight.

6. Now go back to single values of ℓ and adjust the second element further to ensure that an elongated spot is observed.

7. Then use the SLM to generate, again, a superposition of LG modes, *e.g.*, $\ell = -7, -1, +1$ and $+7$. And confirm that the positive and negative components look the same. If the result is not symmetric about $\ell = 0$, then input mode is misaligned with respect to the sorter.

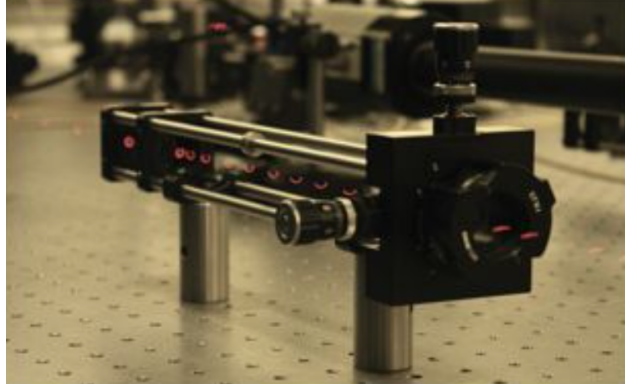


Figure 2.20: When aligned, the Lavery transformation optics act as a “donut-to-hotdog” converter of optical topology. The photo is from Dr. Martin Lavery’s thesis, “Measurement of Light’s Angular Momentum” and relevant publications. [21] [13] [20]

8. Adjust the input position and tilt of incident beam. Control of tilt via the SLM is a very useful approach. To do this image the plane of the SLM to the plane of the first element. Then change (slightly) the number of blazing lines on the SLM, which will fine tune the angular tilt of the incident beam.
9. Repeat Steps 6 - 8 until the beam is straight. The behavior of the transformation optics is shown in Figure 2.20.

Important tips

1. Before alignment, it is important to check if the elements of the transformation optics ordered in the correct sequence. The transformation will not work if the phase correction element is placed before the log-polar mapping element.
2. The size of the beam coming into the transformation optics matters a lot. If the beam is too small, it will be very hard to align the system, and there will be no obvious change of the location of the focused spot on camera when switching to different topological charges.

2.5.4 First implementation of the transformation optics

In our lab in IWU, we are applying Laguerre-Gaussian beams with different values of ℓ to the transformation optics. According to the previous section on transformation optics, these LG beams will be focused to separate points on a line. In our lab in IWU, we are applying Laguerre-Gaussian beams with different values of ℓ to the transformation optics. Again, these LG beams will be focused to separate points on a line, but as our interest has to do with examining the *robustness* of this method, and the degree to which aberration correction methods may be useful, Figure 2.21 zooms in to highlight the details associated with the experimental outputs achieved at IWU.

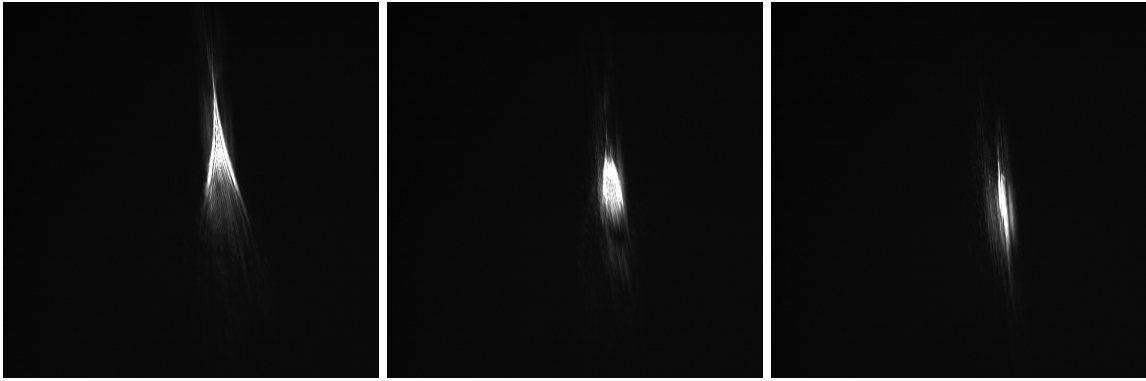


Figure 2.21: The image on the left shows the focal “point” for $\ell = 1$. The one in the middle is for $\ell = 10$. The one on the right is for $\ell = 20$.

Over the range of ℓ values shown, the result optimized by our aberration correction is shown in the middle frame, and aberration clearly increases as we move away from that ℓ value. Future work should look at improving optimization over a broad range of ℓ values.

2.6 Vaterite Synthesis

2.6.1 The desire for Birefringent Spheres

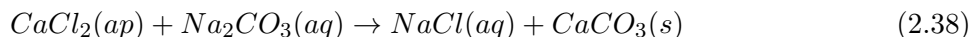
For studies involving transfer of angular momentum, we want to prepare microscopic versions of the wave plates used in Chapter 1. These birefringent materials can, for example, change left-circularly polarized light into right-circularly polarized light, and therefore by conservation of angular momentum, since the angular momentum content of the light has been altered there must be a optical torque acting on the wave plate. Because optical forces and torques are quite feeble, and because the mesoscopic physics of interest to our lab, we wish to fabricate birefringent micro-particles and nano-particles. For situations where we are interested in full analysis, use of a *spherical* particle offers clear advantages. After all, there are only three geometries which have, to date, allowed analytic, closed form solutions for hydrodynamic drag: the best known of these is Stoke's drag, which applies (only) to an isolated sphere immersed in fluid and far from any other surfaces. Vaterite is a spherical form of hydrated calcium carbonate. While it is not as strongly birefringent, its spherical shape makes it of interest for a variety of experiments involving optical trapping and experimental analysis of the transference of light's orbital angular momentum. [7]

2.6.2 Synthesis protocols

The general idea is to use a non-reactive agent as a mediator to slow down the reaction rate and stabilize the crystal growth. During the synthesis process, calcium chloride and sodium carbonate are dissolved in 83.3% ethylene glycol solution separately. The ethylene glycol here acts as the mediator. Then they are mixed up with each other and the solution is stirred for an extended period. After stirring, the particles are taken out of the solution by centrifugation. They are subsequently washed and stored in alcohol to preserve their birefringence for a few days.[3] [2]

The formula for this reaction is shown in equation 2.9. The procedures are shown as below. This

recipe is provided by Yoshi Arita.



1. Take 50 ml fresh ethylene glycol and 10 ml deionized water. mix them together
2. Weigh 0.525g Na_2CO_3 , and 0.55g CaCl_2 and dissolve them separately into two 15ml 83.3% ethylene glycol-water solution
3. Mix them together and stir with a stir bar. The reaction will take 3 hours.
4. Centrifuge the solution for 15 min * 3 rounds. Every time, remix the particles back to the solution using vortex mixer
5. Wash the particles with ethanol for 5 min * 3 rounds
6. Re-suspend the particles in fresh ethanol, diluted.

The volumes indicated above are not fixed: they can be changed to adapt different experimental conditions, as long as the *concentrations* are the same as the ones in the procedures provided above.

2.6.3 Important tips

Here are some important tips and ideas to vaterite synthesis.

Effect of reaction time up particle dimensions

Currently, the length of time for the reaction is known to be related to the size of the particles synthesized. However, the exact relationship between reaction time and dimension of vaterite is yet unknown to me. If the reaction is 3 hours, the size will be around 1 micron. This would be something to look into during later vaterite synthesis research.

Conditions of ethylene glycol

According to information from Yoshi Arita from University of St Andrews, Scotland, the ethylene glycol needs to be fresh. Otherwise the vaterite will be elongated or even cubical. As a result, every time we need to make new solutions for the reaction. The leftovers should be thrown away without hesitation.[3]

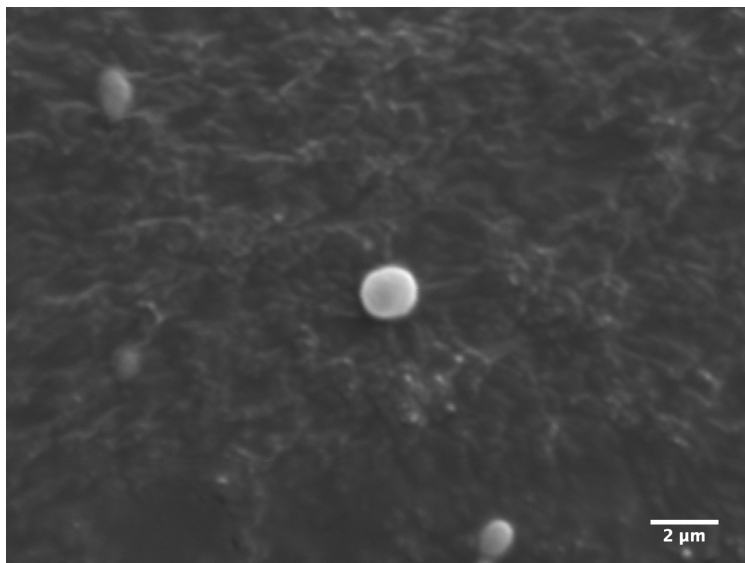


Figure 2.22: Vaterite crystal synthesized in IWU

Additional protocol details

The stirring rate needs not be too strictly controlled, although few researches is done regarding how this is affecting the result. This could be something to look into in later research. Also, the rate of mixing and the mixing direction, *i.e.*, which one is mixed into the other, do not matter in the experiment. Certain experiments have been done and no obvious change has been observed. However, the part temperature plays in the experiment is not clear. My guess is that higher temperature speeds up the process and increases the size of the vaterite crystals.

2.6.4 The polydisperse ensembles produced

This is a picture of one of our vaterite crystals taken using a scanning electron microscope. Figure 2.23 shows the distribution of sizes we achieved for the vaterite we made using the procedures above.

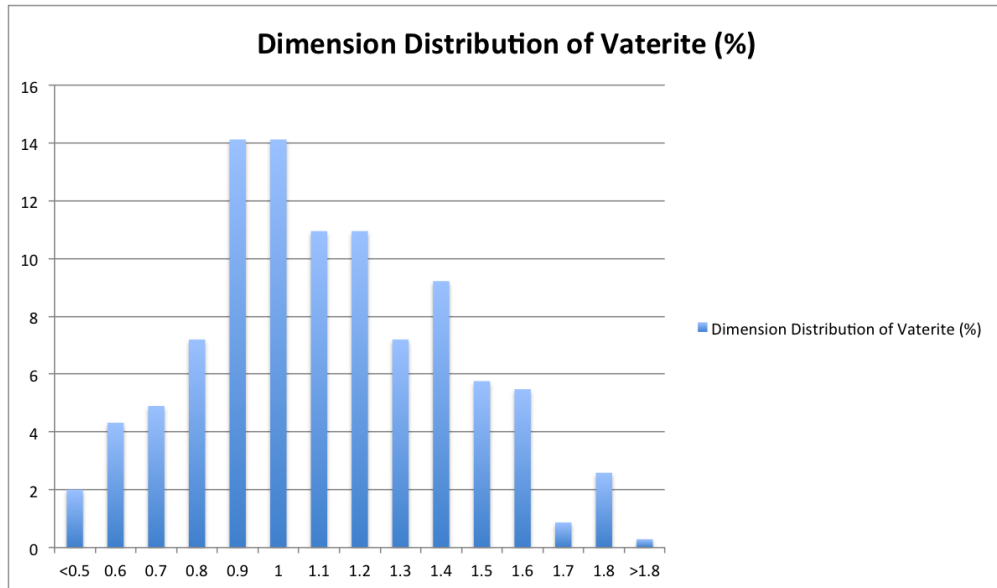


Figure 2.23: data on the size of vaterite

2.7 Applications of Optical Angular Momentum: Contact-Free Mechanotransduction, and the Quantum Limit of Optomechanics

Our vaterite samples are currently in use at the *Centro de Investigación Científica y de Educación Superior de Ensenada* (CICESE), by Beatriz Juárez, under the supervision of Veneranda Garcés and Kevin O'Donnell, for her PhD research. Previous studies of the effect of local shear stress upon biological cells have shown initiation of calcium waves, and other signaling factors, but there have remained questions about the separate roles of the mechanical strain induced by a physical probe and the chemical nature of the contact. By utilizing the local flow fields which surround a rotating vaterite sphere, these studies can be performed without any physical contact to the biological cell (beyond that of the fluid medium which always surrounds it). We have delivered vaterite to CICESE on multiple occasions, and Beatriz reports that her progress towards completing her PhD has been significant. Thus, this experiment is expected to result in a publication over the near term. – It is also notable that the vaterite particles that I have produced are highly porous, and so may serve as micro-containers for nano-components (*e.g.*, for targeted drug delivery at the cellular

level, or genetic transfection of individual cells, or fluorescent molecules for advanced imaging), which may play an essential role in upcoming projects.

Looking into the much more distant future, we have already noted, in the Introduction to this thesis, that there has been a controversial hypothesis put forth, that “New Physics” could force a boundary between the microscopic (quantum) and macroscopic (classical) domains (recognizing, of course, that the existence of such a boundary was hypothesized by the architects of the Copenhagen Interpretation, at the outset of quantum physics). What we were particularly referring to is the Diósi-Penrose (DP) gravity-induced collapse model. Lajos Diósi’s argument is that gravity is fundamentally *nonlinear* and so, when properly taken into account, – the argument goes – it induces a nonlinear modification of the Schrödinger equation, leading to localization once mass of the object described exceeds some critical threshold, currently estimated to be of order 10^{10} amu, and so the vaterite samples we have produced span a range from well above to well below this value. Roger Penrose has made an argument that a mass-superposition, spread over an extended area of space-time, would cause an energy shift for “different parts” of the superposition, naturally providing another mechanism for wavefunction collapse. We have greatly enjoyed discussing the possibilities with Dr. James Millen, who is a Marie Curie European Fellow in the Quantum Nanophysics group at the University of Vienna.

If there were some viable possibility for experimentally demonstrating the existence of a quantum-classical boundary, it would be of considerable interest. The conceptually simplest type of test would require cooling some degree of freedom associated with a massive object, and performing interferometry. Currently, the largest mass for which such interference has successfully been demonstrated is 10^4 a.m.u., which is (awesomely) impressive, but still six orders of magnitude below the threshold level required for testing gravitational collapse with microspheres. A new and controversial idea (from Caslav Bruckner, in Vienna) is that you could put a molecule into a spatial superposition over varying spacetime, and the effect of the curvature on the energy levels may cause collapse testable via spectroscopic means. Roger Penrose is currently writing a paper on summarizing the range of tests that have been suggested. Suffice it to say that this thesis does not aim to address all of the issues involved, and Dr. Millen has been careful to point towards the technical challenges involved.

At the same time, it is notable that as various groups have begun to extend the steady march toward the quantum limit of optomechanics, there has been one particular problem that our work might help to address: namely, cooling a trapped object requires decoupling it from the surrounding (room temperature) environment, but while mesoscale objects have been stably trapped in air, optical traps at these scales become unstable as the air pressure is reduced toward the vacuum limit. Interestingly, Yoshi Arita, working in the Kishan Dholakia group at St Andrews has demonstrated gyroscopic stabilization of such traps, by using vaterite particles spun, via transfer of optical angular momentum, by the trapping beam. The work presented here is intended as a follow-up to the achievements of the St Andrews group.

CHAPTER 3

STUDIES IN MICROFLUIDICS, AND THE CREATION OF MICRO-CONTAINERS FOR NANO-COMPONENTS

3.1 Introduction to microfluidics and lab-on-a-chip technology

The term “mesoscale” implies some transition between microscopic and macroscopic realms, but there are multiple kinds of physics to consider in describing such transition(s). At the end of the previous section, we discussed a transition involving a hypothetical quantum-classical boundary. Another kind of transition involves the emergence of irreversible behavior, which is to say, the Arrow of Time. A sequence of new “Fluctuation Theorems” offer insight into the violence of the nano-world, at space and time scales where the Second Law of Thermodynamics does not strictly apply.

In this section, I introduce my work on the study of microfluidics, which differs significantly from the topics introduced in the previous chapters, in that it is less directly related to the foundational questions of quantum mechanics (though there are those who would argue that questions of irreversibility are essential to “the quantum measurement problem,” as was briefly described in our introduction to SPADs in Chapter 1). Here, we deal with systems described by classical Statistical Physics.

My interest in the study of microfluidics initially stemmed from a fascination with DNA nanotechnology. In high school, I was struck by the notion that DNA could be utilized to store digital information at enormous densities. At Illinois Wesleyan, my expression of this interest led Dr. Spalding to introduce me to the separate fields of optical trapping (for single-molecule manipulation) and microfluidics, as a technology that might play a key role in extending, quite significantly, what would be possible via optical traps alone. Here, I will present the protocols I have learned

and developed, my experiences and my advice for working with microfluidics. I will also describe how microfluidics can be combined with optical trapping technologies for a next generation of experiments.

Microfluidics is the science and technology of systems that process pico-liter amount of fluids using micron-scale networks of channels. It is one of the fastest growing field in applied sciences, motivated by molecular analysis, biodefense, molecular biology and microelectronics. A microfluidic system consists of several important components: methods of introducing samples to the system, methods for moving the fluids in the channels of the chip, methods for processing and manipulating the fluids, *e.g.* mixing and purifying.[26] There are two important developments on the fabrication of the devices: the development of soft photolithography in PDMS, and the development of fabricating pneumatically activated valves, mixers and pumps.[26] As a result to these developments, the time period for fabricating PDMS devices has shortened to around two days, from initial designing to final testing, assuming that the researcher or the research group have access to mask printing facility or third party companies to provide mask-printing services. In general, microfluidic-based analysis has higher throughput and lower consumption than biochemical analysis carried out in conventional ways. Its current applications are in the study of protein crystallization, high-throughput screening in drug development, and study of single cells and single molecules.

Microfluidics has the ability to manipulate multiphase flow. In my research in both IWU and Harvard, we are interested in droplet-based microfluidics, which can generate monodisperse water emulsions in oil phase. These water droplets, each around pico-liter in size, can act as micro-containers and carry around DNA strings, proteins and single-cells for self-assembly and bio-analysis. We can process and manipulate these drops using optical tweezers, droplet sorting, multiple immersions and pico-injection techniques. For droplet-generation, we can have T-junction designs and co-flow designs, which will be shown in the first section of this chapter.

I began to work with PDMS-based microfluidics at Illinois Wesleyan, focusing more on fabrication. Then I spent the summer of 2016 extensively applying microfluidics to bio-related researches in Weitz group in Harvard. PDMS-based devices are relatively easy to fabricate, and are extensively

used by researchers in the field. As PDMS is cheap, non-toxic, and chemically stable, it is often the preferred material for creating lab-on-a-chip platforms for biochemical analysis, and it has wide applications in many other technological areas.

The vaterite described in the previous chapter turns out to be highly porous, and so those spheres, quite naturally, can be used as micro-containers for nano-components. Yet for a variety of reasons, we decided that there could be additional opportunities associated with having fluid-phase micro-containers for nano-components. Our goal at Illinois Wesleyan was to develop a monodisperse source of micron-scale fluid-phase droplets to serve as optically trappable containers (“hydrosomes”) for single-molecule studies and nano-component assembly. At Harvard, our goals expanded to include development of hydrogel-generation technology based on a PDMS microfluidic system. With our tailored designs and careful flow-rate control, hydrosomes and hydrogels with controllable dimensions can be generated continuously in the channels. We can successfully encapsulate a variety of biological cells, bacteria, or chemicals into these micron-scale droplets or hydrogels, for use in further studies. One project that I have worked on is to apply this technology platform for development of an immuno assay at the single-cell level, in which we encapsulate two different cell types into generated micro-compartments, for observing an immune response at the single cell level.

The first section of this chapter will be on microfluidic chip designing, with several examples of droplet-based microfluidics and important tips. The second section will be protocols on device fabrication, with tips on fabricating devices in Dr. Spalding’s lab in IWU. Then in the third section I will introduce my work in Harvard on single-cell immunol assay. Some technical details of the experiments are not available, as I am no longer officially associated with the group. The reason to include this part is to provide the readers with an example on the applications of this technology, which I believe has great potential in the field of applied sciences.

3.2 Designing microfluidic devices

3.2.1 Introduction

This section is about designing masks for soft photolithography, which is a crucial step during microfluidic device fabrication. Usually people use CAD softwares to design the masks. Both in the Weitz lab and at IWU, we use AutoDesk AutoCad to design the masks. When finished, the designs are sent to a third party photo-printing company for printing. The masks are plastic transparencies with patterns printed on them in black. The masks can selectively expose the wafer coated with photoresist. Then during development, the un-exposed parts will dissolve in the developer while the exposed parts are preserved. As a result, the patterns will be translated as channels on the microfluidic devices.

There are complete tutorials on AutoDesk's websites and on YouTube. When designing patterns, avoid overlays, open polygons, random lines or dots, as the companies will charge more for corrections.[22]

One example of a well-designed mask is shown in Figure 3.1.

3.2.2 Device components

Filters at the inlets

The design for filters at the inlets is shown in Figure 3.2 below. The gratings in the design is for filtering out the impurities, like pieces of PDMS from the channel.

Resistor

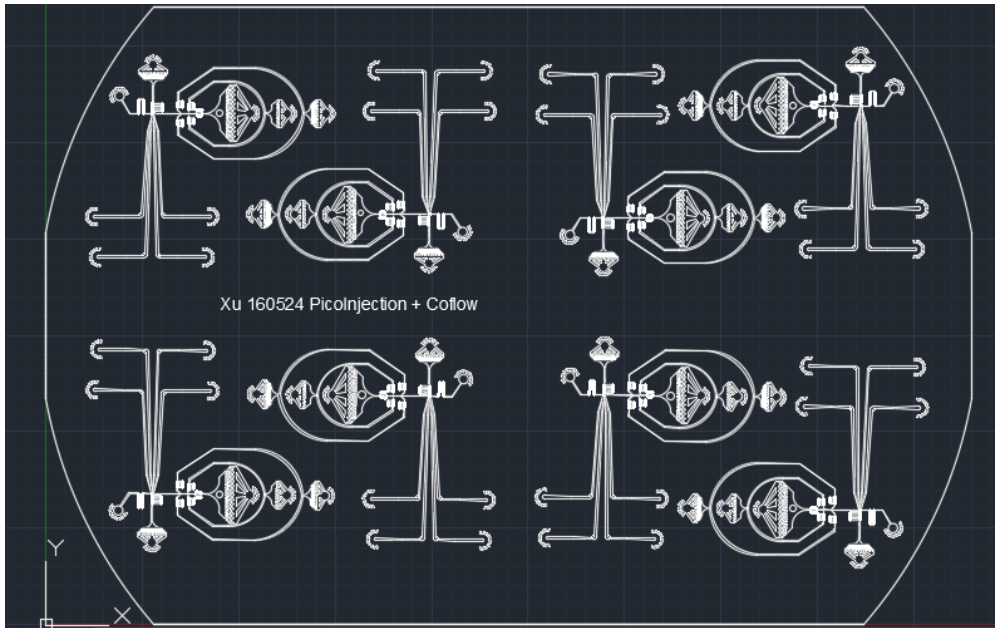


Figure 3.1: Co-flow droplet generator with pico-injection, designed by Xu Zhang, Ph.D from Weitz lab. [28]

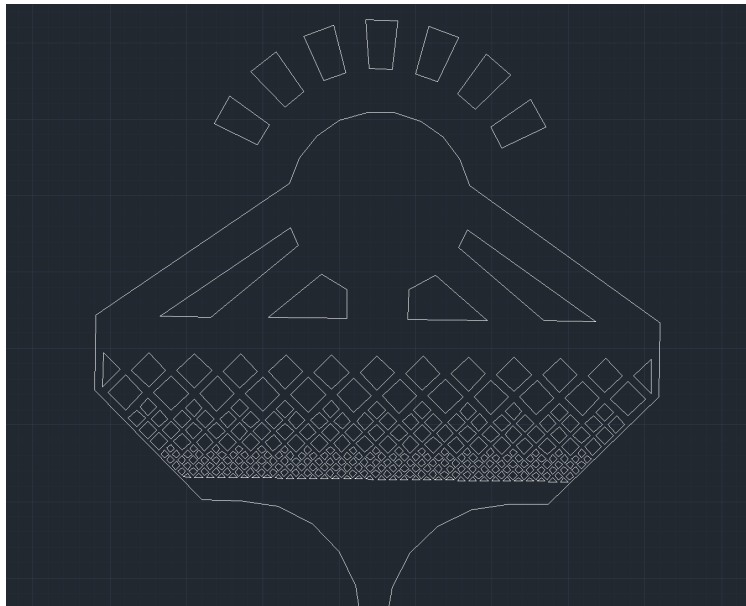


Figure 3.2: Design for inlet filter. [28]

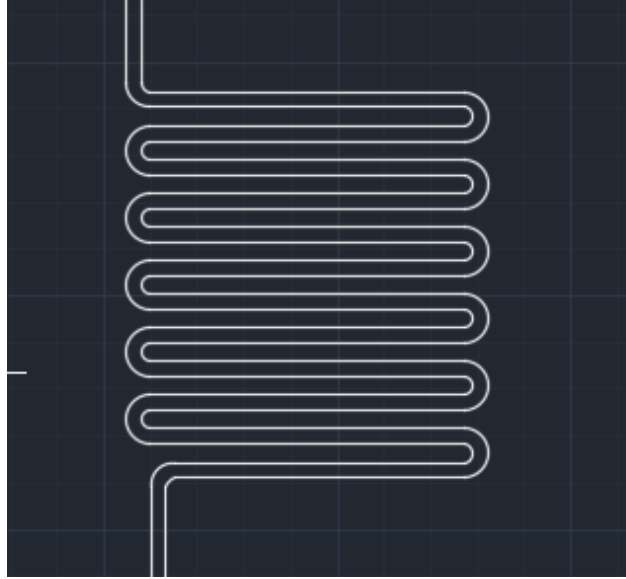


Figure 3.3: Fluidic resistor design. [28]

A fluidic resistor is used for absorbing the mechanical shocks produced by the syringe pumps. The usual design for such a resistor is shown in Figure 3.3.

Mixer

The mixer uses its wiggling structure to mechanically shake the drops to make sure the solutions are mixed uniformly. The design for mixer is shown in Figure 3.4.

Co-flow droplet generator

The Co-flow droplet generator is a common component for generating water emulsions. One design example is shown in Figure 3.5. The inlet on the right is the inlet for water while the one on the left is for oil.[28]

Pico-injection

Pico-injection is used when we want to add some solutions or components to the drops already made. The electrodes will break the surfactant and let the incoming droplets merge with the injecting flow. Usually the electrodes have a voltage around 5000V. A design example is shown in

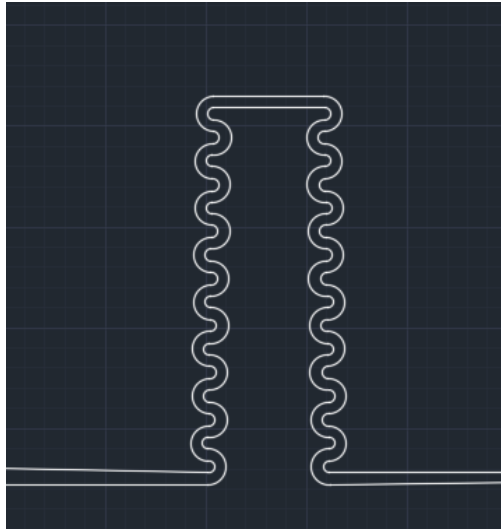


Figure 3.4: Mixer design. [28]

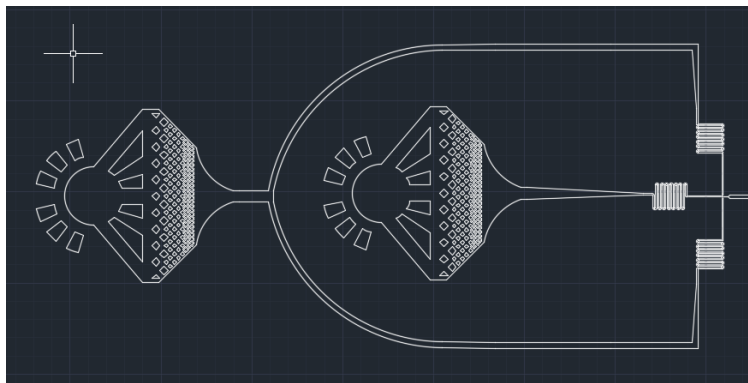


Figure 3.5: Co-flow droplet generator design. [28]

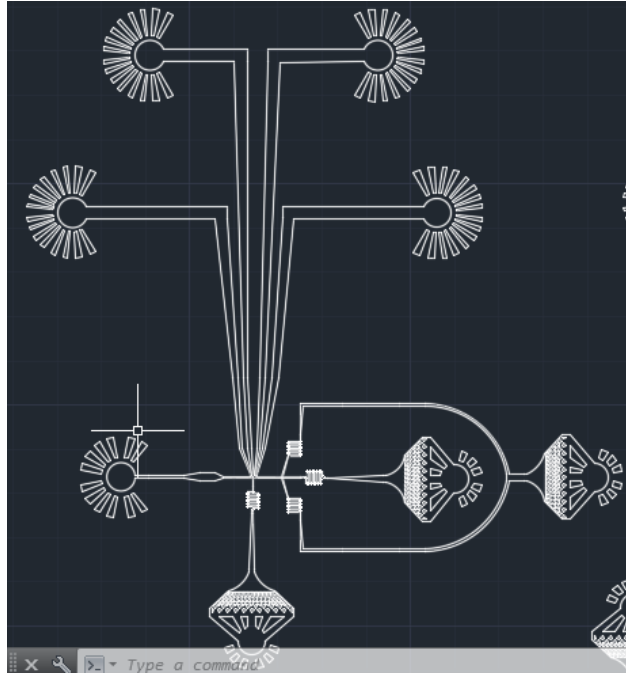


Figure 3.6: Pico-injection design.[28]

Figure 3.6, and a zoomed-in version of the design is shown in Figure 3.7.[28]

Reservoir and design for optical trapping

Reservoir is used for observing, controlling or temporarily storing large amount of droplets. In Harvard, we use reservoir to incubate the cells and observe their immunol activities. In IWU, we are going to use optical tweezers to trap water droplets in oil for nano self-assembly. The design used in Harvard is shown in Figure 3.8, designed by Xu Zhang, Ph.D, and the design used in IWU

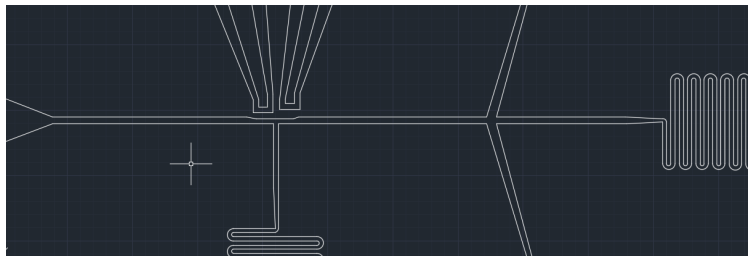


Figure 3.7: Pico-injection design zoomed in. [28]

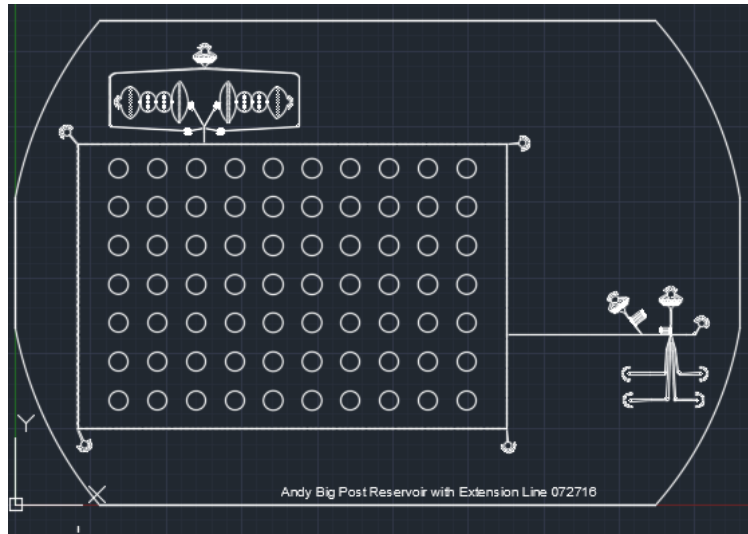


Figure 3.8: Droplet reservoir designed by Xu Zhang, Ph.D, from Weitz lab. [28]

for trapping is shown in Figure 3.9.

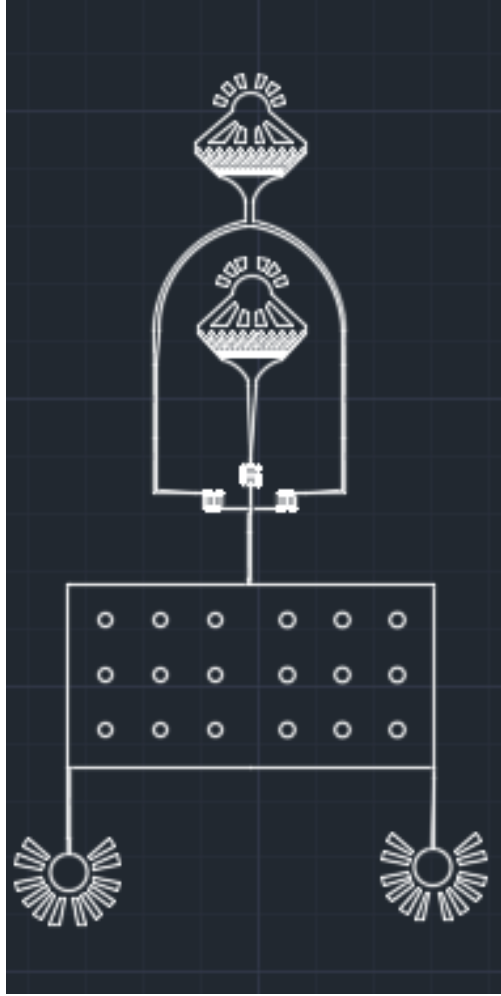


Figure 3.9: Droplet generator and reservoir for optical trapping

3.3 PDMS-based microfluidic device fabrication

3.3.1 Materials required

The materials listed here are mostly for fabrication of PDMS-based microfluidic devices themselves. Further items for doing microfluidic experiments are specified in the notes which follow. This list and the accompanying protocol mostly come from Weitz lab protocol.[22] Some of the items are particular to work done at IWU, as noted.

Reagents

1. SU-8 photoresist (MicroChem, SU-8 2000 series or 3000 series, depending on the dimension of the channels). This is a photo-sensitive polymer used for making patterns on silicon wafers. These chemicals are highly flammable and toxic and should be used in a fume hood or with respiratory protection. Cleanup is essential.
2. Propylene glycol monomethyl ether acetate (PGMEA; Sigma-Aldrich, cat.no. 537543). PGMEA is used as developer during the soft photolithography process and it will dissolve the unexposed photoresist on the silicon wafers. This chemical is highly flammable and should be operated in a fume hood.
3. Polydimethylsiloxane (PDMS and its curing agent, Dow Corning, Sylgard 184) is non-toxic, plain old (transparent) silicone rubber, popularized by George Whitesides for making microfluidic devices.
4. Isopropanol Alcohol (Sigma-Aldrich, cat.no. 278475) is used for rinsing the developer PGMEA from the wafer after developing. This liquid is highly flammable and should be handled in a fume hood.

5. Aquapel (Aquapel, cat.no.47100) is used for treating the channels of the microfluidic devices to make them hydrophobic. It is highly toxic and moisture sensitive, and should be handled in a fume hood with gloves, lab coats and eye protections. The liquid will come in a cylindrical sealed glass container with plastics wrapped around it. When opening, carefully cut open the plastic and take out the glass. Then use a glass cutter to open the container. Do not allow the liquid to contact bare skin.

6. Pressurized oxygen for the oxygen plasma cleaner. If you were to, instead, use only air during the plasma treatment process, the bonding between the PDMS and the glass slides will likely fail.

7. HFE-7500 (cat.no.98-0212-2928-5). This is the oil phase we used at Harvard for producing water droplets. It is a bio-friendly liquid, ideal for microfluidic-based bio-analysis. Also, the index of refraction at room temperature is 1.29, lower than that of water, which is 1.33, which simplifies optical trapping of the droplets. Avoid direct contact with this chemical.

8. Pressurized air, or pressurized nitrogen for cleaning and drying wafers and the cured PDMS.

Equipment to have on hand

1. Spin coater (Laurell, Model WS-650MZ-23NPP), used during photolithography process for uniformly coating the silicon wafer with photoresist.

2. Oxygen plasma cleaner (Gala Instrumente at Harvard; SPI Plasma Prep II at IWU)

3. Vacuum oven for removing air bubbles in liquid phase PDMS, used at IWU lab (Fisher Scientific); or a planetary centrifugal mixer (Thinky mixer, Cat. No. ARE-310) used in the Harvard Soft Lithography clean room.

4. Filtered air blower, used in Harvard lab to dry wafers and PDMS using pressurized nitrogen.

5. Fume hood.

6. Silicon wafers (3-inch diameter, Type-p, 1S polished, University Wafer, cat.no.S3P01SP).
7. UV light source (unlabeled source at IWU; OAI, model LS30/5 at Harvard), used for photolithography.
8. Ceramic hot plate, could be used for curing PDMS.
9. Syringe pumps, this is for doing microfluidic experiments, not needed for fabrication. (Harvard Apparatus in Harvard lab, not required to be this brand)
10. AutoCAD software.
11. Cover glass (24X60 mm, No.1.5; Corning, cat.no. 2980-246)
12. Glass slides (75X50 mm, Corning, cat.no.2947-75X50)
13. Biopsy punches (Harris Uni-core, Ted Pella 0.5, 0.75 and 1.0 mm diameter)
14. Hamilton gas-tight syringe, 2.5ml and 5ml, this is for doing microfluidic experiments, not needed for fabrication. (Hamilton, cat.no. 201300)
15. Needles, this is for doing microfluidic experiments, not needed for fabrication. (23 gauge and 27.5 gauge; Terumo Neolus, cat.no.NN2325R)
16. PE-2 tubing, this is for doing microfluidic experiments, not needed for fabrication.(Intramedic)
17. Petri dishes (100-mm diameter X 15 mm; BD Falcon, cat.no.351029)
18. Tweezers.

19. Aluminum foil (for hot plate)
20. Pipettes, for doing the microfluidic experiments themselves, not for device fabrication. (5-, 10-, 25- and 50-ml; BD Falcon)
21. UV glasses, to protect the eye while exposing the wafer to UV light.
22. Gloves.
23. Microscope (research-grade Olympus, Zeiss, or Nikon)
24. Plastic cups or boats.
25. Razor blades or scalpel.
26. Scotch tape.
27. Millipore filter, 0.22 micron (PVDF and polyethersulfonate type)

3.3.2 Fabrication protocols for microfluidic chips

The protocols presented here are standards the from Weitz lab.[22] There are variations for fabricating microfluidic devices in IWU lab, noted in the section on important tips.

Mask design and ordering

Use CAD softwares to design your masks. Usually I use AutoCAD. Well-written AutoCAD tutorials are available online. Example patterns are provided in the section below on designing microfluidic devices. These designs are converted into masks for photolithography by a high-resolution photo

service company such as Fineline Imaging, Cad/Art services or Selba. Features in the provided designs should be printed at a minimum resolution of 24000 d.p.i.

When drawing using CAD, avoid overlays, open structures, random dots or other components, as the companies will charge extra for correcting errors and defects.

Master fabrication

The following Weitz Lab protocol has just been published as an attachment to the paper, “Single-cell analysis and sorting using droplet-based microfluidics” by Mazutis, Linas and Gilbert, John and Ung, W Lloyd and Weitz, David A and Griffiths, Andrew D and Heyman, John A.[22]

1. Choose an SU-8 photoresist with a viscosity appropriate for the desired microfluidic channel thickness. For example, 10-20 micron deep channels of good quality can be effectively produced using SU-8 2010 or 2015. Channels of 20-40 micron deep can be produced with SU-8 2015, 2025 and 2035. For channels deeper than 50, use SU-8 2050 and higher. Follow the manufacturer’s online processing guidelines. For the rest of these notes, I assume that the channel has a designed thickness of 25 microns.
2. Usually, silicon wafers are already very clean straight out the package, and can be directly used for fabricating masters. However, if there are traces of organic materials on the surface, clean the wafers as follows: immerse the wafer in a crystallizing dish filled with acetone and sonicate it for 2-5 min; transfer the wafer into a glass crystallizing dish filled with methanol and sonicate for 1-2 min; remove the wafer and rinse it thoroughly with isopropanol; blow the isopropanol off the wafer with pressurized nitrogen or air and heat the wafer up at 200°C to vaporize any leftover solvent.
3. Use aluminum foil to line the bottom of the spin coater for (much) simpler clean up. Place the wafer onto the vacuum chuck of the spin coater and carefully pour 3ml of SU-8 2025 onto the center of the wafer. Do not allow any bubbles in the photoresist. When almost done with pouring, drag the flow (could be quite viscous) outside the wafer horizontally to avoid trapping bubbles.

4. Turn on the vacuum and then ramp the spin rate to 500 r.p.m. and spin for 15s; thereafter, ramp the spin rate, at 500 r.p.m.s^{-1} , to 3000 r.p.m and spin for 30s, to create a flat resist layer of the desired thickness. The relationship between the spin rate of the wafer and the thickness of the channels is shown in figure below, from the data sheet provided by MicroChem.

5. Pre-bake the coated wafer for 1 min on a 65°C hot plate. The relationship between baking

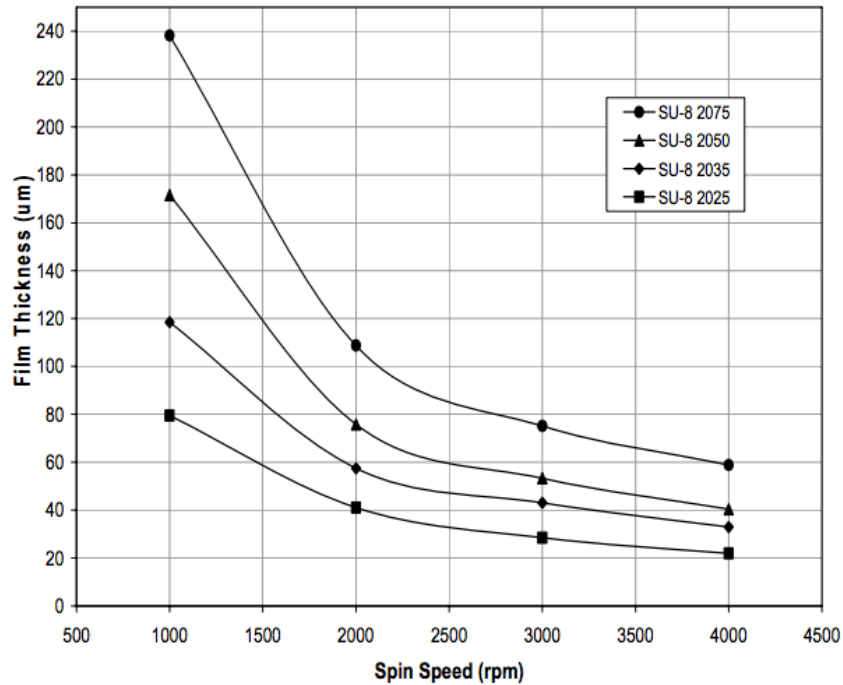


Figure 3.10: SU-8 2000 spin rate *vs.* thickness

time and thickness is shown in Fig. 3.11. Make sure that the hot plate is level and *flat*, so the photoresist coated on the wafer will not flow and the temperature is uniform.

6. Bake the wafer at 95°C for 3 min. Some over-baking will not reduce the quality of the master.

7. Cool the wafer to room temperature.

8. Place the photomask on top of the substrate and expose the wafer according to the specifications

THICKNESS microns	SOFT BAKE TIMES	
	(65°C) minutes	(95°C) minutes
25 - 40	0 - 3	5 - 6
45 - 80	0 - 3	6 - 9
85 - 110	5	10 - 20
115 - 150	5	20 - 30
160 - 225	7	30 - 45

Figure 3.11: SU-8 2000 soft bake times *vs.* thickness

in the MicroChem data sheet, based upon the power of the UV source at hand. Fig. 3.12 illustrates the basic dependence. For my work, for 25 microns, the exposure time is around 20s.

9. Post-baking: Fig. 3.13 gives how the required bake time varies with temperature. For 25 micron,

THICKNESS microns	EXPOSURE ENERGY mJ/cm ²
25 - 40	150 - 160
45 - 80	150 - 215
85 - 110	215 - 240
115 - 150	240 - 260
160 - 225	260 - 350

Figure 3.12: SU-8 2000 exposure time *vs.* UV power

bake the wafer at 65°C for 1 min and at 95°C for 3 min.

10. Cool the wafer down at room temperature.

11. Submerge the wafer in PGMEA with the coated side up and agitate for development. A table

THICKNESS	PEB TIME	PEB TIME
microns	(65°C)* minutes	(95°C) minutes
25 - 40	1	5 - 6
45 - 80	1 - 2	6 - 7
85 - 110	2 - 5	8 - 10
115 - 150	5	10 - 12
160 - 225	5	12 - 15

Figure 3.13: SU-8 2000 post-exposure baking time *vs.* thickness

below shows the relationship between developing time and thickness of the channels. You can either gently agitate the container for 4min or ultrasonic the solution for 1min. Directly using ultrasonic is not recommended, as it will potentially rip off the patterns on the wafer. This step should be performed in fume hood, as the PGMEA is highly flammable.

12. Rinse the wafer with isopropanol. Conduct this step in the fume hood, as isopropanol is a

THICKNESS	DEVELOPMENT TIME
microns	minutes
25 - 40	4 - 5
45 - 75	5 - 7
80 - 110	7 - 10
115 - 150	10 - 15
160 - 225	15 - 17

Figure 3.14: SU-8 2000 developing time *vs.* thickness

highly flammable chemical.

13. Dry the wafer with pressurized nitrogen and the air blower. If there is white residue on the wafer, re-develop the wafer in PGMEA for a while and rinse it with isopropanol.

14. Hard-bake: To improve adhesion of photoresist to the wafer, heat the wafer to 150°C, then slowly cool the wafer to room temperature. Handle with caution.

15. Use a microscope to examine the quality of the channels. The wafer can be translated into a petri dish. Avoid dusty environments.

PDMS molding

1. Place the master wafer in a 100-mm diameter plastic petri dish.

2. Weigh 30g PDMS and 3g curing agent in a plastic cup and uniformly mix them together. In Harvard, a centrifugal mixer was used for mixing, with 30s spent mixing and 30s de-foaming. However this is not required: mixing can be achieved using a wooden stick or a spoon, as long as a vacuum chamber is then used to get rid of the bubbles.

3. Pour the PDMS mixture into the Petri dish 3 mm deep and place the Petri dish into a vacuum desiccator or a vacuum chamber. Release the vacuum periodically to prevent foam from spilling out of the dish.

4. Degas the PDMS until no bubbles remain attached to any device features and no new bubbles are being formed. Usually 15-30 min is sufficient. If a few bubbles persist, blow gently on the PDMS surface using an air blower or canned air, to break the bubbles.

5. Bake the PDMS in a 65°C oven on a flat, level surface for at least 2h to cure the PDMS. We have noticed that curing overnight gives better quality PDMS slabs. Right now the PDMS mold is very resilient and could be store at room temperature in a low dust environment for long periods of time.

6. Cut the PDMS slab with a scalpel and gently peel the PDMS from the silicon wafer. Excessive force will break the silicon wafer and ruin your work.

7. Cover the non-patterned side of the PDMS slab with frosted Scotch tape, and then place the device on a cutting mat with the channels facing upward.

8. Use a biopsy punch to create holes at each fluid inlet or outlet. Devices with micro-electrodes require additional holes, at a different punch diameter, for efficient solder filling. The size of the biopsy punch should be 1.21.5 times smaller than the outer diameter of the tubing to be used. We used a 0.75-mm-diameter biopsy punch for PE-2 tubing (Intramedic). For micro-electrode channels, we use a 0.5-mm-diameter biopsy punch.

9. Cover the patterned side of the PDMS with frosted Scotch tape so that both sides of the PDMS slab are now covered. Place the device, channel side down, on your work surface. Peel off the Scotch tape from the top side. This will remove most of the debris that results from PDMS hole punching.

10. Remove the Scotch tape from the patterned side and use sharp tweezers to remove any PDMS plugs that remain lodged inside the ports. Flush the PDMS slab holes with isopropanol to ensure complete removal of PDMS debris. Dry under a stream of nitrogen.

11. Place the PDMS slab and the glass slide in the plasma chamber with the channel side facing upward.

12. Plasma-treat the PDMS slab and the glass slide together. This step must be performed carefully, as it is essential that the binding of the PDMS slab to the glass is strong; otherwise delamination will occur during operation of the microfluidic device. The parameters for plasma treatment depend on the type of machine. For the oxygen plasma cleaner used at Harvard (GaLa Instrumente, Plasma Prep 2), the following settings worked well: plasma burst = 10 s, power = 2.5, oxygen level = 810. For the plasma chamber at IWU, we use a SPI plasma prep II. The manual is online.

13. Remove the PDMS slab and the glass slide from the chamber and bring the plasma-treated

faces into contact. Gently press the PDMS so that all parts are sealed to the glass.

14. Place the device in a 65°C oven. The time here does not matter much. The device can be stored in the oven for a long time.

Microelectrode fabrication

This is optional for general fabrication procedures and is only for devices with electrodes.

1. Place the device on a 90°C hot plate for 35 min.
2. Cut 5 cm of low-melting-temperature solder wire and use tweezers to insert it into the electrode channels. Solder bends easily; thus it should be held close to the tip. Upon insertion, the solder should melt immediately and start filling the microchannel. Continue pushing the solder into the hole until molten solder emerges from the outlet. Be careful not to burn yourself while working on the hot plate. A face shield should be worn for protection from molten solder spatters.
3. Remove any excess solder by using tweezers to gently scrape solder from the PDMS surface.
4. Insert metal pins into each end of the filled electrode channel. Verify electrical contact using a digital multimeter.

Channel surface treatment

1. The Aquapel solution is supplied in a glass ampule embedded in a thick felt pad. Carefully cut the pad and remove the ampule.
2. Place the ampule at the bottom of a 15-ml Falcon-type conical plastic tube and score the ampule using a diamond pen or similar. Carefully break the ampule inside the tube.
3. Transfer the Aquapel solution into a 5-ml glass, gas-tight syringe, while leaving the broken glass in the 15-ml plastic tube.

4. Remove air bubbles from the syringe. Upon prolonged contact with air, Aquapel precipitates and loses its functionality. By preventing air contact, Aquapel can be stored for up to 2 weeks.
5. Attach a 0.22- μ m Millipore filter and a 23-gauge needle to the syringe and affix PE-2 microtubing to the needle.
6. Insert the microtube into the continuous-phase inlet of a single microfluidic module, and then inject the surface treatment solution to fill each of the device channels.
7. Leave the solution in the channels for 1030 s, and then flush with pressurized air or nitrogen. Devices can be stored at room temperature for weeks or months before use. To prevent degradation of treated surfaces, avoid direct sunlight. Device surfaces should be covered with Scotch tape to keep dust from the openings.

Important tips

1. During soft baking, the photoresist will not solidify at 95°C over the time used for baking. Thus, handle with caution when taking it off the hot plate. It will solidify when cooled down.
2. Do not use excessive force to inject solder into a channel, or inject excessive amounts, as the solder will then leak into other neighboring channels and can also bead-up at the outlet, potentially resulting in an electrical short.
3. Press reasonably hard on the mask and wafer when exposing to UV light. Failure to do so will result in under-exposure of the channels and they will detach from the wafer during development.
4. When the resist has wrinkles on its surface, it is probably because the solvent was not completely evaporated during the initial baking step.
5. When there are cracks in the SU-8 film, it is probably because of rapid substrate cooling causing

thermal stresses. You can cool the wafer more slowly by placing it on a thermally insulating surface to cool, or by turning the hot plate off and allowing the wafer and hot plate to cool down together

6. If SU-8 structures detach from the wafer during PDMS peeling, it is probably because of insufficient UV exposure, or unclean wafers.

7. If PDMS does not peel properly from SU-8 structures, it is probably due to insufficient baking time.

8. If the device leaks from the inlets, it probably means that the punches were not sharp enough.

This entire fabrication process is condensed into the following graph, and the photo of a complete device is attached as an example.

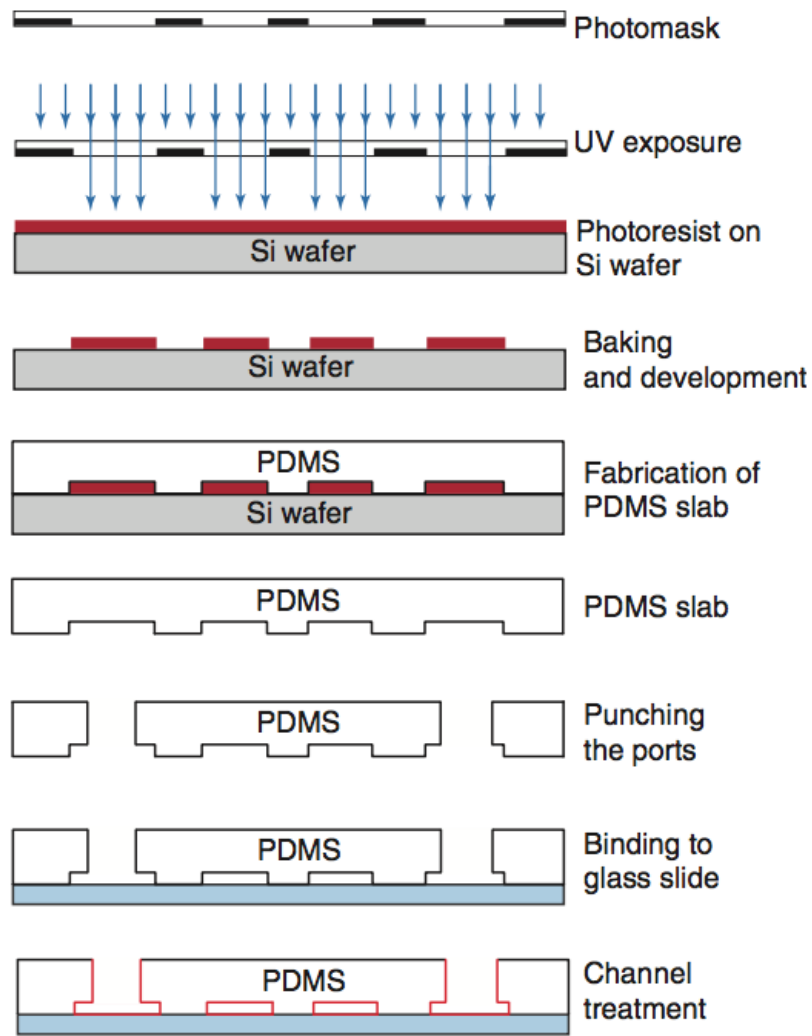


Figure 3.15: Fabrication process for creating PDMS-based microfluidic devices

3.4 Application of lab-on-a-chip technology: droplet-based single cell immunol assay

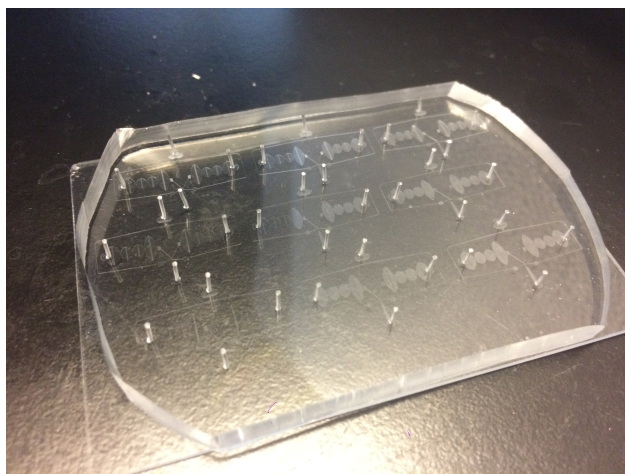


Figure 3.16: An example PDMS-based microfluidic device

3.4.1 Introduction

This section briefly introduce readers to the summer project I worked on at Harvard. I will not provide in-depth details of the experiments, out of respect for the group I worked in, but an overview may spark interest.

One feature of microfluidics is that the channel dimensions are typically comparable to that of biological cells, making it very suitable for single cell analysis. Droplets, in our case, generated in these device, are perfect for encapsulating single cells. These drops, which serve as individual micro-reactors and micro-containers, transport their contents to different parts of the chip where specific operations are processed. Many such operations can be performed on these droplets. Pico-injection can deliver new content into the drops, while sorting is suitable for separating drops based on their contents.

By using a microfluidic droplet-based immunol assay, we are addressing one of the most fundamental questions of immunology: which immunol cell kills which target cell? In other words, the immunol relationship is to be clarified. In the human immunol system, there are thousands of different immunol cells, and there are thousands of guest cells getting into the human body every

minute. The immunol system works when certain types of immunol cells recognize certain types of guest cells, and then secrete chemicals to kill them. If the immunol relationship is known, when a human is infected by a certain kind of disease, we can reinforce the original immunol activity by injecting large quantities of the corresponding immunol cells.

The basic methodology is simple. We encapsulate one immunol cell and one target cell into one droplet, in a microfluidic device, and use microscopes to study their interaction, *i.e.*, detecting the death of the target cell or the release of the antibody from the immunol cell. The drops are largely alginate, a bio-compatible polymer. Alginate can be cross-linked, or “gelled” using ions like Ca^{+2} , which can be useful when doing sorting in a commercially available sorting machine. While surfactant is added to the drops to prevent them from merging, occasionally, under pressure or shock vibrations, drops will coalesce. Once we cross-link the alginate to make them gels, we no longer need to worry about such issues.

3.4.2 Method 1: Dye release

When cells die, the permeability of their cell membrane will change. As a result, if a fluorescent dye has been injected into the target cell beforehand, then the dye will be released once the immunol cell kills it.

In our experiment, we used K562 cell as a target cell and NK cell (Nature Killer cell) as our immunol cell. We dyed both cells using different fluorescence dyes and encapsulated them into drops using a droplet-making microfluidic device that we fabricated. After collecting all drops into a reservoir, we incubate the reservoir while monitoring the process with a confocal microscope, which allows us to image the cells, in drops, while they communicate with each other. We excite the fluorescence dye with a laser of the appropriate wavelength, and then filter that wavelength from the imaging path of the microscope, so as to only detect the fluorescence emission of the dye. We created video clips showing the dye-release process. Figure 3.17 demonstrates the basic principle.

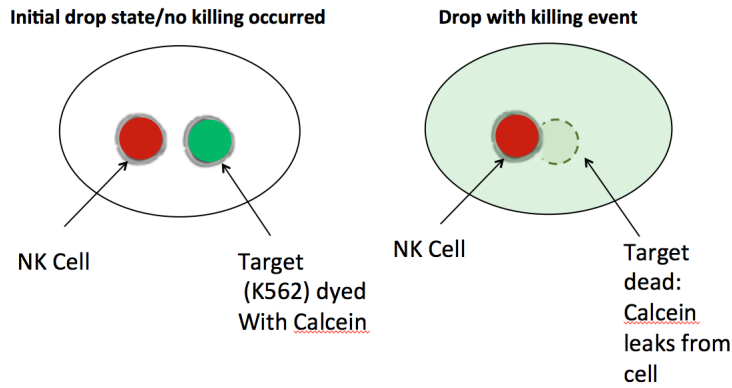


Figure 3.17: Dye Release

3.4.3 Method 2: Apoptosis Detection

In this method, we still use NK cells as killer cells and K562 as target cells. However, we dyed

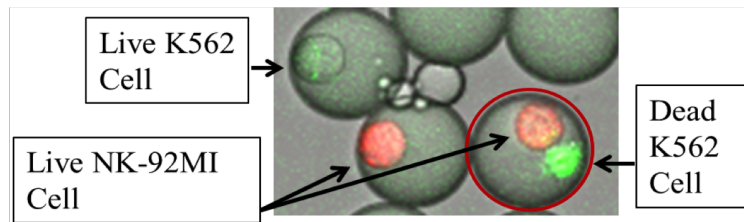


Figure 3.18: NK92-MI cells (red) were encapsulated with unstained K562 cells and Caspase-3-dependent green fluorescence probe and incubated 37C for 3 hr.

the NK cells with *red* fluorescence dye beforehand and add Caspase-3-dependent green fluorescence dye into the alginate. The green fluorescence dye is an indicator of cell death, which will infiltrate the cell's membrane once the cell is killed. Then we encapsulate both cells in drops, collect them into a syringe and incubate the syringe at 37C. We image the drops under the confocal microscope both before and after incubation. A result is shown in Figure 3.18.

3.4.4 Method 3: Fluorescence concentration assay to detect secreted IFN- γ

In this method, drops encapsulate NK cells that are dyed red, along with unstained K562 cells,

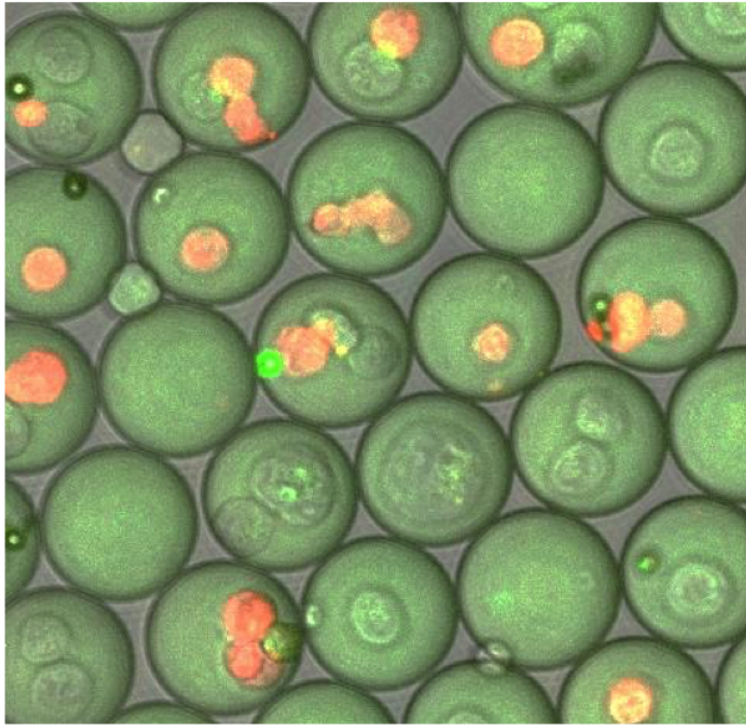


Figure 3.19: Fluorescence concentration assay to detect secreted IFN- γ

and Anti-IFN- γ capture beads. During the immunol interactions, the NK cells will secrete IFN- γ , an antibody that kills K562 cells. The IFN- γ also attaches to the beads, and when it does so, the bead will emit green light under proper excitation. This emission signifies the immunol process, as shown in Figure 3.19.

Currently we are combining methods, aiming to achieve a most effective demonstration.

3.4.5 Notes and protocols on water droplet generation using co-flow microfluidic devices

Droplet generation protocol from Weitz lab [22]

1. Take a completed microfluidic droplet generation device with its channels treated by aquapel.
2. Prepare 2ml HFE-7500 oil with 1.5% (wt/wt) fluorinated surfactant.
3. Load the HFE-7500 oil with surfactant into a 5ml syringe.
4. Load 1ml H₂O into a 5ml syringe.
5. Place 23-gauge needles on the syringes, connect to PE-2 microtubing and place on vertically oriented syringe pumps with the needles facing upward.
6. Start infusing both fluids to fill up the tubing and to squeeze out all the air from the tubing. The infusion rate, for now, will not influence the following steps.
7. Connect the syringes to the corresponding inlets of the microfluidic chip via PE-2 microtubing and start infusing. Now set the rate of infusion of the water phase to somewhere in the range from 50 microliters per hour to 800 microliters per hour. The rate of the oil phase can then be set to be either more or less than that of the water phase, with appropriate ratios depending on the relative viscosity of the fluids. Note that it can take up to several minutes to get the fluids into the channels due to friction and pressure issues in the tubing and channels. However, if after 15 minutes nothing is coming out of a channel, switch to a different device.
8. Once fluids are flowing through the channels, droplets should start to form continuously at the co-flow junction. The droplet size can be adjusted via control of the flow rates of the fluids.

9. (Optional) Once flow is steady, initiate collection of the droplets at the outlet by connecting PE-2 microtubing to a syringe or to a collection tube. Collection can take up to 3 hours, depending on the amount of droplets needed.

BIBLIOGRAPHY

- [1] L. Allen, M. W. Beijersbergen, R. J. C. Spreeuw, and J. P. Woerdman. Orbital angular momentum of light and the transformation of laguerre-gaussian laser modes. *Physics Review Letter A*, June 1992.
- [2] Y. Arita, J.M. Richards, G. C. Spalding M. Mazilu, S.S. Spesyvtseva, and K. Dholakia D. Craig. Rotational dynamics and heating of trapped nanovaterite particles. *ACS Nano*, 10, 2016.
- [3] Yoshi Arita. private communication.
- [4] Reuben S. Aspden, Miles J. Padgett, and Gabriel C. Spalding. Video recording true single-photon double-slit interference. *American Journal of Physics*, August 2016.
- [5] Stephen M. Barnett, Mohamed Babiker, and Miles J. Padgett. Optical orbital angular momentum. *The Royal Society Publishing*, 2017.
- [6] Mark Beck. *Quantum Mechanics: Theory and Experiments*. Oxford University Press, 198 Madison Ave, New York, New York, USA, 2012.
- [7] A. I. Bishop, T. A. Nieminen, Heckenberg, and H. N. R. RubinszteinDunlop. Optical microrheology using rotating laser-trapped particles. *Physics Review Letter*, 92, 2004.
- [8] O Bryndahl. Geometrical transformations in optics. *Journal of the Optical Society of America*, 64(8), 1974.
- [9] Vittorio Degiorgio and Ilaria Cristiani. *Photonics*. Springer, 2016.
- [10] Dietrich Dehlinger and M. W. Mitchell. Entangled photons, nonlocality, and bell inequalities in the undergraduate laboratory. *American Journal of Physics*, 70(903), 2002.
- [11] Christine E. M. Demore, Alexander Volovick Zhengyi Yang, Sandy Cochran, Michael P. MacDonald, and Gabriel C. Spalding. Mechanical evidence of the orbital angular momentum to energy ratio of vortex beams. *Physics Review Letters*, May 2012.
- [12] Eric R. Dufresne, Gabriel C. Spalding, Matthew Dearing, Steven Sheets, and David Grier. Computer-generated holographic optical tweezer arrays. *Review of Scientific Instruments*, 72, December 2000.
- [13] G.Berkhout, M.P.J. Lavery, J. Courtial, M.W. Beijersbergen, and M.J. Padgett. Efficient sorting of orbital angular momentum states of light. *Physical Review Letters*, 15(105), 2010.

- [14] David Griffith. *Introduction to Quantum Mechanics*. Pearson Education, 2005.
- [15] Liam E. Gumley. *Practical IDL Programming: Creating Effective Data Analysis and Visualization Applications*. Morgan Kaufmann Publishers, 2002.
- [16] Benjamin Harke, Jan Keller, Chaitanya K. Ullal, Volker Westphal, Andreas Schönle, and Stefan W. Hell. Resolution scaling in sted microscopy. *Optics Express*, 2008.
- [17] A. Jesacher, A. Schwaighofer, S. Fuerhapter, C. Maurer, S. Bernet, and M. Ritsch-Martel. Wavefront correction of spatial light modulators using an optical vortex image. *Optics Express*, 15(9), April 2007.
- [18] Paul Kwiat. Lecture notes phys513 quantum optics and quantum information, February 2010.
- [19] Martin Lavery. private communication.
- [20] Martin P. J. Lavery, David J. Robertson, Gregorius C. G. Berkhout, Gordon D. Love, Miles J. Padgett, and Johannes Courtial. Refractive elements for the measurement of the orbital angular momentum of a single photon. *Optical Society of America*, 20, Jan 2012.
- [21] Martin P.J Lavery. Measurement of light’s orbital angular momentum. *Ph.D. Thesis, University of Glasgow*, October 2013.
- [22] Linas Mazutis, John Gilbert, W Lloyd Ung, David Weitz, Andrew Griffiths, and John Heyman. Single-cell analysis and sorting using droplet-based microfluidics. *Nature*, April 2013.
- [23] Paroma Palchoudhuri. A study of the phenomenon of spontaneous parametric down-conversion. 2014.
- [24] Francsco Pampaloni and Joerg Enderlein. Gaussian, hermite-gaussian, and laguerre-gaussian beams: A primer. *American Journal of Physics*, 2004.
- [25] Gabriel C. Spalding, Johannes Courtial, and Roberto Di Leonardo. Holographic optical tweezers.
- [26] George M. Whitesides. The origins and the future of microfluidics. *Nature*, 442, July 2006.
- [27] Alan E. Willner. Twisted light could dramatically boost data rates. *IEEE Spectrum*, August 2016.
- [28] Xu Zhang. private communication.